

NORTHWESTERN UNIVERSITY

Quantitative Superfluid Helium-3 from Confinement to Bulk

A DISSERTATION

SUBMITTED TO THE GRADUATE SCHOOL
IN PARTIAL FULFILLMENT OF THE REQUIREMENTS

for the degree

DOCTOR OF PHILOSOPHY

Field of Physics and Astronomy

By

Joshua J. Wiman

EVANSTON, ILLINOIS

December 2018

© Copyright by Joshua J. Wiman 2018

All Rights Reserved

ABSTRACT

Quantitative Superfluid Helium-3 from Confinement to Bulk

Joshua J. Wiman

Liquid ^3He is a remarkable substance. Even prior to the discovery of superfluidity in 1972, liquid ^3He was the paradigm of a strongly interacting Fermi liquid. At even lower temperatures, liquid ^3He undergoes a phase transition to a p -wave Fermi superfluid. Over 40 years since its discovery, superfluid ^3He is still the only confirmed p -wave superfluid.

One of the most striking features of this superfluid is the existence of two distinct phases in the bulk liquid. These A and B phases are separated by a line of first order transitions as a function of temperature and pressure. Shortly after the discovery of p -wave superfluidity, it was realized that additional phases should be obtainable through geometric confinement. With more recent advances in materials design and fabrication, the use of confining geometries to control the superfluid ^3He phase diagram has grown to encompass a number of ordered and disordered geometries.

In this thesis I first consider the confinement problem in the Ginzburg-Landau regime, focusing on novel superfluid phases in arrays of line impurities, thin films, and nanoscale channels. In the last chapter I revisit the problem of precisely calculating bulk superfluid properties from a microscopic model. Using a quasiclassical free-energy functional approach, with newly determined quasiparticle interactions, quantitative agreement with the experimental specific heat and A-B phase boundary is achieved.

Acknowledgements

I must first thank my graduate advisor Jim Sauls for his guidance and understanding throughout my entire time at Northwestern. I came here knowing next to nothing about superfluid ^3He and many-body condensed matter theory, and I'm leaving having completed the first real microscopic calculation of the superfluid ^3He phase diagram.

I am also extremely grateful to Jens Koch and Bill Halperin for their advice and support. Their extended research groups—undergraduates, graduate students, postdocs, and professors—felt to me as a broad and inclusive condensed matter physics community at Northwestern.

Further, I'll try to acknowledge additional individuals, although I know there are too many to name. I thank Oleksii Shevtsov and Peter Groszkowski for assisting with CMT IT duties. In the ULT lab, I had numerous beneficial discussions with Johannes Pollanen, Leo Li, and Charles Collette, along with significant project collaborations with Andrew Zimmerman and Man Nguyen.

Outside of Northwestern, I greatly appreciate our close collaborators: Anton Vorontsov, Takeshi Mizushima, Jeevak Parpia, John Saunders, Erkki Thuneberg, Vladimir Dmitriev, and their associated research groups. Finally I'd like to thank Yoonseok Lee for both his role as my undergraduate advisor and his continued support and also Priya Sharma for many illuminating discussions at conferences.

Preface

This thesis contains chapters prefixed with “Publication”. These are, in fact, the preprint versions of published papers adapted to the format of the thesis and with additional notes and corrections. Each of them includes substantial wording due to my graduate advisor and co-author Jim Sauls, as well as numerous careful edits and additions due to editors, peer reviewers, journal producers, and colleagues.

The included publications are:

WIMAN, J. J., AND SAULS, J. A. Superfluid Phases of ^3He in a Periodic Confined Geometry. *J Low Temp Phys* 175, 1-2 (Apr. 2014), 17–30.

WIMAN, J. J., AND SAULS, J. A. Superfluid phases of ^3He in nanoscale channels. *Phys. Rev. B* 92, 14 (Oct. 2015), 144515.

WIMAN, J. J., AND SAULS, J. A. Strong-Coupling and the Stripe Phase of ^3He . *J Low Temp Phys* 184, 5-6 (Sept. 2016), 1054–1070.

WIMAN, J. J., AND SAULS, J. A. Spontaneous Helical Order of a Chiral p -Wave Superfluid Confined in Nanoscale Channels. *Phys. Rev. Lett.* 121, 4 (July 2018), 045301.

Table of Contents

ABSTRACT	3
Acknowledgements	4
Preface	5
Table of Contents	6
List of Tables	10
List of Figures	11
Chapter 1. Introduction	21
Chapter 2. Publication: Superfluid phases of ^3He in a periodic confined geometry	24
2.1. Abstract	24
2.2. Introduction	25
2.3. Ginzburg-Landau Theory	28
2.4. Symmetry Classes of ^3He in a confined D_{4h} geometry	31
2.5. Numerical Methods	37
2.6. Stable Phases - Maximal Pair-breaking	39
2.7. Weak-Coupling Phase Diagram	42
2.8. Conclusions	45

Chapter 3. Strong-coupling GL theory of ^3He in a periodic confined geometry	47
3.1. Strong-coupling Corrections	47
3.2. Strong-coupling phase diagram	51
Chapter 4. Line impurities and Nafen aerogels	56
4.1. Introduction	56
4.2. Ginzburg-Landau Theory	57
4.3. Impurity Lattice	58
4.4. Phase Diagram	60
4.5. Disorder in the Lattice	60
4.6. NMR and further models	62
Chapter 5. Publication: Superfluid phases of ^3He in nanoscale channels	66
5.1. Abstract	66
5.2. Introduction	67
5.3. Ginzburg-Landau Theory	68
5.4. Superfluid Phases	76
5.5. Phase Diagram	83
5.6. NMR Signatures	88
5.7. Summary and Outlook	99
5.8. Material Parameters	102
5.9. Acknowledgements	104
Chapter 6. Publication: Spontaneous Helical Order of a Chiral p -wave Superfluid Confined in Nanoscale Channels	106

6.1. Abstract	106
6.2. Introduction	107
6.3. Ginzburg-Landau Theory	108
6.4. Dynamical Instability	112
6.5. Double Helix Phase	116
6.6. Phase Diagram	116
6.7. NMR Signatures	118
6.8. Conclusions and Beyond ^3He	119
6.9. Appendix	121
Chapter 7. Publication: Strong-coupling and the Stripe phase of ^3He	124
7.1. Abstract	124
7.2. Introduction	124
7.3. Ginzburg-Landau Theory	126
7.4. Stripe phase	133
7.5. Stripe Phase Stability	139
7.6. NMR Signatures of the Stripe Phase	144
7.7. Summary and Outlook	150
Chapter 8. Strong-coupling: Superfluid ^3He as the precursor to an anti-ferromagnetic solid	151
8.1. Introduction	151
8.2. Free-energy functional	152
8.3. Frequency dependence of Δ	159

8.4. Experimental Inputs	160
8.5. Quasiparticle interaction potentials	162
8.6. Specific heat	164
8.7. Phase diagram	165
8.8. Ginzburg-Landau regime	167
8.9. Conclusion	168
References	170
Appendix A. Strong-coupling diagrams	180
Appendix B. Numerical Optimization with L-BFGS	183
Appendix C. Monte Carlo integration	190

List of Tables

- 4.1 Experimental parameters for the nafen aerogels with corresponding model parameters. The density, ρ , and the mean strand radius, r , are from Asadchikov et al.[**10**] 59
- 5.1 Material parameters for ^3He vs. pressure, with T_c from Ref. [**39**], v_f calculated with m^* from Ref. [**39**] and density n from Ref. [**101**]. Coherence lengths are calculated as $\xi_0 = \hbar v_f / 2\pi k_B T_c$. Strong-coupling $\Delta\beta_i^{\text{sc}}$ parameters at T_c in units of $|\beta_1^{\text{wc}}|$ are from Ref. [**23**]. 102
- 5.2 Coefficients of a polynomial fit to the strong-coupling β parameters from Ref. [**23**] of the form $\Delta\beta_i^{\text{sc}} = \sum_n a_n^{(i)} p^n$. 103
- 5.3 Sauls-Serene $\Delta\beta_i^{\text{sc}}$ parameters[**81**] for ^3He vs. pressure. The values at $p = 0$ bar were obtained by extrapolating the published $\Delta\beta_i^{\text{sc}}$, which were calculated only down to 12 bar, to their weak-coupling values at $\lim_{p \rightarrow p_0} T_c(p)/T_F(p) = 0$, which corresponds to a negative pressure of $p_0 = -5$ bar. 104
- 5.4 Coefficients of a polynomial fit to the Sauls-Serene β parameters in Table 5.3 of the form $\Delta\beta_i^{\text{sc}} = \sum_n a_n^{(i)} p^n$. 104

List of Figures

- 1.1 Bulk phase diagram adapted from Greywall's measurements[**39**] and including the self-consistently calculated T_{AB} points from this thesis. 22
- 2.1 Left panel: One-fourth of the unit cell showing the triangular computational grid. The grey region defines the area occupied by the post. Right panel: Order parameter amplitude, $A_{zz}(\vec{R})$, of the z-aligned polar phase for $L = 20 \xi_0$, $d = 8 \xi_0$, $T = 0.9T_c$, and $\hat{d} = \hat{z}$. The order parameter is real and scaled in units of the bulk B-phase order parameter, $\Delta_B(T)$. 38
- 2.2 Order parameter components of the B_{\square} phase plotted in the domain V for $L = 20 \xi_0$, $d = 12 \xi_0$, and $T = 0.7T_c$. All values are real and scaled by the bulk B-phase order parameter $\Delta_B(T)$. Note the reduced scale of the A_{xy} amplitude. 40
- 2.3 Order parameter amplitude as a function of the confinement length, D , for $L = 20\xi_0$ and $T = 0.7T_c$. The amplitudes are taken as the maxima within the domain. Note that maxima for A_{xx} and A_{yy} are equal, as are the maxima for A_{xy} and A_{yx} , but suppressed compared to A_{zz} . The dashed vertical line marks the 2nd order P_z to B_{\square} phase transition. 42
- 2.4 Phase diagrams for $L = 5\xi_0$ and $L = 20\xi_0$. The dashed curve is the normal to P_z transition obtained by the variational method. The solid curves are fits of the transition data points to the functional form

of the variational curve. Note that there is a range of confinement lengths, D , for which only the P_z phase is realized. 45

3.1 (Left) Experimental strong-coupling $\Delta\beta^{sc}$ s estimated by Choi et al[23] and plotted relative to their weak-coupling values. (Right) The bulk phase diagram showing the regions of stability of the A (green) and B (red) phases using the experimental β s with linear T scaling. The dashed line is the experimental A-B transition line terminating at the experimental PCP point. 49

3.2 (Left) Diagram for the array of posts showing its relevant dimensions: the post size d , the confinement length D , and the post spacing L . (Right) For purposes of plotting the superfluid order parameter, we shift the origin of the unit cell. 51

3.3 The \mathbf{A}_{C_2} order parameter for $T = 0$, $P = 30$ bar, $L = 80$ nm, and $D = 50$ nm in units of the bulk amplitude $\Delta_A^2 = -\alpha(T)/(4\beta_{245})$. The \hat{l} vector is overlaid on the plot for the polar amplitude $\Re A_{zz}$ 53

3.4 The domain structure for both the $s_{\mathbf{A}}$ and $s_{\mathbf{B}}$ phases. For $s_{\mathbf{A}}$, $\Delta_x = \Im A_{zx}$ and $\Delta_y = \Im A_{zy}$, while for $s_{\mathbf{B}}$, $\Delta_x = \Re A_{xx}$ and $\Delta_y = \Re A_{yy}$. The domain walls are analogous those of the stripe B phase in the slab geometry. 54

3.5 Phase diagram for the periodic geometry as a function of T and D with $P = 30$ bar, $L = 80$ nm, and maximal pairbreaking boundary conditions. These values of P and L were chosen to cleanly separate the five superfluid phases. 55

4.1 Polar order parameter at $p = 15$ bar and $T = 0.95T_c$ for the square lattice models of both nafen-90, left, and nafen-243, right, in units of $\Delta_P = \sqrt{|\alpha|/2\beta_{12345}}$. 60

- 4.2 Phase diagrams for nafen-72, nafen-90, and nafen-243, with points denoting the phase transitions observed by Dmitriev et al. The lines show the calculated transitions on the square lattice using the parameters in Table 4.1. 61
- 4.3 Polar order parameter at $p = 15$ bar and $T = 0.95T_c$ for the disordered supercell model of Nafen-90 in units of $\Delta_P = \sqrt{|\alpha|/2\beta_{12345}}$. 62
- 4.4 Nafen-90 phase diagram comparing the square lattice (solid lines) to the disordered cell (dashed lines) of Fig. 4.3. 63
- 4.5 Calculated NMR frequency shifts for three different models of nafen-90 impurities compared to the experimental measurements by Dmitriev et al.[29] The “modified-Lévy” curve model is described in the text. 64
- 4.6 Impurity distribution for the “modified Lévy” model used in Fig. 4.5 65
- 4.7 Volume fraction of the polar distorted A phase in the “modified Lévy” supercell as a function of temperature. 65
- 5.1 The bulk phase diagram showing the regions of stability of the A (blue) and B (red) phases using the experimental β s with linear T scaling. The dashed line is the experimental A-B transition line terminating at the experimental PCP point. 72
- 5.2 Order parameter amplitudes for the P_z phase as a function of r at $p = 26$ bar and $T = 0.5 T_c$ for retro-reflection (maximal pair-breaking), diffuse ($b'_T = 0.54$), and specular (minimal pair-breaking) boundary conditions. Values are scaled by the unconfined polar phase amplitude $\Delta_P^2 = |\alpha(T)|/2\beta_{12345}$. For minimal pairbreaking boundary conditions the P_z phase is spatially homogeneous within the pore. 78
- 5.3 Order parameter amplitudes for the $B_{\text{SO}(2)}$ phase as a function of r at $p = 26$ bar and $T = 0.5 T_c$. The left figure depicts maximal pairbreaking ($b'_T = 0$) while the right shows minimal pairbreaking

($b'_T = \infty$). Values are scaled by the bulk B phase order parameter, $\Delta_B^2 = |\alpha(T)|/6(\beta_{12} + 1/3\beta_{345})$. 89

5.4 Order parameter amplitudes for the $A_{\text{SO}(2)}$ phase as a function of r at $p = 26$ bar and $T = 0.5 T_c$. The left figure depicts maximal pairbreaking while the right shows minimal pairbreaking. Values are scaled by the bulk A phase order parameter, $\Delta_A^2 = |\alpha(T)|/4\beta_{245}$. 81

5.5 Chiral axis \hat{l} for the $A_{\text{SO}(2)}$ phase at $p = 26$ bar, $T = 0.5 T_c$, and minimal pairbreaking boundaries. Arrow lengths are scaled by $|\Delta_\phi|$. 81

5.6 Dominant order parameter amplitudes for the A_{C_2} phase at $p = 26$ bar and $T = 0.5 T_c$. The left figure depicts maximal pairbreaking while the right shows minimal pairbreaking. Values are scaled by the bulk A phase amplitude $\Delta_A^2 = |\alpha(T)|/4\beta_{245}$. 82

5.7 Chiral axis \hat{l} for the A_{C_2} phase at $p = 26$ bar and $T = 0.5 T_c$. (Left) Maximal pairbreaking boundaries result in a nearly uniform \hat{l} direction. (Right) Minimal pairbreaking, on the other hand, gives the characteristic ‘‘Pan Am’’ configuration. Arrow lengths are scaled by $(\Delta_r^2 + \Delta_\phi^2)^{1/2}$. 82

5.8 Phase diagrams for $b'_T = 0$ (maximal pairbreaking) and $b'_T = 0.1$. The $A_{\text{SO}(2)}$ phase does not appear at all for maximal pairbreaking; as pairbreaking at the boundary is relaxed it is stabilized at high pressure and displaces the $B_{\text{SO}(2)}$ and A_{C_2} phases. 84

5.9 Phase diagrams for $b'_T = 0.54$ and $b'_T = \infty$ (minimal pairbreaking). As pairbreaking decreases, the A_{C_2} phase is suppressed completely and the stable range of the $B_{\text{SO}(2)}$ phase is decreased significantly. For minimal pairbreaking the $A_{\text{SO}(2)}$ phase onsets at $T = T_c$ with the P_z phase absent. 85

- 5.10 Temperature-confinement phase diagram for fixed $b'_T = 0.1$, $p = 26$ bar and the β parameters of Ref. [23]. 86
- 5.11 Phase diagram for $b'_T = 0.1$ using the β parameters of Sauls and Serene.[81] The resulting phase boundaries are largely left unchanged except for the shift upward in pressure of the tricritical point, roughly corresponding to the difference of the Choi et al[23] polycritical point, $p_{\text{PCP}} \approx 21$ bar, and the Sauls and Serene polycritical point, $p_{\text{PCP}} \approx 28$ bar. 87
- 5.12 Frequency shift of the $\text{A}_{\text{SO}(2)}$ phase at $p = 26$ bar, $T = 0.5 T_c$, and $b'_T = 0$. The P_z phase has the same functional form, but with larger amplitude. 92
- 5.13 Transverse frequency shifts for the A_{C_2} phase with $\vec{H} \parallel \hat{z}$ at $p = 26$ bar, temperatures $T = 0.5 - 0.8 T_c$, and maximal pairbreaking with $b'_T = 0$. 94
- 5.14 Transverse frequency shifts for the A_{C_2} phase with $\vec{H} \perp \hat{z}$ at $p = 26$ bar, temperatures $T = 0.5 - 0.8 T_c$, and maximal pairbreaking with $b'_T = 0$. The left panel shows the shifts for in-plane field orientation $\varphi = 0$ (blue), and $\varphi = \pi/2$ (red). The right panel shows the shifts for $\varphi = \pi/4$, which has the same functional form as that of the $\text{A}_{\text{SO}(2)}$ phase. 96
- 5.15 Transverse frequency shifts for the $\text{B}_{\text{SO}(2)}$ phase at $p = 10$ bar, temperatures $T = 0.1 T_c, 0.2 T_c, 0.3 T_c, 0.36 T_c$, and maximal pair-breaking, $b'_T = 0$. 98
- 6.1 Left: The chiral axis $\hat{l}(\mathbf{r})$ for the A_{C_2} phase at $p = 26$ bar, $T = 0.7 T_c$ with strong pairbreaking ($b'_T = 0.1$). The chiral axis is confined in the $r - \phi$ plane. The arrow color density is scaled by the amplitude, $(\Delta_r^2 + \Delta_\phi^2)^{1/2}$. The red and blue dots locate the two disgyrations, which support supercurrents propagating along $+z$ and $-z$, respectively.

- Right: Supercurrent isosurfaces in the $S_{\mathbf{A}}$ phase, calculated using the full order parameter in Eq. 6.13 of the Appendix. 110
- 6.2 NG mode dispersion, ω_- , as a function of Q and T and scaled by the bulk A-phase amplitude at $p = 26$ bar and $R = 100$ nm. Negative values denote imaginary values of ω_- . The circles indicate the most unstable mode, Q/Q_c , for each temperature. $Q_c \approx \pi/674$ nm = 4.66×10^{-3} nm $^{-1}$ is the maximum value of the most unstable mode at the $S_{\mathbf{A}}$ - $P_{\mathbf{z}}$ transition. 113
- 6.3 (Left) The amplitudes Δ'_z , (red); Δ''_r , (blue); and Δ''_z , (green) for the $S_{\mathbf{A}}$ order parameter phase, at $p = 26$ bar, $R = 100$ nm and scaled by the bulk A phase amplitude $\Delta_A = \sqrt{|\alpha(T)|/4\beta_{245}}$. The black vertical lines denote the continuous phase transitions A_{C_2} - $S_{\mathbf{A}}$, $S_{\mathbf{A}}$ - $P_{\mathbf{z}}$, and $P_{\mathbf{z}}$ -Normal with increasing temperature. (Right) The temperature dependence of the half-period L . 115
- 6.4 Phase diagram for the cylindrical channel with $R = 100$ nm and strong pairbreaking, $b'_T = 0.1$. The labels $S_{\mathbf{A}}$ and $s_{\mathbf{B}}$ correspond to the helical and B-like stripe phases, respectively. The $A_{SO(2)}$ phase appears at the highest pressures, and the A_{C_2} phase is suppressed by the more stable $S_{\mathbf{A}}$ phase. The $s_{\mathbf{B}}$ phase appears in a narrow region at low pressure and low temperature. 117
- 6.5 Small tipping angle ($\beta \approx 0$) transverse frequency shift for the $S_{\mathbf{A}}$ phase as a function of temperature. The $S_{\mathbf{A}}$ phase order parameter is that shown in Fig. 6.3. The $S_{\mathbf{A}}$ and $P_{\mathbf{z}}$ frequency shifts are found using Eq. 6.12, and the A_{C_2} frequency shifts are given by Eqs. 36 and 37 in Ref. [104]. The grey shaded region denotes the region of the $S_{\mathbf{A}}$ phase where the half-period L exceeds $\xi_D \approx 10$ μ m. 120
- 6.6 Phase diagram for the cylindrical channel with $R = 100$ nm and $b'_T = 0$ (maximal pairbreaking). The $S_{\mathbf{A}}$ phase has displaced much of

- the A_{C_2} phase compared to the phase diagram calculated for only z translationally invariant phases [104]. 122
- 6.7 Phase diagram: temperature versus radius for cylindrical channel at $p = 26$ bar with strong pairbreaking. $b'_T = 0.1$. All six phases we have found are shown in this diagram, although the s_B phase is stable in a very narrow window of R and T . 123
- 7.1 (Left) Bulk phase diagram with lines showing the measured phase transitions and shading showing the calculated regions of phase stability based on GL theory. The $\Delta\beta_i^{sc}$ coefficients are from Choi et al[23] and are plotted in the right panel. 129
- 7.2 (Left) Bulk phase diagram where the shaded regions represents the phases calculated from GL theory with the $\Delta\beta_i^{sc}$ of Sauls & Serene [81]. These strong-coupling corrections are plotted in the right panel. 130
- 7.3 Comparison of the phase diagrams calculated within weak-coupling quasiclassical theory (blue and orange lines), weak-coupling GL theory (dashed lines), and weak-coupling GL theory with D rescaled by $\xi_{GL}(T)/\xi_{\Delta}(T)$ (solid black lines). 132
- 7.4 Stripe phase order parameter for specular surfaces as functions x and z for $D = 12\xi_0$, $p = 3$ bar, $T = 0.5T_c$, and calculated period $L \approx 23.6\xi_0$. The amplitudes are scaled in units of the bulk B phase order parameter, $\Delta_B = \sqrt{|\alpha(T)|/6(\beta_{12} + 1/3\beta_{345})}$. 134
- 7.5 Energy density of the Stripe phase with specular surfaces for $D = 12\xi_0$, $p = 3$ bar, $T = 0.5T_c$, and calculated period $L \approx 23.6\xi_0$. The energy density f is scaled by the unconfined bulk energy density $f_B = \frac{1}{2}\alpha(T) \Delta_B(T)^2 < 0$, and is also shown separated into bulk and gradient contributions. 136

- 7.6 Temperature and pressure dependence of the wavenumber Q for film thicknesses $D = 11 \xi_0$, with no Stripe to B transition (left panel), and $D = 11.5 \xi_0$, with a Stripe to B transition (right panel). The onset of the Stripe transition is based on the Planar-Stripe instability, i.e. omitting the A phase. 139
- 7.7 Pressure-temperature-confinement phase diagram for the film with minimal pairbreaking boundaries and experimental strong-coupling corrections. The A phase is stable everywhere not excluded by the Stripe and B phases. 140
- 7.8 Pressure-temperature phase diagram for a film of thickness $D = 700$ nm with minimal pairbreaking (specular) boundary conditions. The A phase is stable everywhere in the white region below the bulk transition temperature. The larger yellow circles are data for the A-B transition based on NMR from Levitin et al obtained with ^4He preplating [50]. 141
- 7.9 Pressure-temperature phase diagram for a film of thickness $D = 1080$ nm with minimal pairbreaking boundaries. The A phase is stable everywhere not excluded by the Stripe and B phases. 143
- 7.10 Temperature-confinement phase diagram for films at $p = 3$ bar with the Choi et al. strong-coupling corrections. Results for three boundary conditions are shown: minimal pairbreaking, $b'_T \rightarrow \infty$ (solid); diffuse, $b'_T = 0.54$ (dashed); and maximal pairbreaking, $b'_T = 0$ (dotted). For diffuse and maximal pairbreaking, the suppression of the A to Normal phase transitions are also shown. 146
- 7.11 Transverse NMR frequency shifts as a function of tipping angle β at $D = 12\xi_0$, $p = 3$ bar, and $T = 0.5 T_c$, with minimal pairbreaking for the B^\pm and S^\pm states. 148

- 8.1 Φ diagrams. Diagram (a) generates the usual BCS weak-coupling theory, while diagrams (b) to (h) are next order corrections at $(T_c/T_F)^3$ which contribute to Φ_{sc} and are described further in Appendix A. 158
- 8.2 The relative order parameter amplitude for the bulk A and B phases as a function of Matsubara index m . The red circles (B phase) and blue squares (A phase) are calculated self-consistently and have nearly identical frequency dependence. The dashed black line is the Lorentzian function with width $\omega_{sf} = 1.14\omega_{ff}$ where ω_{ff} is the spectral width of the pairing interaction. 161
- 8.3 The spin-dependent interaction potential $j(q)$ and the spin-independent potential $v(q)$ at pressures from 0 to 34 bar. The curvature variations of the potentials with pressure at small q appear to largely be artifacts of the underconstrained functional forms. The vertical dashed line is the value of q that corresponds to the solid ^3He lattice constant at 34 bar. 163
- 8.4 Superfluid specific heat as a function of temperature at 34 bar, for both A and B phases, as calculated self-consistently with the strong-coupling free-energy functional (solid lines) and as measured by Greywall[39] (squares and circles). 165
- 8.5 Fractional differences between the calculated superfluid specific heat and Greywall's measurements. For temperatures below the vertical line at $T \sim 0.8$ mK the temperature calibration for the experiment becomes significantly more uncertain. 166
- 8.6 Bulk phase diagram adapted from Greywall's measurements[39] and including the self-consistently calculated T_{AB} points. 167
- 8.7 Corrections to the fourth-order β coefficients for the ^3He Ginzburg-Landau free-energy functional. These corrections are qualitatively similar to those calculated by Sauls and Serene.[81] 168

- C.1 Probability densities generated by Foam in comparison to the exact function, two gaussians on a diagonal. Brighter points are higher probability. 192
- C.2 Probability densities generated by Foam in comparison to the exact function, a Marr wavelet. Brighter points are higher probability. 193

CHAPTER 1

Introduction

Despite being almost solely produced as a byproduct of decaying nuclear weapons stockpiles through the beta-decay of tritium, ^3He has had a surprisingly large impact on physics in the 20th and 21st centuries. As bulk quantities of purified liquid ^3He became possible in the 1950s it became an exemplary experimental model for normal Fermi liquids. In the 1960s, the first Helium dilution refrigerators were realized using ^3He diluted into ^4He , which became critical parts of ultra low temperature physics.[102] The superfluidity of ^3He was only first confirmed in 1972 when Osheroff, Richardson, and Lee were able to cool a sample below 2.7 mK.[68, 67] Since then, superfluid ^3He has become the model (and only confirmed) p -wave Fermi superfluid, with unsurpassable purity and multiple stable phases even in the bulk liquid, shown in Figure 1.1.

The stable A and B phases, as first named by Osheroff et al[68], can be understood in terms of their symmetries. The bulk normal Fermi liquid has the maximal symmetry group

$$(1.1) \quad \mathbf{G} = \mathbf{U}(1)_{\text{N}} \times \mathbf{SO}(3)_{\text{S}} \times \mathbf{SO}(3)_{\text{L}} \times \mathbf{P} \times \mathbf{T},$$

which is the product of global gauge rotations, spin rotations, orbital rotations, space inversion, and time-reversal, respectively. This maximal symmetry group is spontaneously broken by the superfluid transition, with distinct residual symmetries for each phase.

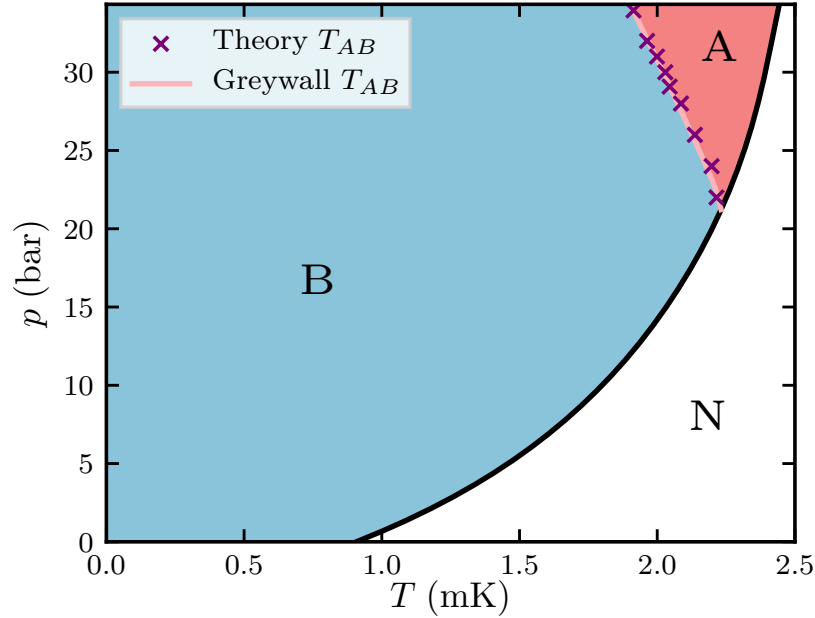


Figure 1.1. Bulk phase diagram adapted from Greywall’s measurements[**39**] and including the self-consistently calculated T_{AB} points from this thesis.

The lower temperature B phase was first described by Balian and Werthamer[**13**] and has the residual symmetry group

$$(1.2) \quad \mathbf{H} = \text{SO}(3)_{L+S} \times \mathbf{T},$$

consisting of joint spin and orbital rotations combined with time reversal symmetry. This phase is also known as the “isotropic” phase and its order parameter belongs to a $J = 0$ representation.

The A phase appears only above $p_{\text{PCP}} \approx 21.22$ bar and near T_c . It was identified with the spin-triplet, p -wave phase first discussed by Anderson together with Morel[**8**] and later Brinkman[**7**]. Its residual symmetry group is

$$(1.3) \quad \mathbf{H} = \text{SO}(2)_{S_d} \times \mathbf{Z}_2^{\text{spin}} \times \text{SO}(2)_{L_z - \Phi}$$

which consists of spin rotations about an axis \hat{d} and a joint gauge and orbit symmetry consisting of an orbital rotation of angle $\alpha \in \text{SO}(2)_{L_z}$ about the angular momentum axis \hat{l} combined with a gauge transformation $-\alpha \in \text{U}(1)_N$. This phase is $S = 0$ and $L = 1$, meaning it carries a groundstate angular momentum.[77]

While it is remarkable enough that the bulk superfluid supports these two phases, most of this thesis will be devoted to identifying potentially new phases by distorting the bulk. In particular, placing ^3He in a confining geometry reduces the maximal orbital symmetry, eliminating the exact bulk phases and leading to novel phase diagrams. The nature of the stabilized phases may be chosen by varying the confining geometry along with the temperature and pressure.

Determining the precise nature of a novel phase requires a good understanding of the basic interactions that lead to the bulk superfluid as well as a model for the confining boundary. Although we have a good qualitative understanding of both of these, certain quantitative aspects have evaded theorists. In particular, the bulk phase diagram itself is quite difficult to calculate within a microscopic model due to both uncertainties in the underlying quasiparticle interactions and computational challenges. In Chapter 8 we present the first precise microscopic calculation of the bulk superfluid ^3He phase diagram. In doing so, we find evidence that superfluid ^3He is governed by competing ferromagnetic and almost-localized antiferromagnetic exchange interactions. We also obtain new evidence that ^3He is an almost localized Fermi liquid in the sense of being near a Mott transition.

CHAPTER 2

Publication: Superfluid phases of ^3He in a periodic confined geometry

2.1. Abstract

Predictions and discoveries of new phases of superfluid ^3He in confined geometries, as well as novel topological excitations confined to surfaces and edges of near a bounding surface of ^3He , are driving the fields of superfluid ^3He infused into porous media, as well as the fabrication of sub-micron to nano-scale devices for controlled studies of quantum fluids. In this report we consider superfluid ^3He confined in a periodic geometry, specifically a two-dimensional lattice of square, sub-micron-scale boundaries (“posts”) with translational invariance in the third dimension. The equilibrium phase(s) are inhomogeneous and depend on the microscopic boundary conditions imposed by a periodic array of posts. We present results for the order parameter and phase diagram based on strong pair breaking at the boundaries. The ordered phases are obtained by numerically minimizing the Ginzburg-Landau free energy functional. We report results for the weak-coupling limit, appropriate at ambient pressure, as a function of temperature T , lattice spacing L , and post edge dimension, d . For all d in which a superfluid transition occurs, we find a transition from the normal state to a periodic, inhomogeneous “polar” phase with $T_{c1} < T_c$ for bulk superfluid ^3He . For fixed lattice spacing, L , there is a critical post dimension, d_c , above which only the periodic polar phase is stable. For $d < d_c$ we find a

second, low-temperature phase onsetting at $T_{c_2} < T_c$ from the polar phase to a periodic “B-like” phase. The low-temperature phase is inhomogeneous, anisotropic and preserves time-reversal symmetry, but unlike the bulk B-phase has only D_{4h}^{L+S} point symmetry.

2.2. Introduction

The p-wave, spin-triplet superfluid phases of ^3He provide the paradigm for unconventional BCS pairing in which spin and orbital rotation symmetries, $\text{SO}(3)_S \times \text{SO}(3)_L$, are spontaneously broken in conjunction with $U(1)_N$ gauge symmetry. It was realized soon after the discovery that these broken symmetries, particularly parity and orbital rotation symmetry, implied that interfaces, boundaries and impurities could have profound effects on the superfluid phases.[5, 73] In the case of the bulk A-phase the effect of the boundary is to *lock* the orbital quantization axis, \hat{l} , normal to the boundary. The influence of boundaries can often extend to length scales much longer than the coherence length, $\xi_0 = \hbar v_f / 2\pi k_B T_c \approx 200 - 800 \text{ \AA}$ depending on pressure, when there is competition between alignment effects from curved boundaries and/or superflow.[26] In a long cylinder with radius $R \gg \xi_0$ the boundary condition on \hat{l} leads to a *texture*, i.e. a long-wavelength spatial variation of the orbital quantization axis, \hat{l} , which is also an equilibrium current-carrying state.[57, 100, 46] At the coherence length scale near a boundary strong pair-breaking typically occurs. The orbital component of the order parameter normal to the surface is suppressed and a spectrum of Fermionic states are localized near the boundary.[21, 62, 98] The de-pairing effect of the boundary is further enhanced if the surface is rough on length scales comparable to or smaller than ξ_0 . If superfluid ^3He is confined to a region with dimensions of order a few coherence lengths then the geometry and surface

structure on the boundaries can significantly modify the equilibrium phase diagram, and can even stabilize phases not realized in bulk superfluid ^3He .[\[45, 62, 98, 99\]](#)

Several studies of superfluid ^3He have been performed on thin films or within a slab geometry.[\[34, 107, 84\]](#) In the case of strong one-dimensional confinement, i.e. boundary separation $D < D_{c_2} \approx 9\xi_0$, the A phase is expected to be the stable phase even at pressures well below the bulk critical pressure, $p_c \approx 21$ bar.[\[98\]](#) Nuclear magnetic resonance (NMR) measurements strongly support this prediction.[\[50\]](#) This is in stark contrast to the bulk ^3He phase diagram in which the A phase is only stable at high temperature and pressure. In weak-coupling theory the planar and axial (ABM) phases are degenerate even with strong surface disorder.[\[98\]](#) Strong-coupling effects which stabilize the Anderson-Brinkman-Morel (ABM) state at high pressures and high temperatures are poorly known for inhomogeneous phases at low-temperatures, $T \ll T_c$, and low pressures, $p \rightarrow 0$ bar. For this reason the ground state of thin ^3He films at the lowest pressures is still an open question. At intermediate scales of confinement, $D_{c_2} < D < D_{c_1} \approx 13\xi_0$, the ground state in the weak-coupling limit is predicted to be a “crystalline” phase with an order parameter that spontaneously breaks translation symmetry in the plane of the film.[\[99\]](#) A one-dimensional periodic phase (“striped phase”) with in-plane wavelength $Q_{\perp}^{-1} \approx 3\xi_0$ has lower energy than any of the translationally invariant axial, planar or B-planar phases over a wide range of film thicknesses and temperatures. The mechanism responsible for spontaneously breaking translation symmetry for $D \lesssim D_{c_1}$ is the energy cost of surface pair-breaking compared to the energy cost for domain wall formation between degenerate B-planar phases. For $D < D_{c_1}$ it is energetically favorable for domain walls to enter the film. Interactions between domain walls lead to the striped phase. This type of

competition between surface pair-breaking, the formation of topological defects and the stabilization of new phases not realized in bulk ^3He is part of the motivation for developing sub-micron to nano-scale geometries for confining ^3He . [50, 35] Of particular interest for this study is the possibility of confining ^3He in a periodic geometry such as a cavity supported by a periodic array of sub-micron scale posts. [108]

We break translational symmetry externally by considering ^3He infused into an infinite two-dimensional ($x - y$) periodic array of square posts, with translational invariance in the third dimension (z). This geometry can also be viewed as a two-dimensional ($2d$) grid formed of vertical (x) and horizontal (y) channels. The spatial region between the corners of four adjacent posts, or alternatively where the x and y channels intersect is particularly significant, and we will refer to this region as the “center” of the $2d$ cell when discussing superfluid ^3He confined within this structure. We expect the results reported here to be valid for confinement lengths in the z dimension, satisfying $L_z \gg 30\xi_0$.

The order parameter for superfluid ^3He belongs to the manifold of spin-triplet, p-wave, BCS pairing states represented by the 2×2 “gap matrix”,

$$(2.1) \quad \hat{\Delta}(\hat{p}) = \sum_{\alpha i} (i\sigma_\alpha \sigma_y) A_{\alpha i} \hat{p}_i,$$

which is a function of the direction of relative momentum of the Cooper pair, \hat{p} , and is parametrized in its most general form by nine complex amplitudes, $A_{\alpha i}$. The 3×3 matrix order parameter transforms as a vector under spin rotations, and separately as a vector under orbital rotations. The maximal symmetry group for bulk ^3He is $\mathbf{G} = \text{U}(1)_N \times \text{SO}(3)_S \times \text{SO}(3)_L \times \text{P} \times \text{T}$, where P, T and $\text{U}(1)_N$ represent space inversion, time-reversal and global gauge symmetries of the normal phase. The symmetry reduction resulting from

the weak nuclear dipolar interaction is omitted here, but is important in resolving relative spin-orbit rotational degeneracies, and in determining the NMR signatures of the phases of confined ^3He .

2.3. Ginzburg-Landau Theory

To determine the phase diagram and superfluid order parameter for ^3He confined within a $2d$ periodic structure we minimize the Ginzburg-Landau (GL) free energy for a general spin-triplet, p-wave condensate defined as a functional of the 3×3 matrix order parameter. A few atomic units away from a boundary the ^3He - ^3He interactions responsible for pairing are invariant under the maximal symmetry group of bulk ^3He . Thus, the GL functional takes its bulk form,[**72**, **93**]

$$\begin{aligned}
 \Omega[A] = \int_V d\vec{R} \left\{ \alpha(T) \text{Tr}(AA^\dagger) + \beta_1 |\text{Tr}(AA^T)|^2 + \beta_2 [\text{Tr}(AA^\dagger)]^2 \right. \\
 (2.2) \quad & + \beta_3 \text{Tr}[AA^T(AA^T)^*] + \beta_4 \text{Tr}[(AA^\dagger)^2] + \beta_5 \text{Tr}[AA^\dagger(AA^\dagger)^*] \\
 & \left. + K_1 (\nabla_k A_{\alpha j} \nabla_k A_{\alpha j}^*) + K_2 (\nabla_j A_{\alpha j} \nabla_k A_{\alpha k}^*) + K_3 (\nabla_k A_{\alpha j} \nabla_j A_{\alpha k}^*) \right\}.
 \end{aligned}$$

The equilibrium order parameter is obtained from the stationarity condition for the GL functional. Confinement is introduced via boundary conditions of the order parameter field, $A_{\alpha i}(\vec{R})$. For ^3He confined in a non-magnetic, periodic geometry with 4-fold rotational, reflection and inversion symmetries, the maximal symmetry group is reduced by restricting the orbital rotations to the point group D_{4h} (which includes space inversion), i.e.

$$(2.3) \quad \mathbf{G} = \mathbf{U}(1)_N \times \mathbf{SO}(3)_S \times D_{4h} \times \mathbf{T}.$$

The domain, V , is a square unit cell with side length L . Periodic boundary conditions are imposed on the order parameter field at the outer boundaries of this unit cell. In the interior of the unit cell is an inner boundary representing the square post of side length d . Typical boundary conditions for the order parameter on the inner boundary are: (i) *maximal* pair-breaking in which all components of the order parameter vanish on the inner boundary and (ii) *minimal* pair-breaking in which only the orbital component normal to the surface of the inner boundary is forced to vanish, and the normal derivative of the tangential orbital components vanishes on the inner boundary. This latter boundary condition corresponds to surfaces with specular reflection,[5] while the former boundary condition corresponds to an atomically rough surface with strong backscattering.[77] Here we report results based on maximal pair-breaking. We numerically minimize the GL functional on this domain, and determine the stable (and in some cases meta-stable) order parameter (phases) for superfluid ^3He in this class of periodic confined geometries. We also present results for the phase diagram as a function of temperature T , confinement length $D \equiv L - d$, and period L . The results reported here are appropriate for low pressures in the GL regime. Thus, we assume weak-coupling values for the GL material parameters:[72, 93]

$$(2.4) \quad \begin{aligned} \alpha(T) &= \frac{1}{3}N(0)(T/T_c - 1), & 2\beta_1 &= -\beta_2 = -\beta_3 = -\beta_4 = \beta_5, \\ K_1 = K_2 = K_3 &= \frac{3}{5}N(0)\xi_0^2, & \beta_1 &= -\frac{N(0)}{(\pi k_B T_c)^2} \left\{ \frac{1}{30} \left[\frac{7}{8}\zeta(3) \right] \right\}, \end{aligned}$$

where T_c is the superfluid transition temperature for bulk ^3He , $\xi_0 = \hbar v_f / 2\pi k_B T_c$ is the zero-temperature correlation length, and $N(0) = k_f^3 / 2\pi^2 v_f p_f$ is the single-spin quasiparticle density of states at the Fermi surface, defined in terms of the Fermi velocity, v_f , and Fermi momentum and wavenumbers, $p_f = \hbar k_f$.¹

In what follows we neglect the nuclear dipolar energy and choose *aligned* spin and orbital coordinate axes, $\{x, y, z\}$, corresponding to the high symmetry directions of the periodic channel. Thus, the order parameter is represented by,

$$(2.5) \quad A = \begin{pmatrix} A_{xx} & A_{xy} & A_{xz} \\ A_{yx} & A_{yy} & A_{yz} \\ A_{zx} & A_{zy} & A_{zz} \end{pmatrix}.$$

For bulk ^3He , the B-phase, defined by the Balian-Werthamer state,

$$(2.6) \quad A^{\text{B}} = \frac{\Delta_{\text{B}}}{\sqrt{3}} \begin{pmatrix} 1 & 0 & 0 \\ 0 & 1 & 0 \\ 0 & 0 & 1 \end{pmatrix},$$

with amplitude given by

$$(2.7) \quad \Delta_{\text{B}}^2(T) = \frac{1}{2} \frac{|\alpha(T)|}{\beta_{12} + \frac{1}{3}\beta_{345}},$$

is the equilibrium phase at low pressures with free energy density given by

$$(2.8) \quad \Omega_{\text{B}}/V = -\frac{1}{4} \frac{|\alpha(T)|^2}{\beta_{12} + \frac{1}{3}\beta_{345}} = -\frac{\Delta C_{\text{B}}}{2T_c} (T - T_c)^2,$$

¹This published definition of K_i is incorrect, it should be $K_1 = K_2 = K_3 = \frac{7\zeta(3)}{60} N(0) \xi_0^2$

where the notation refers to summation as $\beta_{ijk} \equiv \beta_i + \beta_j + \beta_k$. The second term is the B-phase condensation energy scaled in terms of the heat capacity jump, ΔC_B , at the normal to B-phase transition. For weak-coupling values of the material coefficients this gives the BCS result, $\Delta C_B/C_N = 12/\zeta(3)7 \simeq 1.43$, where $C_N = \frac{2}{3}\pi^2 N(0) T_c$ is the normal-state heat capacity at T_c . These values for the bulk B-phase order parameter and free energy are used as the scale for the order parameter and free energy of confined ${}^3\text{He}$.

We note that the boundary condition imposed by an interior post is expected to be accurate only for post side lengths $d \gtrsim \xi_0$. For post dimensions, $d \ll \xi_0$, the boundary is more accurately treated microscopically as an ‘‘impurity’’ that scatters excitations and breaks pairs.[73] The pair-breaking effect of an impurity with side dimension smaller than a coherence length is reduced by d/ξ_0 near the post. We avoid this limit and restrict our analysis to post dimensions with $d \geq \frac{1}{2}\xi_0$.²

Before discussing the numerical results we describe some of the possible phases with a high degree of residual symmetry, i.e. sub-groups of the maximal symmetry group, that may be realized by ${}^3\text{He}$ in a confined D_{4h} geometry.

2.4. Symmetry Classes of ${}^3\text{He}$ in a confined D_{4h} geometry

The effects of confinement are enforced by the boundary conditions imposed on the order parameter. The boundary conditions reflect the point symmetry of the confining boundaries. For the case of a periodic array of square posts the elementary symmetry group of a square post, C_{4v} , is the combined set of four-fold rotations, $\{E, C_4, C_4^2, C_4^3\}$, where E is the identity and $C_4^n = (C_4)^n$ is a rotation about the z axis by $n \times \pi/2$, the set of reflections through four vertical planes, $\{\Pi_{zx}, \Pi_{zy}, \Pi_{zx'}, \Pi_{zy'}\}$, and the corresponding

²In Chapter 4 we consider a related model using line impurities with $d \ll \xi_0$

rotary reflections, $\{R_{zi} \equiv C_4 \Pi_{zi} \mid i = x, y, x', y'\}$, where (x', y') are axes rotated from (x, y) by $\pi/4$ about z . The addition of reflection symmetry through the horizontal plane, Π_{xy} , and 180° rotations about the vertical plane symmetry axes, $\{C_{2x}, C_{2y}, C_{2x'}, C_{2y'}\}$, defines the point group, D_{4h} , which includes space inversion, $C_i = C_{2y} \cdot \Pi_{zx}$.

For any element $g \in D_{4h}$ a scalar function transforms as $f(\vec{R}) \xrightarrow{g} f(\hat{g}^T \cdot \vec{R})$, where \hat{g} is the 3×3 matrix representing the symmetry element g , $\hat{g}^T = \hat{g}^{-1}$ is the matrix inverse, and $\vec{R} = (x, y)$. Thus, the order parameter field, which is a vector under space rotations and reflections, transforms as $A_{\alpha i}(\vec{R}) \xrightarrow{g} g_{ij} A_{\alpha j}(\hat{g}^T \cdot \vec{R})$. Similarly, for any rotation $g \in \mathbf{SO}(3)_S$ we have, $A_{\alpha i}(\vec{R}) \xrightarrow{g} g_{\alpha\beta} A_{\beta i}(\vec{R})$, and under a gauge transformation, $\chi \in \mathbf{U}(1)_N$, $A_{\alpha i}(\vec{R}) \xrightarrow{\chi} e^{-i\chi} A_{\alpha i}(\vec{R})$. Time-reversal, \mathbf{T} , reduces to complex conjugation, $A_{\alpha i}(\vec{R}) \xrightarrow{\mathbf{T}} A_{\alpha i}^*(\vec{R})$.

2.4.1. Non-Equal Spin Pairing - The B_{\square} Phase

In the case of bulk ^3He the maximal symmetry sub-group of joint spin and orbital rotations combined with time-reversal, $\mathbf{SO}(3)_{L+S} \times \mathbf{T}$, is the symmetry class of the B-phase, i.e. the Balian-Werthamer state with $A_{\alpha i}^{\text{BW}} = \Delta \delta_{\alpha i}$. The *discrete analog* of the bulk B-phase is a state, which we refer to as the B_{\square} -phase, that is invariant under joint spin and orbital elements of the maximal point group, D_{4h} , and time-reversal, i.e. $H_{B_{\square}} = D_{4h}^{\text{L+S}} \times \mathbf{T}$. Note that space inversion is broken, but space inversion combined with inversion in spin-space is a symmetry of the B_{\square} -phase.

The matrix structure of the B_{\square} order parameter differs substantially from the isotropic B -phase. For all $g \in H_{B_{\square}}$, the order parameter satisfies,

$$(2.9) \quad A_{\alpha i}(\vec{R}) \xrightarrow{g} g_{\alpha\beta} A_{\beta j}(\hat{g}^T \cdot \vec{R}) g_{ji}^T = A_{\alpha i}(\vec{R}).$$

It is then straightforward to show that

$$(2.10) \quad A^{B_{\square}} = \begin{pmatrix} A_{xx} & A_{xy} & 0 \\ A_{yx} & A_{yy} & 0 \\ 0 & & A_{zz} \end{pmatrix},$$

with $A_{xx}(x, y) = A_{yy}(y, x)$, $A_{xy}(x, y) = A_{yx}(y, x)$, $A_{zz}(x, y) = A_{zz}(y, x)$ and all components are real (\mathbb{T} symmetry). The diagonal (off-diagonal) components are even (odd) under $x \rightarrow -x$ or $y \rightarrow -y$. The numerical results presented below show that the B_{\square} -phase is the equilibrium state in the weak-coupling limit at low temperatures.

2.4.2. Equal Spin Pairing States

The superfluid phases with the highest degree of residual symmetry are those that preserve a continuous rotation symmetry about an axis \hat{d} in spin space, i.e. $\text{SO}(2)_{\text{S}_d}$. The direction \hat{d} is a vector representing spontaneously broken spin-rotation symmetry. If \hat{d} is real, then the broken symmetry phase is an equal-spin-pairing (ESP) state and \hat{d} is the direction in which the Cooper pairs have zero spin projection. The residual symmetry group of the class of ESP states includes $\text{SO}(2)_{\text{S}_d} \times \mathbb{Z}_2^{\text{spin}}$, where $\mathbb{Z}_2^{\text{spin}} = \{1, e^{i\pi} R_{\pi \hat{x}}^{\text{spin}}\}$ is a two element group of the identity and the combined operation of a gauge transformation, $e^{i\pi}$, and a rotation of π about an axis $\hat{x} \perp \hat{d}$ in spin space. Continuous $\text{U}(1)_{\text{N}}$ symmetry is broken,

but elements of $U(1)_N$ may be combined with spin or orbital rotations and reflections. In particular, the point symmetry, D_{4h} , is necessarily broken by any p-wave pairing state. However, the residual symmetry of the z-aligned polar (P_z) phase contains all the elements of D_{4h} . In particular, the P_z phase can be expressed as $A_{\alpha i}^{P_z} = \hat{d}_\alpha a(x, y) \hat{z}_i$ with $a(x, y)$ real (time-reversal symmetry) and invariant under the sub-group C_{4v} : $a(x, y) = a(y, x) = a(-x, y) = a(x, -y)$. The P_z order parameter undergoes a sign change for any of the C_{2i} operations and reflection in the xy plane since $\hat{z} \rightarrow -\hat{z}$. Thus, combining these operations with the gauge transformation, $e^{i\pi}$, and C_{4v} yields the group, $D_{4h}^{L,\pi}$, which is isomorphic to D_{4h} . Thus, the residual symmetry group for the P_z phase is

$$(2.11) \quad H_{P_z} = SO(2)_{S_d} \times Z_2^{\text{spin}} \times D_{4h}^{L,\pi} \times T.$$

This state is the stable superfluid phase that onsets from the normal state at T_{c1} .

The P_z phase retains the sub-group C_{4v} of point symmetries, but is not the only ESP state with this symmetry. If we omit the operations that transform $z \rightarrow -z$, then we obtain two possible symmetry classes. If time-reversal is preserved we obtain the residual symmetry group is

$$(2.12) \quad H_{3D} = SO(2)_{S_d} \times Z_2^{\text{spin}} \times C_{4v}^L \times T$$

with an orbital order parameter field, $\vec{a} = a_x \hat{x} + a_y \hat{y} + a_z \hat{z}$, that includes three real components satisfying the reflection symmetries,

$$(2.13) \quad a_x(x, y) = -a_x(-x, y) = +a_x(x, -y)$$

$$(2.14) \quad a_y(x, y) = +a_y(-x, y) = -a_y(x, -y)$$

$$(2.15) \quad a_x(x, y) = a_y(y, x)$$

$$(2.16) \quad a_z(x, y) = a_z(y, x) = a_z(-x, y) = a_z(x, -y).$$

This phase is not found to be a local minimum of the GL functional for the weak-coupling values of the β parameters.

Another ESP phase with \mathcal{C}_{4v}^L symmetry is obtained if we break T symmetry, but preserve $\Pi_{xy} \cdot \mathbf{T}$. In this case the residual symmetry group is

$$(2.17) \quad \mathbf{H}_{\text{chiral-}\mathcal{C}_{4v}} = \text{SO}(2)_{\text{S}_d} \times \mathbf{Z}_2^{\text{spin}} \times \mathcal{C}_{4v}^L \times \{E, \Pi_{xy} \cdot \mathbf{T}\}.$$

The orbital vector, $\vec{a}_{\pm} = \vec{a}_{\perp} \pm i a_z \hat{z}$, with $\vec{a}_{\perp} = a_x \hat{x} + a_y \hat{y}$, is a complex vector field with real amplitudes $\{a_x, a_y, a_z\}$ satisfying the reflection symmetries in Eqs. 2.13-2.16 required by \mathcal{C}_{4v}^L . The \pm sign reflects the two-fold degeneracy resulting from broken time-reversal symmetry. These are *chiral* phases with a local chiral vector field given by

$$(2.18) \quad \vec{l}_{\pm} = \pm \vec{a}_{\perp} \times a_z \hat{z} = \pm a_z(\vec{R}) \left[a_y(\vec{R}) \hat{x} - a_x(\vec{R}) \hat{y} \right],$$

which is confined to the xy plane. For a unit cell centered on the post, the chiral vector vanishes on the post boundaries and at the center of the two channels, where $a_x = a_y = 0$, if the periodicity of the ordered phase is the same as that of the underlying geometry.

Here the phase is locally the P_z phase. For chiral phases, and more generally current carrying states, the periodicity of the ordered phase need not equal the underlying lattice periodicity. Thus, a complete classification of the residual symmetry sub-groups should include the space-group operations. This is beyond the scope of this report, but underscores the complexity of the possible phases of ${}^3\text{He}$ in a periodically confined geometry.

³ In the weak-coupling limit this chiral ESP phase is not energetically stable, but this phase, or a closely related phase with period $2L$, may emerge as a stable, or meta-stable, low temperature phase at high pressures due to strong coupling effects.⁴ However at high pressures, for very weak confinement, $L \gg 20\xi_0$, and small post dimensions, $d \lesssim \xi_0$, the chiral $-\mathcal{C}_{4v}^L$ phase is unlikely to be the equilibrium phase. In this limit we expect a chiral ABM-like phase with $\vec{l} \parallel \hat{z}$ in the center of the channels to be the equilibrium phase at temperatures below a narrow region of stability of the P_z phase.

The residual symmetries that define the bulk ABM phase, $A_{\alpha i}^{\text{ABM}} = d_{\alpha} (\hat{m} \pm i\hat{n})_i$, are (i) *chiral symmetry*, $Z_2^{\text{chiral}} = \{E, P_2 \cdot T\}$, where P_2 is reflection in a plane containing the chiral axis $\hat{l} = \hat{m} \times \hat{n}$, and (ii) *gauge-orbit symmetry*, $U(1)_{Lz-N}$, i.e. rotation by angle ϑ about the chiral axis, combined with a gauge transformation, $e^{\pm i\vartheta}$, by phase angle $\mp\vartheta$. A discrete analog of the ABM phase of bulk ${}^3\text{He}$ is obtained by breaking \mathcal{C}_{4v}^L rotational symmetry, but restoring symmetry with appropriate elements from $U(1)_N$. In addition, T symmetry is broken, but chiral symmetry is present as invariance with respect to the combined operation, $T \cdot \Pi_{zx}$. Thus, the discrete ABM phase is invariant with respect to

³In Chapter 3 we describe equilibrium phases which break the lattice translation symmetry.

⁴The in-plane chiral phase with period $2L$ is a periodic version of the texture obtained by Surovtsev and Fomin [88] for a uniform distribution of rod-like impurities embedded in ${}^3\text{He-A}$.

the group obtained from these generators,

$$(2.19) \quad \mathbf{C}_{4h}^{\text{L-N,T}} = \{E, e^{i\pi/2}C_4, e^{i\pi}C_4^2, e^{i3\pi/2}C_4^3, \\ \mathbf{T}\Pi_{zx}, e^{i\pi/2}\mathbf{T}\Pi_{zx'}, e^{i\pi}\mathbf{T}\Pi_{zy}, e^{i3\pi/2}\mathbf{T}\Pi_{zy'}\},$$

and is isomorphic to $\mathbf{C}_{4v}^{\text{L}}$. The full symmetry group is then

$$(2.20) \quad \mathbf{H}_{A_{\square}} = \text{SO}(2)_{\text{Sd}} \times \mathbf{Z}_2^{\text{spin}} \times \mathbf{C}_{4h}^{\text{L-N,T}},$$

and the functional form of the discrete ABM phase is $A_{\alpha i}^{\pm} = a(x, y) \hat{d}_{\alpha} (\hat{x} \pm i \hat{y})_i$, where $a(x, y)$ is real and obeys the $\mathbf{C}_{4v}^{\text{L}}$ reflection symmetries in Eq. 2.16. The A_{\square} -phase is not stable in the weak-coupling limit. However, several chiral phases are found to be stationary points of the GL functional for strong-coupling values of the β -parameters appropriate for high pressures. The phase diagram at high pressures will be discussed in a separate report.⁵

2.5. Numerical Methods

To compute the order parameter which minimizes the GL functional we implement a finite element method (FEM).[110] We discretize the ^3He unit cell with an unstructured triangular mesh generated with the code **Triangle**.[87] This type of mesh permits spatially varying triangular element sizes, which we use to provide finer spatial resolution in regions near boundaries and sharp corners as shown in the left panel of Fig. 2.1. Also, an unstructured mesh does not enforce any point symmetry that a periodic mesh possesses. Thus, the residual symmetries of the phases we find result from interaction terms in the

⁵See Chapter 3.

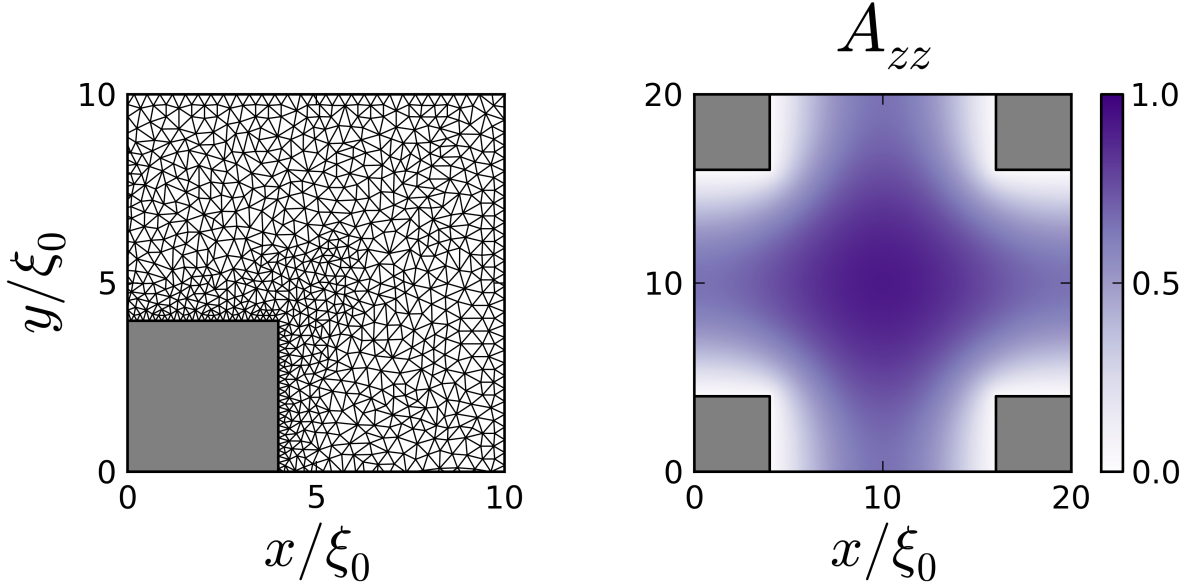


Figure 2.1. Left panel: One-fourth of the unit cell showing the triangular computational grid. The grey region defines the area occupied by the post. Right panel: Order parameter amplitude, $A_{zz}(\vec{R})$, of the z-aligned polar phase for $L = 20\xi_0$, $d = 8\xi_0$, $T = 0.9T_c$, and $\hat{d} = \hat{z}$. The order parameter is real and scaled in units of the bulk B-phase order parameter, $\Delta_B(T)$.

GL functional combined with pair-breaking and periodicity represented by the boundary conditions.

For the FEM we represent the order parameter with quadratic Lagrange interpolating functions defined on each element. The Lagrange interpolating functions are determined by the values of the order parameter at six nodes corresponding to the vertices and midpoints of edges of each element. The order parameter field defined at the nodes of each element is continuous across the entire domain. The resulting integration over the domain then separates into independent integrals over each element which we evaluate numerically with Gauss-Legendre quadrature.[1]

We minimize the discretized GL functional using an implementation of the conjugate gradient algorithm, `CG_DESCENT`.[\[40\]](#) The gradient, $\mathbf{G}[A] \equiv \delta\Omega/\delta A^\dagger(\vec{R})$, is evaluated at each node within the finite element scheme and input as the gradient in the conjugate gradient method. We set convergence as $\max\{|\mathbf{G}_i[A]|\} < 10^{-7}$, for all i degrees of freedom (i.e. all 9 complex components of A at each node) which we determined to yield no significant loss of accuracy compared to stricter tolerances.

2.6. Stable Phases - Maximal Pair-breaking

Figure 2.1 (right panel) shows the equilibrium order parameter for confined ${}^3\text{He}$ with period $L = 20\xi_0$ and post dimension $d = 8\xi_0$ at temperature $T = 0.9T_c$ for the case of maximal pair-breaking by the interior boundary. This is a spatially modulated z-aligned polar (P_z) state in which only the z-orbital component, A_{zz} , is non-vanishing. This phase breaks spin- and orbital rotation symmetry, but preserves time-reversal symmetry. Note that the polar amplitude is maximum in the center of the channel and decreases by approximately 50% into both x - and y channels. The P_z phase is an equal-spin pairing state and thus the more general representation for this phase is $A_{\alpha i} = \Delta(\vec{R}) \hat{d}_\alpha \hat{z}_i$, where \hat{d} is a real unit vector that defines the broken rotational symmetry in spin space. The P_z phase with only $A_{zz} \neq 0$ corresponds to $\hat{d} = \hat{z}$, and is degenerate with respect to the orientation of \hat{d} since we have neglected the nuclear dipole and Zeeman energies. The P_z phase belongs to the symmetry class of pairing states defined by the sub-group, $\mathbf{H}_{P_z} = \text{SO}(2)_{\text{Sd}} \times \mathbf{Z}_2^{\text{spin}} \times \mathbf{D}_{4\text{h}}^{\text{L},\pi} \times \mathbf{T}$, as discussed in Sec. 2.4

For the periods, $L \leq 30\xi_0$, and temperatures within the region of stability of the P_z phase, we find a finite polar amplitude everywhere within the ${}^3\text{He}$ cavity, except at

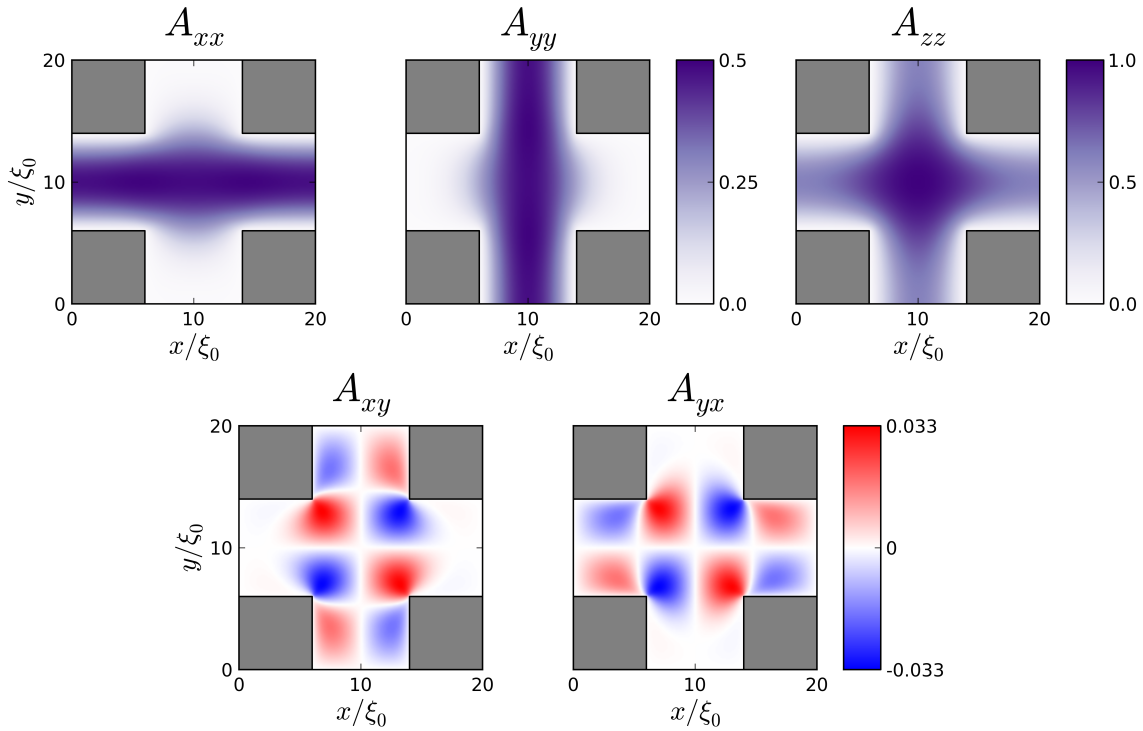


Figure 2.2. Order parameter components of the B_{\square} phase plotted in the domain V for $L = 20\xi_0$, $d = 12\xi_0$, and $T = 0.7T_c$. All values are real and scaled by the bulk B-phase order parameter $\Delta_B(T)$. Note the reduced scale of the A_{xy} amplitude.

the post boundaries. However for much larger periods, L , and the same channel width, $D = L - d$, the amplitude of the P_z order parameter appears to vanish deep within the x - and y channels far from the center, leaving a lattice of isolated islands of P_z condensate in the center. This suggests there may be a regime in which de-coupled P_z condensates nucleate in the center region, but are not phase coherent and do not exhibit superfluidity.

For the same period, post dimension and boundary conditions we also find a second stable phase in the weak-coupling regime at a lower temperature. This phase (B_{\square}) also preserves time-reversal symmetry, but has lower symmetry than that of the P_z phase. The B_{\square} phase is similar to the bulk B-phase in that the order parameter is real, with diagonal

elements, A_{xx} , A_{yy} and A_{zz} in the center of the channel as shown in Fig. 2.2. However, the component A_{xx} (A_{yy}) is strongly suppressed in the y -channel (x -channel), and off-diagonal components, A_{xy} and A_{yx} , appear at the corners of the posts. It is also clear from Fig. 2.2 that the components of the order parameter obey the reflection symmetries: $A_{xx}(x, y) = A_{yy}(y, x)$ and $A_{xy}(x, y) = A_{yx}(y, x)$, and that the diagonal components, A_{xx} , A_{yy} and A_{zz} are even functions of x and y , while the off-diagonal components, A_{xy} and A_{yx} , are odd under $x \rightarrow -x$ or $y \rightarrow -y$. The remaining off-diagonal components are all zero: $A_{zx} = A_{xz} = A_{zy} = A_{yz} = 0$. As discussed in Sec. 2.4 these are the conditions imposed by the discrete sub-group, $H_B = D_{4h}^{L+S} \times T$. This is the maximal allowed point symmetry and is the discrete analog of the maximal subgroup $SO(3)_{L+S}$ for the bulk B-phase. Indeed, we recover the bulk B-phase for $L \rightarrow \infty$ and $d \rightarrow 0$, as indicated in Fig. 2.3. Note that the off-diagonal components are significantly smaller in magnitude than the diagonal components and become negligible far from the post corners, except for $D \approx D_c(T)$, the critical line separating the P_z and B_\square phases.

The phase transition from the P_z to B_\square phase is presented in Fig. 2.3, which shows the maximal magnitudes for the components of the order parameter as a function of the confinement length D/ξ_0 for fixed period, L , and temperature, T . The transition is 2nd order, i.e. continuous as a function of D or T , with spontaneously broken symmetry from $H_{P_z} \rightarrow H_{B_\square}$. For confinement lengths onsetting at the critical value, $D_c(T) \rightarrow 4.1\xi_0$ at $T = 0$ and $L = 20\xi_0$, the x and y components, A_{xx} , A_{yy} , A_{xy} and A_{yx} , become finite, signaling the transition to the B_\square phase. Close to the transition the B_\square phase is locally a ‘‘planar’’ phase deep within the channels due to the suppression of the orbital components normal to the boundary. However in the central region the B_\square phase is defined by all

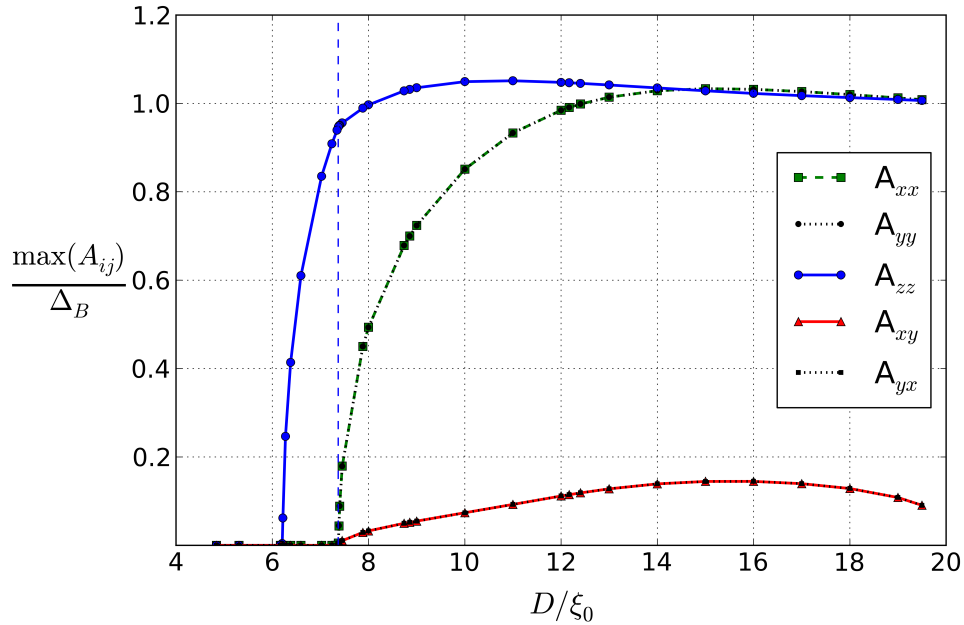


Figure 2.3. Order parameter amplitude as a function of the confinement length, D , for $L = 20\xi_0$ and $T = 0.7T_c$. The amplitudes are taken as the maxima within the domain. Note that maxima for A_{xx} and A_{yy} are equal, as are the maxima for A_{xy} and A_{yx} , but suppressed compared to A_{zz} . The dashed vertical line marks the 2nd order P_z to B_{\square} phase transition.

three diagonal components, as well as the off-diagonal components, A_{xy} and A_{yx} , allowed by D_{4h}^{L+S} symmetry.

2.7. Weak-Coupling Phase Diagram

The phase diagram for superfluid ^3He in the weak-coupling limit as a function of reduced temperature, T/T_c , and confinement length, D/ξ_0 , is shown in Fig. 2.4 for two values of the periodicity, $L = 5\xi_0$ (left panel) and $L = 20\xi_0$ (right panel). These two diagrams are qualitatively representative of the phase diagram for any $5 \leq L/\xi_0 \leq 30$. In particular, we do not find any additional equilibrium phases as minima of the GL functional with the weak-coupling material parameters.

The transition lines are found by classifying the phases based on non-negligible order parameter components, and then bracketing the location of both normal to P_z and the P_z to B_{\square} transitions. These brackets are refined until their width drops below a specified tolerance, which we chose to be $0.025\xi_0$. Note that predicted phase boundaries are limited by the restriction we place on the validity of the boundary condition for strong pair-breaking, i.e. $d \geq \xi_0/2$.

The phase boundary for the normal to P_z transition is determined by a linear eigenvalue equation, obtained by solving the linearized GL equation for the P_z order parameter, $\alpha(T) A_{zz} - K_1 (\nabla_x^2 + \nabla_y^2) A_{zz} = 0$, within the domain V , and with boundary condition, $A_{zz}|_{\partial V} = 0$, for maximal pair-breaking. The eigenfunction, $A_{zz} \equiv a_1(x, y)$, corresponding to the highest instability temperature, T_{c_1} , defines the spatial profile of the first unstable mode of the P_z phase. If we knew the exact functional form of the first unstable mode, $a_1(x, y)$, we could obtain the phase boundary, $T_{c_1}(D, L)$, from the equality in the Rayleigh-Ritz inequality,

$$(2.21) \quad \alpha(T_{c_1}) \geq \frac{- \int_V d\vec{R} \{ K_1 |\nabla a(x, y)|^2 \}}{\int_V d\vec{R} \{ |a(x, y)|^2 \}}.$$

In the absence of $a_1(x, y)$ we can obtain a lower bound on the N to P_z transition temperature with a good approximation to the eigenfunction $a_1(x, y)$. Consider the following

approximation to the most unstable mode,

$$\begin{aligned}
 a(x, y) = & \left[\frac{C(x) + C(y)}{1 + C(x)C(y)} \right] \Theta(D/2 - |x|)\Theta(D/2 - |y|) \\
 & + C(x)\Theta(D/2 - |x|) [\Theta(-D/2 - y) + \Theta(-D/2 + y)] \\
 (2.22) \quad & + C(y)\Theta(D/2 - |y|) [\Theta(-D/2 - x) + \Theta(-D/2 + x)] ,
 \end{aligned}$$

where $C(x) = \cos(\pi x/D)$, $\Theta(x)$ is the Heaviside step function, and x and y are defined on the domain $[-L/2, L/2]$. This function is piece-wise continuous at the interfaces between the central region and the x - and y channels, and satisfies the strong pair-breaking boundary condition, $a|_{\partial V} = 0$. The variational result $T_{c_1}^{var}$, is shown in comparison to the exact numerical result for the $N - P_z$ phase boundary, T_{c_1} in Fig. 2.4.

For the range of $L \leq 30\xi_0$ that we consider, and for all $D \geq D_c(T)$ that gives a superfluid transition, the P_z phase is stable for a temperature range below T_{c_1} . Furthermore, for a given L there is a narrow range of confinement lengths, D , in which only the P_z phase is stable. This is in sharp contrast to one-dimensional confinement in an infinite slab where the axial or planar phases are stable under strong confinement. The absence of these phases in the periodic confined geometry here is due to pair-breaking within the two orthogonal x and y channels, the large cost in gradient energy for x - and y orbital components for strong confinement and the weak-coupling β -parameters. Chiral phases, such as the A_{\square} -phase and the chiral- C_{4v} phase will be discussed in a separate report on GL theory of confined phases in the strong-coupling limit.

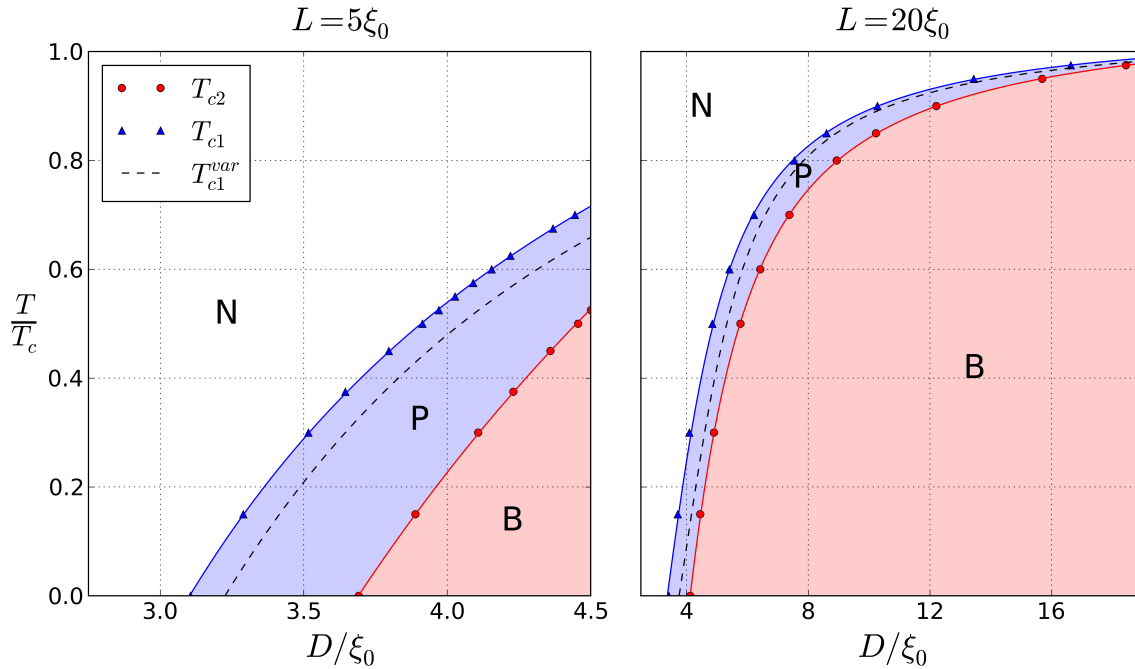


Figure 2.4. Phase diagrams for $L = 5\xi_0$ and $L = 20\xi_0$. The dashed curve is the normal to P_z transition obtained by the variational method. The solid curves are fits of the transition data points to the functional form of the variational curve. Note that there is a range of confinement lengths, D , for which only the P_z phase is realized.

2.8. Conclusions

We have investigated the inhomogeneous phases of superfluid ^3He confined to a two-dimensional lattice of square, sub-micron-scale boundaries (“posts”) with translational invariance in the third dimension. In the weak-coupling limit, and strong pair-breaking by the boundary post, we find an instability from the normal state, at $T_{c1} < T_c$ for bulk superfluid ^3He , to an equal-spin pairing state with z -aligned polar orbital order. For fixed lattice spacing, L , there is a critical post dimension, d_c , above which only the periodic polar phase is stable. For $d < d_c$ we find a second, low-temperature phase onset at $T_{c2} < T_{c1}$ from the polar phase to a periodic “B-like” phase. The low temperature phase

is inhomogeneous, anisotropic and preserves time-reversal symmetry, but unlike the bulk B-phase has only D_{4h}^{L+S} point symmetry. This or similar geometries may be realizable with current nano-fabrication processes, and could therefore provide a potential avenue for experimental studies of the polar phase in ^3He in well defined geometries.[108] Further studies of ^3He in geometries with periodic confinement are expected to yield a large number of tunable phases with unique broken symmetries and topological properties that are not realized in bulk superfluid ^3He .

Acknowledgements — This research is supported by the National Science Foundation (Grant DMR-1106315). We thank David Ferguson for many discussions and critique during the course of this work.

CHAPTER 3

Strong-coupling GL theory of ^3He in a periodic confined geometry**3.1. Strong-coupling Corrections**

One of the main weaknesses of weak-coupling Ginzburg-Landau theory is revealed by considering the pressure dependence, or lack thereof, of the free energy functional. The condensation energy density for a bulk homogeneous phase is given by

$$(3.1) \quad f_* = \frac{-\alpha(T)^2}{4\beta_*},$$

where β_* represents the characteristic sum of β_i s for a given stationary phase. The ratio of condensation energies for any two phases is therefore pressure independent, which means that the B phase is the sole stable phase even at high pressures. Furthermore, that ratio is also temperature independent, so that even if there were some pressure where the A phase became stable, there would still be no transition as a function of temperature between the homogeneous A and B phases. These two results obviously contradict the experimental superfluid ^3He phase diagram and must be considered when interpreting weak-coupling phase diagrams.

The weak-coupling material parameters are derived from the leading-order contribution to the full GL free-energy in an expansion in the small parameter T/T_F , in which $\Delta\Omega^{\text{wc}} \sim (T_c/T_F)^2 E_N$ and E_N is the ground state energy of the normal Fermi liquid. The next-to-leading-order corrections to the weak-coupling GL functional enter as corrections

to the weak-coupling material coefficients. These are of order $\Delta\beta_i^{\text{sc}} \approx \beta_i^{\text{wc}}(T/T_F)\langle w_i|A|^2 \rangle$, where $\langle w_i|A|^2 \rangle$ is a weighted average of the square of the scattering amplitude for binary collisions between quasiparticles on the Fermi surface.[72] At high pressures, these scattering amplitudes largely compensate the small parameter T/T_F , resulting in significant strong-coupling corrections.

Although we later calculated the $\Delta\beta_i^{\text{sc}}$ s through a model of the quasiparticle scattering amplitude, detailed in Chapter 8, for this work we used the most current values available, inferred from experiment by Choi et al.[23] These experimentally determined beta parameters by design fit the heat capacity jumps for the A and B transitions, which should make them reasonably accurate when considering the energetics of A and B-like phases at T_c . The A phase correctly appears as a stable phase above the polycritical point $p_{PCP} = 21.22$ bar; however, in the standard formulation of fourth-order GL theory it is the only stable phase at all temperatures above that point.

The presence of a tricritical points at p_{PCP} tells us that we may break the degeneracy between the A and B free energies around that point by retaining the leading-order temperature dependence of the $\Delta\beta_i^{\text{sc}}$ s which determine the tricritical point. Near T_c , the leading strong-coupling corrections scale as $\Delta\beta_i^{\text{sc}} \sim (T/T_F)|\beta_1^{\text{wc}}|$, where the linear scaling with T originates from the phase space for binary collisions of quasiparticles at low temperatures. This is applied to the experimental β_i s by first subtracting off the weak-coupling contribution and then scaling the remaining strong-coupling piece as

$$\begin{aligned} \Delta\beta_i^{\text{sc}} &= \beta_i^{\text{sc}} - \beta_i^{\text{wc}}, \\ (3.2) \quad \beta_i(p, T) &= \beta_i^{\text{wc}} + \frac{T}{T_c}\Delta\beta_i^{\text{sc}}(p). \end{aligned}$$

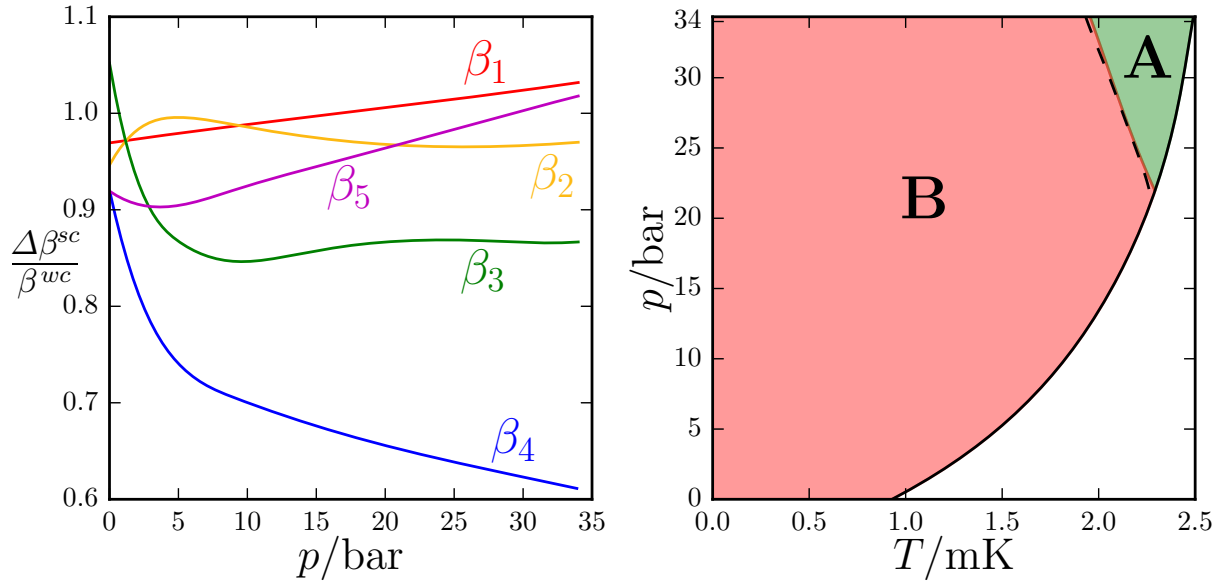


Figure 3.1. (Left) Experimental strong-coupling $\Delta\beta^{sc}$ s estimated by Choi et al[23] and plotted relative to their weak-coupling values. (Right) The bulk phase diagram showing the regions of stability of the A (green) and B (red) phases using the experimental β s with linear T scaling. The dashed line is the experimental A-B transition line terminating at the experimental PCP point.

When we extrapolate this linear T dependence for all temperatures and pressures, we find that the resulting Ginzburg-Landau bulk phase diagram largely reproduces the experimental T_{AB} line as shown in Fig. 3.1. This modification greatly enhances the region in which GL theory is useful.

3.1.1. Boundary Conditions

When dealing with confined geometries, appropriate boundary conditions are essential. For planar surfaces there are two well-defined boundary conditions within Ginzburg-Landau theory: maximal pairbreaking, representing quasiparticle retroreflection, and minimal pairbreaking, representing quasiparticle specular reflection.[5] If we take the surface to lie along the $x - y$ plane with ^3He occupying $z > 0$, then maximal pairbreaking is the condition

$$(3.3) \quad A_{\alpha i} \Big|_{z=0} = 0 \quad \forall i \in \{x, y, z\},$$

while minimal pairbreaking corresponds to the boundary conditions

$$(3.4) \quad \begin{aligned} A_{\alpha z} \Big|_{z=0} &= 0, \\ \nabla_z A_{\alpha x} \Big|_{z=0} &= \nabla_z A_{\alpha y} \Big|_{z=0} = 0. \end{aligned}$$

In many cases it would be useful to go beyond these boundary conditions which represent the two extremes of surface Cooper pair suppression. Some geometries may be highly sensitive to surface conditions, and interesting physics could be hidden between these two limits. Additional control over the boundary conditions would also provide a test of whether a geometry might be sensitive to small variations in experimental surface conditions. Ambegaokar, de Gennes, and Rainer[5] introduced the idea of a transverse extrapolation length b_T to describe the effect of an atomically rough surface on the order parameter, where the order parameter components with relative momenta normal to the surface were calculated to decrease to zero linearly past the boundary at a distance

$b_T \approx 0.54\xi_0$ for such a surface with diffuse scattering. This idea can be turned into a more general boundary condition in GL theory as

$$(3.5) \quad \begin{aligned} A_{\alpha z}|_{z=0} &= 0, \\ \nabla_z A_{\alpha x}|_{z=0} &= \frac{1}{b_T} A_{\alpha x}|_{z=0}, \\ \nabla_z A_{\alpha y}|_{z=0} &= \frac{1}{b_T} A_{\alpha y}|_{z=0}, \end{aligned}$$

where $b_T = b'_T \xi_0$ can be treated as a parameter that varies between the maximal pair-breaking ($b'_T = 0$) and minimal pairbreaking ($b'_T = \infty$) limits. This ‘‘AdGR’’ boundary condition is thus a useful extension of the typical Ginzburg-Landau boundary conditions.

3.2. Strong-coupling phase diagram

3.2.1. Stable phases

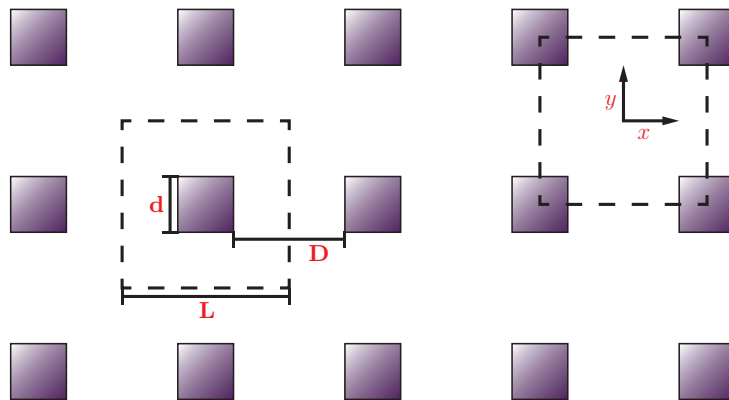


Figure 3.2. (Left) Diagram for the array of posts showing its relevant dimensions: the post size d , the confinement length D , and the post spacing L . (Right) For purposes of plotting the superfluid order parameter, we shift the origin of the unit cell.

We return to the periodic geometry discussed in Chapter 2 and diagrammed in Fig. 3.2[103]. While previously we only considered the equilibrium P_z and s_B phases in weak-coupling, now we consider a broader range of possible phases, including A-like phases with chiral symmetry. To minimize the free-energy functional we switch to a simpler set of algorithms for this system and the remaining Ginzburg-Landau work in this thesis. Spatial discretization is done using a simple finite difference scheme on a regular rectangular lattice. We use a Quasi-Newton method, Limited-memory BFGS, as our numerical solver. The details of L-BFGS are given in Appendix B.

In particular, the A_{C_2} phase is an ESP phase which can be locally identified with the polar distorted bulk A phase. Like the A phase it breaks time-reversal symmetry and has a local chiral axis \hat{l} which will spatially average to point along one of the four [110] directions. It has the residual symmetry group

$$(3.6) \quad H = \text{SO}(2)_{S_d} \times Z_2^{\text{spin}} \times D_{2h}^{\text{L,T},\pi},$$

where $D_{2h}^{\text{L,T},\pi}$ consists of combined orbital, gauge, and time reversal operations. The A_{C_2} order parameter is plotted in Fig. 3.3 along with its chiral axis. This phase is closely related to a phase found in quasi-1D cylindrical pores described in Chapter 5.

Additional stable phases are possible through the formation of energetically favorable domain walls which spontaneously break the lattice translation symmetry, and we describe two which we know to be stable. These s_A and s_B phases consist of domains of the A_{C_2} and s_B phases, respectively, separated by domain walls. The mechanism that stabilizes these domain walls is the same that stabilizes the “stripe” phase[99] of superfluid ^3He confined in slabs discussed in Chapter 7. Both domain wall phases have the same organization,

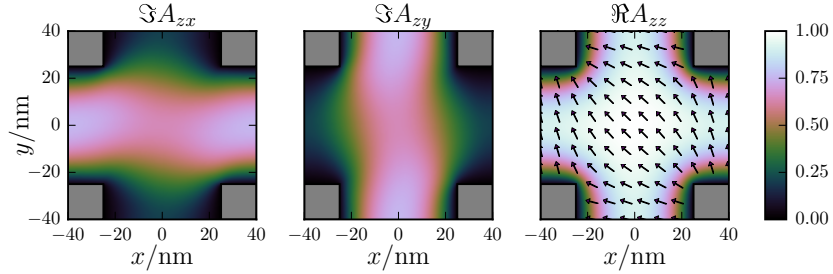


Figure 3.3. The AC_2 order parameter for $T = 0$, $P = 30$ bar, $L = 80$ nm, and $D = 50$ nm in units of the bulk amplitude $\Delta_A^2 = -\alpha(T)/(4\beta_{245})$. The \hat{l} vector is overlaid on the plot for the polar amplitude $\Re A_{zz}$

shown in Fig. 3.4, and these phases may be calculated with a periodic unit cell of size $2L \times 2L$.

Both of these translational symmetry breaking phases have unique experimental signatures. Unlike the AC_2 phase, in the s_A phase the \hat{l} vector spatially averages to zero over a single unit cell. This means that its NMR signatures will be similar to that of the Polar phase, and not the AC_2 phase. In the s_B phase, the spatial averages of $A_{xx}A_{yy}$, $A_{xx}A_{zz}$, and $A_{yy}A_{zz}$ will likewise be zero, greatly modifying the tipping angle dependence of its NMR frequency shifts relative to the s_B phase.

3.2.2. Phase Diagram

Figure 3.5 shows the regions of stability of all five superfluid phases. The P_z phase occurs at the highest temperatures due to its Cooper pair relative momentum being solely along the unconfined direction. All transitions involving the P_z phase are second order. All phase transitions not involving the P_z or normal phase are first order, including the s_A and s_B phases. The energetic advantage of the domain walls is highly dependent on the relative values of L and D , and the energy separating s_A from AC_2 and s_B from s_B is

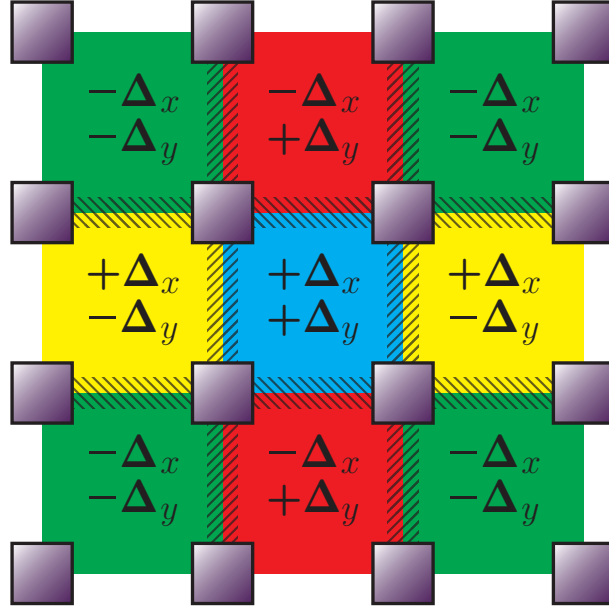


Figure 3.4. The domain structure for both the $s_{\mathbf{A}}$ and $s_{\mathbf{B}}$ phases. For $s_{\mathbf{A}}$, $\Delta_x = \Im A_{zx}$ and $\Delta_y = \Im A_{zy}$, while for $s_{\mathbf{B}}$, $\Delta_x = \Re A_{xx}$ and $\Delta_y = \Re A_{yy}$. The domain walls are analogous those of the stripe B phase in the slab geometry.

very small. Despite this, the tetracritical point separating those four phases is resolved consistently for the dimensions of Fig. 3.5. These results suggest that ordered periodic confining geometries could provide an extreme wealth of different superfluid phases.

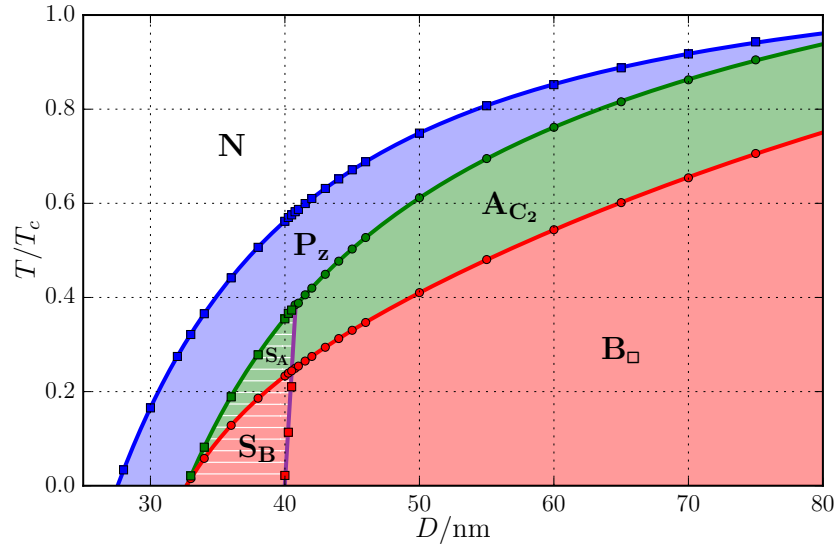


Figure 3.5. Phase diagram for the periodic geometry as a function of T and D with $P = 30$ bar, $L = 80$ nm, and maximal pairbreaking boundary conditions. These values of P and L were chosen to cleanly separate the five superfluid phases.

CHAPTER 4

Line impurities and Nafen aerogels**4.1. Introduction**

While the periodic post geometries may in principle be fabricated, there are similar systems that are already being studied with ^3He . Silica aerogels have porosities reaching above 98%, can be produced with high homogeneity, and provide confinement on the order of the superfluid coherence length ξ_0 . [28, 70] Silica aerogels can be made globally anisotropic through mechanical compression or chemical processing with uniaxial strains up to $\pm 30\%$. [71]

Another class of high porosity random solids are materials composed of amorphous aluminum oxide or aluminum hydroxide. [11] These “nematic” aerogels, which are extremely anisotropic, consist of slender strands aligned along a common axis, with characteristic diameters of ≈ 9 nm and interstrand spacing on the order of ξ_0 . [10] While several different varieties of these nematic aerogels have been studied, the best studied are the “nafen” aerogels, which lead to the first experimental observations of the polar phase in superfluid ^3He and the discovery of half-quantum vortices stabilized in the polar phase under rotation. [29, 12]

The array of strands, aligned on average along the z direction, can be reasonably mapped onto the model of a periodic array of posts. However, their small ≈ 9 nm diameter makes them too small relative to ξ_0 to be treated as macroscopic objects with boundary

conditions in the GL theory. To explicitly study these nematic aerogels, we replace the finite-diameter posts with line impurities described by an anisotropic scattering cross-section.[73]

4.2. Ginzburg-Landau Theory

The same strong-coupling Ginzburg-Landau theory developed in Chapter 3 is employed here, with the posts and their boundary conditions being replaced with a new impurity term in the free-energy functional.

Pair-breaking due to the line impurities is incorporated into the GL theory by extending the microscopic calculation of the correction to the free energy for isotropic impurities to line impurities.[90] In the GL regime the impurity contribution to the free energy density for line impurities with density $n_{\text{imp}}(\mathbf{r})$ is

$$(4.1) \quad f_{\text{imp}} = n_{\text{imp}}(\mathbf{r}) \frac{k_f^2}{48\pi k_B T_c} \text{Tr} (A \underline{\varpi} A^\dagger) ,$$

where ϖ is a second-rank tensor defined by the transport cross-section for a line impurity,

$$(4.2) \quad \varpi_{ij} = 3 \langle |\hat{\mathbf{n}} \times \hat{\mathbf{k}}| \mathbf{k}_i \left[\varpi(\hat{\mathbf{k}}) \hat{\mathbf{k}}_j - 4\pi \langle \frac{d\varpi}{d\Omega'}(\hat{\mathbf{k}}, \hat{\mathbf{k}}') \hat{\mathbf{k}}'_j | \hat{\mathbf{n}} \times \hat{\mathbf{k}}' | \rangle_{\hat{\mathbf{k}}'} \right] \rangle_{\hat{\mathbf{k}}} ,$$

where $d\varpi/d\Omega$ is the differential scattering cross-section, $\hat{\mathbf{n}}$ the nematic axis of the line impurity and $\varpi(\hat{\mathbf{k}}) = 4\pi \langle (d\varpi/d\Omega')(\hat{\mathbf{k}}, \hat{\mathbf{k}}') | \hat{\mathbf{n}} \times \hat{\mathbf{k}}' | \rangle_{\hat{\mathbf{k}}'}$ is the total scattering cross-section. In particular, for a line impurity with only isotropic in-plane scattering $\frac{d\varpi}{d\Omega}(\hat{\mathbf{k}}, \hat{\mathbf{k}}') = \omega_0/\pi^2$, which gives $\varpi(\hat{\mathbf{k}}) = \omega_0$ and $\varpi_{ij} = \frac{9\pi}{32}\omega_0(\delta_{ij} - \frac{1}{3}\hat{\mathbf{n}}_i\hat{\mathbf{n}}_j)$. For line impurities with larger radii

we may parametrize the tensor as

$$(4.3) \quad \varpi = \begin{pmatrix} \omega_{\perp} & 0 & 0 \\ 0 & \omega_{\perp} & 0 \\ 0 & 0 & \omega_{\parallel} \end{pmatrix},$$

where ω_{\parallel} corresponds to scattering principally along $p_z = \mathbf{p} \cdot \mathbf{n}$ and ω_{\perp} to scattering principally in the $p_x - p_y$ plane.[78]

4.3. Impurity Lattice

The simplest model of nafen is a periodic square lattice of line impurities with lattice spacing, L , determined by the mean distance between nafen strands. The resulting GL functional reduces to that for ${}^3\text{He}$ confined within a unit cell with a single line impurity at the origin. The impurity contribution to the free energy density of ${}^3\text{He}$ in the primitive unit cell is then

$$(4.4) \quad f_{\text{imp}} = \frac{k_f^2}{48\pi k_B T_c} \sum_{\alpha} \{ \omega_{\parallel} |A_{\alpha z}(0, 0)|^2 + \omega_{\perp} (|A_{\alpha x}(0, 0)|^2 + |A_{\alpha y}(0, 0)|^2) \}.$$

The values of ω_{\parallel} and ω_{\perp} depend on the quasiparticle-impurity potential and the quasiparticle density of states at the Fermi energy.[78] We fit them based on the observed phase transitions.

	ρ (g/cm ³)	r (nm)	L (nm)	ω_{\perp} (nm)	ω_{\parallel} (nm)
nafen-72	72	4.0	52.8	4.25	0.704
nafen-90	90	4.0	47.8	4.25	1.073
nafen-243	243	4.5	32.3	4.25	0.667

Table 4.1. Experimental parameters for the nafen aerogels with corresponding model parameters. The density, ρ , and the mean strand radius, r , are from Asadchikov et al.[10]

The Normal-Polar transition, T_{c_0} , can be accurately determined from linear instability analysis with a uniform order parameter as

$$(4.5) \quad \frac{T_{c_0}}{T_c} = 1 - \frac{\pi^2 \xi_0(p) \omega_{\parallel}}{4 L^2},$$

where T_c is the transition temperature for pure bulk ³He. Table 4.1 shows the experimental and fit values of ω_{\parallel} corresponding to three different nafen samples measured by Dmitriev et al.[29]

The in-plane cross-section, ω_{\perp} , is more difficult to fix, as it is a transition between two inhomogeneous phases. For nafen-72 and nafen-90, we choose $\omega_{\perp} = 4.25$ nm on the basis of its agreement with experiment across most pressures. This is not possible with nafen-243, since no phases were observed experimentally beyond the Polar phase. For this reason, we use the same value of $\omega_{\perp} = 4.25$ nm as a point of comparison. These model parameters as well as the relevant experimental measurements are summarized in Table 4.1. Figure 4.1 shows the spatial dependence of the polar phase order parameter in the square lattice for both nafen-90 and nafen-243. As T approaches T_{c_0} from below, the order parameter becomes increasingly uniform.

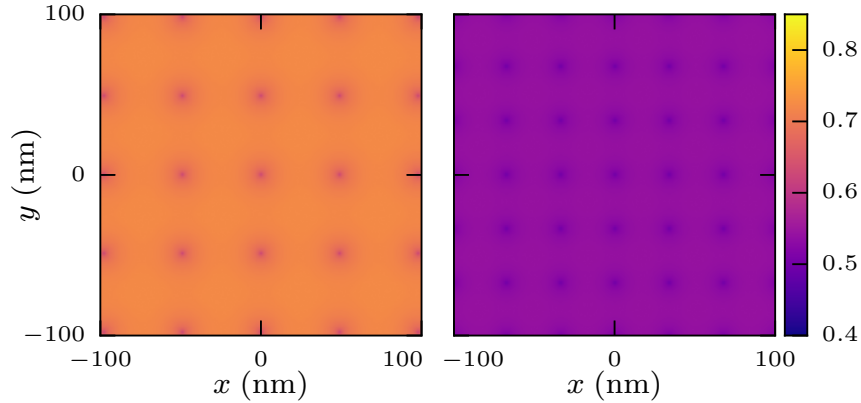


Figure 4.1. Polar order parameter at $p = 15$ bar and $T = 0.95T_c$ for the square lattice models of both nafen-90, left, and nafen-243, right, in units of $\Delta_P = \sqrt{|\alpha|/2\beta_{12345}}$.

4.4. Phase Diagram

The calculated phase diagrams for all three Nafen samples are shown in Figure 4.2. The Normal-Polar phase transition is in excellent with experiment across all samples and pressures. Similarly, the calculated Polar-A transition matches the Polar-A transition reported by Dmitriev et al in both nafen-72 and nafen-90[29]; in nafen-243, this transition was not seen by Dmitriev et al. Few experimental data points are available for the B-A transition on warming, and only in Nafen-90; however, the calculated transition curve is still largely consistent with the available points at moderate pressure reported by Dmitriev et al.[29]

4.5. Disorder in the Lattice

The strands that make up the nafen aerogels do not form a perfect lattice, and this is expected to lead to inhomogeneities in the sample with varying degrees of confinement and in-plane anisotropy. We can model this disorder by considering larger “supercells”

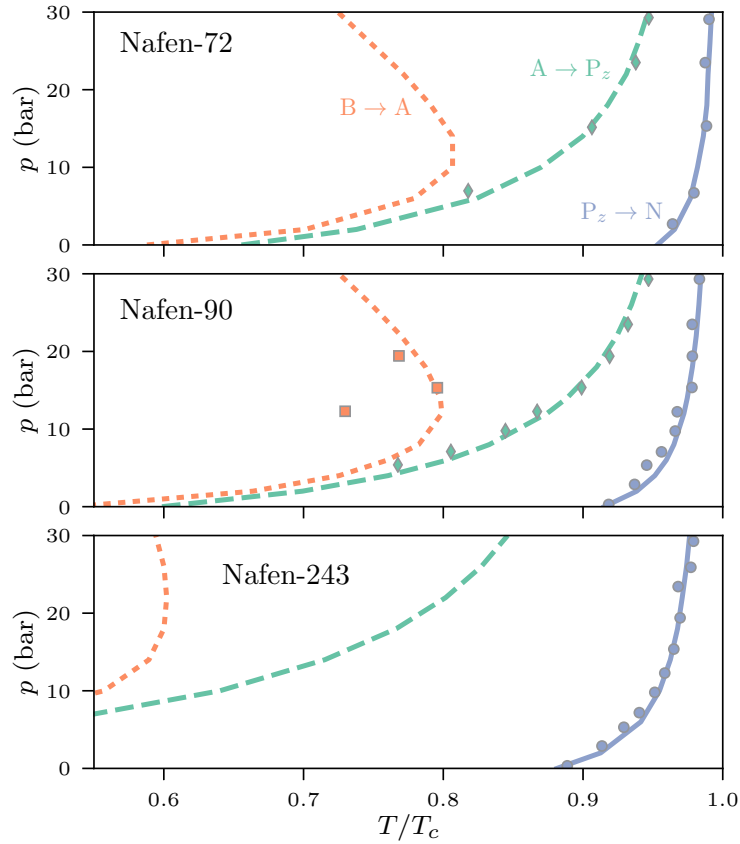


Figure 4.2. Phase diagrams for nafen-72, nafen-90, and nafen-243, with points denoting the phase transitions observed by Dmitriev et al. The lines show the calculated transitions on the square lattice using the parameters in Table 4.1.

containing many impurity sites. To generate relatively large spatial inhomogeneities, we fix the porosity of the supercell and place the impurities in space selected from a uniform probability distribution. An example of such a supercell is shown in Fig. 4.3, which illustrates how the suppression of the order parameter varies together with the local impurity density.

The dashed lines in Figure 4.4 are the phase transitions calculated for the supercell in Fig. 4.3, using the same values for ω_{\parallel} and ω_{\perp} as with the regular nafen-90 lattice.

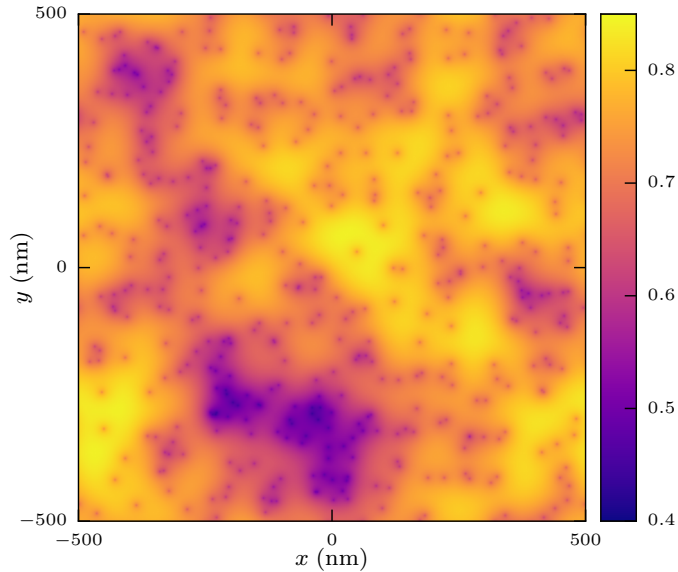


Figure 4.3. Polar order parameter at $p = 15$ bar and $T = 0.95T_c$ for the disordered supercell model of Nafen-90 in units of $\Delta_P = \sqrt{|\alpha|/2\beta_{12345}}$.

Although the inhomogeneous regions do shift the transition temperatures higher towards T_c , the magnitude of the shift is small and the pressure dependence of the transitions remains largely the same. This would suggest that the square lattice model is adequate to predict phase transitions in the nafen aerogels even in the presence of strong in-plane disorder. However, upon checking the predicted NMR frequency for both disordered and periodic models, we found substantial discrepancies with experiment.

4.6. NMR and further models

The experiments by Dmitriev et al [29] to determine the phase diagram of superfluid ^3He in nafen aerogels were done using NMR frequency shifts to detect the spin and orbital correlations of the superfluid phases. These shifts are calculated theoretically from the inhomogeneous solutions of the order parameter obtained from GL theory based on the theory of the NMR frequency shifts described in Chapter 5. The GL frequency shifts

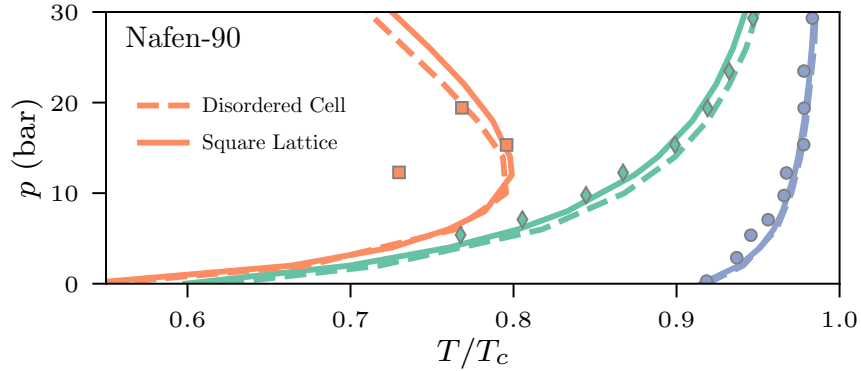


Figure 4.4. Nafen-90 phase diagram comparing the square lattice (solid lines) to the disordered cell (dashed lines) of Fig. 4.3.

shown in Figure 4.5 for both the periodic lattice and disordered supercell model of nafen are very similar to each other and significantly larger than that found in experiment.

A possible reason for the discrepancy would be the presence of substantial correlated disorder. To generate a more correlated disorder in the supercell we start as before by first fixing the number of impurities based on the nafen porosity. A relatively small initial number of nucleation sites are randomly placed. Starting from each nucleation site, additional sites are chosen by taking steps sampled from a Lévy distribution with median corresponding to the average interstrand spacing and placing an impurity at each step. Figure 4.6 shows a representative of the modified Lévy distribution. For the NMR calculations, the value of ω_{\parallel} was tuned to match the apparent experimental T_c while the value of ω_{\perp} was tuned to roughly match the initial NMR slope. This new model produced remarkably better agreement with the experimental NMR data.

One thing lost with the modified Lévy model is a well-defined Polar-A transition. Figure 4.7 shows the relatively broad temperature range in which the supercell contains

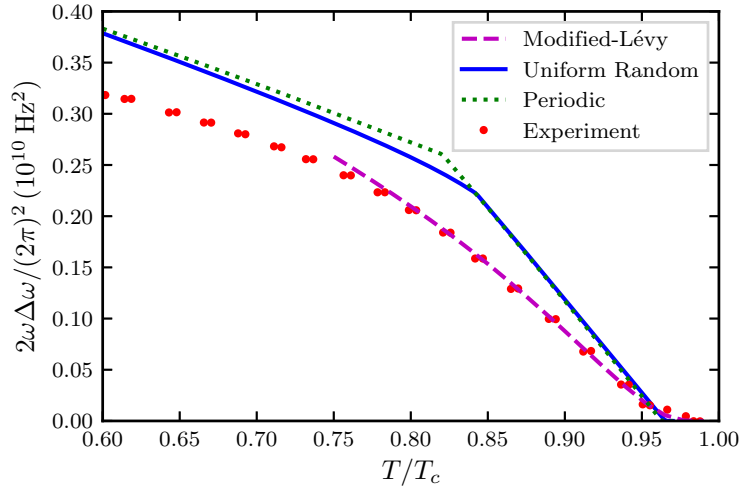


Figure 4.5. Calculated NMR frequency shifts for three different models of nafen-90 impurities compared to the experimental measurements by Dmitriev et al.[29] The “modified-Lévy” curve model is described in the text.

both polar distorted A phase regions alongside regions of pure polar phase. The two-phase mixture is due to large fluctuations in the impurity density, with rarefied regions favoring the chiral phase interspersed with denser regions of polar phase. At this time it is not clear if nafen aerogels exhibit the large fluctuations in local density suggested by the modified Lévy distribution.

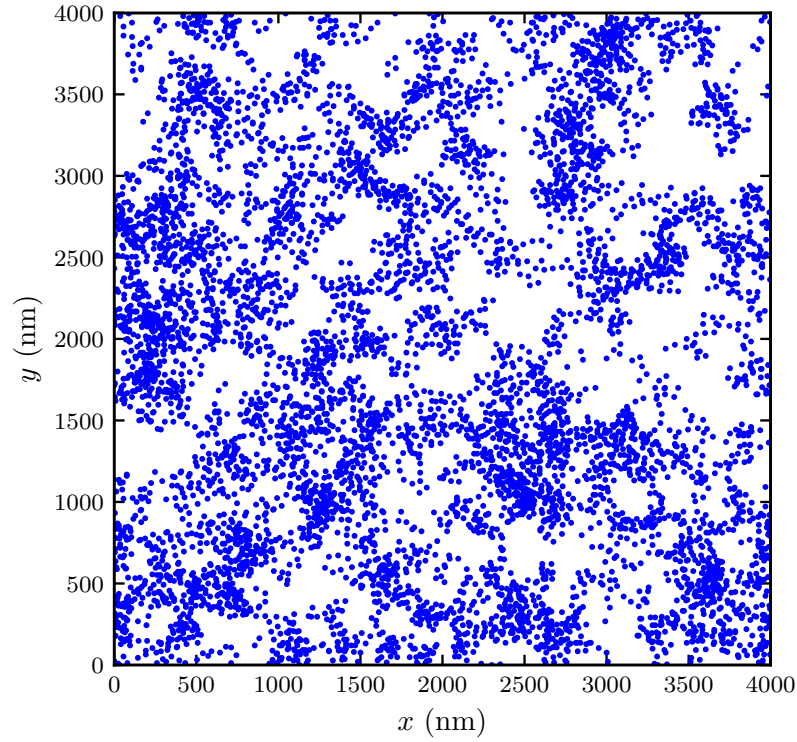


Figure 4.6. Impurity distribution for the “modified Lévy” model used in Fig. 4.5

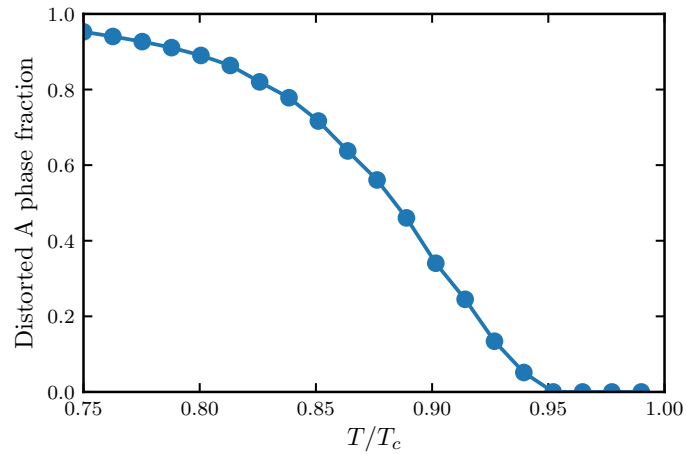


Figure 4.7. Volume fraction of the polar distorted A phase in the “modified Lévy” supercell as a function of temperature.

CHAPTER 5

Publication: Superfluid phases of ^3He in nanoscale channels**5.1. Abstract**

Confinement of superfluid ^3He on length scales comparable to the radial size of the p-wave Cooper pairs can greatly alter the phase diagram by stabilizing broken symmetry phases not observed in bulk ^3He . We consider superfluid ^3He confined within long cylindrical channels of radius 100 nm, and report new theoretical predictions for the equilibrium superfluid phases under strong confinement. The results are based on the strong-coupling formulation of Ginzburg-Landau theory with precise numerical minimization of the free energy functional to identify the equilibrium phases and their regions of stability. We introduce an extension of the standard GL strong-coupling theory that accurately accounts for the phase diagram at high pressures, including the tri-critical point and $T_{AB}(p)$ line defining the region of stability for the bulk A-phase. We also introduce tuneable boundary conditions that allow us to explore boundary scattering ranging from maximal to minimal pairbreaking, and report results for the phase diagram as a function of pressure, temperature, and boundary conditions. Four stable phases are found: a polar phase stable in the vicinity of T_c , a strongly anisotropic, cylindrical analog of the bulk B phase stable at sufficiently low temperatures, and two chiral A-like phases with distinctly different orbital symmetry, one of which spontaneously breaks rotation symmetry about the axis of the cylindrical channel. The relative stability of these phases depends sensitively on

pressure and the degree of pairbreaking by boundary scattering. The broken symmetries exhibited by these phases give rise to distinct signatures in transverse NMR resonance spectroscopy. We present theoretical results for the transverse NMR frequency shifts as functions of temperature, the *rf* pulse tipping angle and the static NMR field orientation.

5.2. Introduction

Superfluid ^3He is a spin-triplet, p-wave Fermi superfluid, where not only is symmetry spontaneously broken but also spin and orbital rotation symmetries $\text{SO}(3)_S \times \text{SO}(3)_L$. There are a myriad of ways to break these symmetries, leading to many potential superfluid phases. In bulk ^3He , in the absence of a magnetic field, only two stable phases are observed: the A phase and the B phase. However, other phases may be stabilized by introducing symmetry breaking terms, such as a magnetic field, impurities, or boundaries, which couple to the spin and orbital degrees of freedom of the Cooper pairs. In particular, confining surfaces suppress Cooper pairs with relative momentum normal to the surface, which leads to a long-range orienting effect on the orbital order parameter.[5] When confined within distances comparable to the Cooper pair coherence length, $\xi_0 \approx 160 - 770 \text{ \AA}$ depending on pressure, the influence of the confining surfaces can stabilize phases much different than those of bulk superfluid ^3He .

Advances in nanoscale fabrication techniques,[50] as well as the production of porous materials with interesting structure on the coherence length scale,[71, 11] have made studies of the effects of strong confinement on broken symmetry phases of topological quantum materials feasible, and have brought a surge of research on the effects of confinement on superfluid ^3He . [25, 66, 59, 58, 106] One of the simplest confining geometries is the pore, a long, small radius cylinder. The pore has long been of theoretical interest due

to the number of different A-phase textures that might be stabilized,[54] as well the effects of radial confinement on the superfluid phase diagram.[32, 89, 53] Nuclear magnetic resonance (NMR) experiments in 2 μm diameter pores have observed A-like textures,[37, 83] but have had difficulty definitively identifying the textures present.[19] New fabrication techniques for porous membranes[55] have made available pores with diameters below 1 μm , which, coupled with an array of new experimental techniques,[35, 109, 50, 75] open new windows into superfluid ^3He under strong confinement.

In this paper we consider an infinitely long cylindrical pore of radius $R = 100$ nm, and we study the equilibrium phases in Ginzburg-Landau (GL) theory and identify their signatures in nonlinear NMR spectroscopy. By incorporating pressure dependent strong-coupling corrections to the GL material coefficients, and a tuneable pairbreaking boundary condition, we obtain phase diagrams as functions of temperature, pressure, and surface condition. Finally, we derive expressions for the transverse NMR frequency shifts of the equilibrium phases of ^3He confined in the pore as functions of *rf* pulse driven tipping angle, and show how they vary with order parameter symmetry and orientation of the static magnetic field.

5.3. Ginzburg-Landau Theory

We use Ginzburg-Landau theory calculations of the superfluid ^3He order parameter and free energy to determine the stable phases present in the pore. The order parameter for superfluid ^3He , given by the manifold of spin-triplet, p-wave BCS pairing states, may be represented by the 2×2 gap matrix,

$$(5.1) \quad \hat{\Delta}(\hat{p}) = \sum_{\alpha i} A_{\alpha i} (i\sigma_{\alpha}\sigma_y) \hat{p}_i,$$

which depends on the direction of the relative momentum \hat{p} of the Cooper pairs, and is parameterized by the 3×3 complex matrix order parameter A . The matrix A transforms as a vector under spin rotations, and separately as a vector under orbital rotations. In cylindrical coordinates $A_{\alpha i}$ can be represented as

$$(5.2) \quad A = \begin{pmatrix} A_{rr} & A_{r\phi} & A_{rz} \\ A_{\phi r} & A_{\phi\phi} & A_{\phi z} \\ A_{zr} & A_{z\phi} & A_{zz} \end{pmatrix},$$

where we have chosen aligned spin and orbital coordinate axes.

The presence of boundaries reduces the possible residual orbital symmetries of the superfluid phases to be elements of the point group of the confining cylindrical geometry. However, this reduction in symmetry is due to interactions atomically close to the boundary surface; away from the surface, the ^3He particle-particle interactions are still invariant under the maximal symmetry group of bulk ^3He . Thus, the Ginzburg-Landau free energy functional is given by the invariants of the bulk ^3He symmetry group,

$$(5.3) \quad \mathbf{G}_{\text{bulk}} = \mathbf{U}(1) \times \mathbf{SO}(3)_{\text{S}} \times \mathbf{SO}(3)_{\text{L}} \times \mathbf{P} \times \mathbf{T},$$

which is the product of global gauge rotations, spin rotations, orbital rotations, space inversion, and time-reversal, respectively. The resulting free energy functional is

$$(5.4) \quad \Omega[A] = \int_V d^3r (f_{\text{bulk}}[A] + f_{\text{grad}}[A]).$$

The terms f_{bulk} and f_{grad} are given by

$$(5.5) \quad \begin{aligned} f_{\text{bulk}}[A] = & \alpha(T)Tr(AA^\dagger) + \beta_1 |Tr(AA^T)|^2 + \beta_2 [Tr(AA^\dagger)]^2 \\ & + \beta_3 Tr[AA^T(AA^T)^*] + \beta_4 Tr[(AA^\dagger)^2] + \beta_5 Tr[AA^\dagger(AA^\dagger)^*] , \end{aligned}$$

$$(5.6) \quad \begin{aligned} f_{\text{grad}}[A] = & K_1 A_{\alpha j, k}^* A_{\alpha j, k} + K_2 A_{\alpha j, j}^* A_{\alpha k, k} + K_3 A_{\alpha j, k}^* A_{\alpha k, j} \\ & + \frac{2}{r} \text{Re} \{ K_1 (A_{rj}^* A_{\phi j, j} - A_{\phi j}^* A_{rj, \phi} + A_{ir}^* A_{i\phi, \phi} - A_{i\phi}^* A_{ir, \phi}) \\ & \quad + K_2 (A_{r\phi}^* A_{\phi j, j} - A_{\phi\phi}^* A_{rj, j} + A_{ir}^* A_{ij, j}) \\ & \quad + K_3 (A_{rj}^* A_{\phi\phi, j} - A_{\phi j}^* A_{r\phi, j} + A_{ir}^* A_{i\phi, \phi} - A_{i\phi}^* A_{i\phi, r}) \} \\ & + \frac{1}{r^2} \{ K_1 [A_{rj}^* A_{rj} + A_{\phi j}^* A_{\phi j} + A_{ir}^* A_{ir} + A_{i\phi}^* A_{i\phi} + 4\text{Re}(A_{r\phi}^* A_{r\phi} - A_{rr}^* A_{\phi\phi})] \\ & \quad + (K_2 + K_3) [|A_{r\phi}|^2 + |A_{\phi\phi}|^2 + A_{ir}^* A_{ir} + 2\text{Re}(A_{r\phi}^* A_{\phi r} - A_{rr}^* A_{\phi\phi})] \} , \end{aligned}$$

where A^\dagger (A^T) is the adjoint (transpose) of A , and

$$(5.7) \quad A_{\alpha i, j} \equiv \left\{ \frac{\partial A_{\alpha i}}{\partial r}, \frac{1}{r} \frac{\partial A_{\alpha i}}{\partial \phi}, \frac{\partial A_{\alpha i}}{\partial z} \right\}_j .$$

The term f_{bulk} holds for any orthogonal coordinate system, whereas f_{grad} is coordinate specific and given in the form derived by Buchholtz and Fetter.[20] In the weak-coupling

BCS limit the material parameters,

$$(5.8) \quad \alpha^{\text{wc}}(T) = \frac{1}{3}N(0)(T/T_c - 1),$$

$$(5.9) \quad 2\beta_1^{\text{wc}} = -\beta_2^{\text{wc}} = -\beta_3^{\text{wc}} = -\beta_4^{\text{wc}} = \beta_5^{\text{wc}},$$

$$(5.10) \quad \beta_1^{\text{wc}} = -\frac{N(0)}{(\pi k_B T_c)^2} \left\{ \frac{1}{30} \left[\frac{7}{8} \zeta(3) \right] \right\},$$

$$(5.11) \quad K_1^{\text{wc}} = K_2^{\text{wc}} = K_3^{\text{wc}} = \frac{7\zeta(3)}{60}N(0)\xi_0^2,$$

are determined by the normal-state (single-spin) density of states at the Fermi energy, $N(0)$, the bulk superfluid transition temperature, T_c , and the Fermi velocity, v_f . Note that $\xi_0 = \hbar v_f / 2\pi k_B T_c$ is the Cooper pair correlation length, which varies from $\xi_0 \simeq 770 \text{ \AA}$ at $p = 0$ bar to $\xi_0 \simeq 160 \text{ \AA}$ at $p = 34$ bar. The equilibrium order parameter is obtained from minimization of the free energy functional by solving the Euler-Lagrange equations obtained from the functional gradient $\delta\Omega[A]/\delta A^\dagger = 0$.

5.3.1. Strong-coupling Corrections

The weak-coupling GL material parameters are derived from the leading order contribution to the full Luttinger-Ward free energy functional as an expansion in the small parameter T/T_F , where $T_F = E_F/k_B \approx 1 \text{ K}$ is the Fermi temperature. In particular, $\Omega^{\text{wc}} \sim (T_c/T_F)^2 E_N$, where E_N is the ground-state energy of the normal Fermi liquid. The next-to-leading corrections to the weak-coupling GL functional enter as corrections to the fourth-order weak-coupling material coefficients. These corrections are of order $\Delta\beta_i^{\text{sc}} \approx \beta_i^{\text{wc}}(T/T_F)\langle w_i|A|^2 \rangle$, where $\langle w_i|A|^2 \rangle$ is a weighted average of the square of the scattering amplitude for binary collisions between quasiparticles on the Fermi surface.[72]

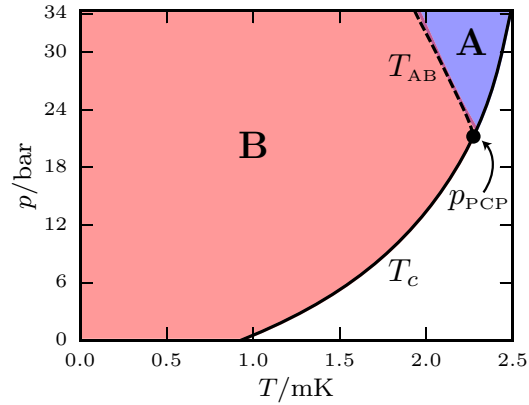


Figure 5.1. The bulk phase diagram showing the regions of stability of the A (blue) and B (red) phases using the experimental β s with linear T scaling. The dashed line is the experimental A-B transition line terminating at the experimental PCP point.

At high pressures, scattering due to ferromagnetic spin fluctuations largely compensates the small parameter T/T_F , resulting in substantial strong-coupling corrections.[81]

While the $\Delta\beta_i^{\text{sc}}$'s may be calculated theoretically through a model of the quasiparticle scattering amplitude[81], the most current determinations come from comparison with experiment.[23]¹ In the main analysis presented here we use the set of $\{\beta_i\}$ reported by Choi et al.[23] These β -parameters reproduce the heat capacity jumps for the A and B transitions, which is essential when considering the energetics of A and B-like phases. In particular, the A phase correctly appears as a stable phase above the polycritical point $p_{\text{PCP}} = 21.22$ bar; however, in fourth-order GL theory it is the only stable phase at all temperatures above the PCP, i.e. the standard fourth-order GL theory fails to account for the A-B transition line, $T_{\text{AB}}(p)$. The missing transition line is traced to the omission of the temperature dependence of the fourth-order β parameters in the neighborhood of a tri-critical point. In particular, the tri-critical point is defined by the intersection

¹This is no longer true. We report more accurate strong-coupling beta parameters in Chapter 8.

of the second-order transition line given by $\alpha(T_c, p) = 0$, and the first-order boundary line separating the A- and B-phases given by $\Delta\beta_{AB}(T_{AB}, p) \equiv \beta_A - \beta_B = 0$. Note that $\beta_A \equiv \beta_{245}$ and $\beta_B \equiv \beta_{12} + \frac{1}{3}\beta_{345}$ where we use the standard notation, $\beta_{ijk\dots} = \beta_i + \beta_j + \beta_k + \dots$ [72] At the PCP we have $T_{AB}(p_{\text{PCP}}) = T_c(p_{\text{PCP}})$. But, for $p > p_{\text{PCP}}$ the lines separate and we must retain both the temperature and pressure dependences of $\Delta\beta_{AB}(T, p)$ to account for $T_{AB}(p)$ in the vicinity of p_{PCP} . This is achieved with remarkable success by making a single correction to the standard treatment of strong-coupling corrections within GL theory. Near T_c the leading-order strong-coupling corrections to the weak-coupling β parameters scale as $\Delta\beta_i^{\text{sc}} \sim (T/T_F)|\beta_1^{\text{wc}}|$, where the linear scaling with T/T_F originates from the limited phase space for binary collisions of quasiparticles at low temperatures. Resolving the degeneracy between the A- and B-phases near p_{PCP} is achieved by retaining the linear T dependence of the strong-coupling corrections to the β parameters. Thus, we separate the β parameters determined at p and $T_c(p)$ into the weak- and strong-coupling parts using Eq. 5.9, and then scale the strong-coupling corrections, $\Delta\beta_i^{\text{sc}}$, determined at $T_c(p)$ in Ref. [23] and listed in Tables 5.1 and 5.2,

$$(5.12) \quad \beta_i(T, p) = \beta_i^{\text{wc}}(p, T_c(p)) + \frac{T}{T_c} \Delta\beta_i^{\text{sc}}(p),$$

$$(5.13) \quad \text{with } \Delta\beta_i^{\text{sc}}(p) = \beta_i(p, T_c(p)) - \beta_i^{\text{wc}}(p, T_c(p)).$$

The resulting bulk phase diagram predicted by these GL parameters accounts remarkably well for the experimental A-B transition line, $T_{AB}(p)$, as shown in Fig. 5.1, as well as the heat capacity jumps and the PCP along $T_c(p)$. This result for the bulk phase diagram gives us confidence in our predictions for the equilibrium phases of confined ^3He based on

strong-coupling GL theory. The main analysis and predictions for inhomogeneous phases of superfluid ^3He reported here are based on the strong-coupling material parameters from Ref. [23] combined with the known pressure-dependent material parameters, v_f , T_c , and ξ_0 as listed in Table 5.1, and the temperature scaling in Eq. 5.12 that accounts for the relative reduction of strong-coupling effects below T_c . [82]

5.3.2. Sauls-Serene β parameters

The individual $\Delta\beta_i^{\text{sc}}$ parameters reported by Choi et al. [23] differ from those calculated from leading order strong-coupling theory, or those obtained from the analysis of different experiments, even though the different sets predict the same bulk phase diagram.

As a test of the sensitivity of our GL predictions for new phases in confined geometries to the details of the model for the strong-coupling GL β parameters we also calculated the phase diagram based on the $\{\beta_i\}$ predicted by the leading order strong-coupling theory. [72, 81] The theoretical values for the strong-coupling β parameters are determined by angular averages of the normal-state quasiparticle scattering rate. The analysis of Sauls and Serene is based on a quasiparticle scattering amplitude that accounts for the effective mass, the ferromagnetic enhancement of the spin susceptibility and the normal-state transport coefficients. [81] The Sauls-Serene β -parameters, summarized in Tables 5.3 and 5.4, reproduce the relative stability of the bulk A and B phases, albeit with an elevated polycritical pressure of $p_{\text{PCP}} \simeq 28$ bar.

The results for the phase diagram with these two different sets of $\Delta\beta_i^{\text{sc}}$, discussed in Sec. 5.5, give robust predictions for the relative stability of new inhomogeneous phases of ^3He confined in cylindrical pores.

5.3.3. Boundary Conditions

For planar surfaces there are two limiting boundary conditions applicable within GL theory: maximal pairbreaking, resulting from retro-reflection of quasiparticles,[77] and minimal pairbreaking, resulting from specular reflection.[5] If we use cartesian coordinates and take the surface to lie along the $x - y$ plane with ${}^3\text{He}$ occupying $z > 0$, then maximal pairbreaking is defined by the condition

$$(5.14) \quad A_{\alpha i} \Big|_{z=0} = 0 \quad \forall i \in \{x, y, z\},$$

while minimal pairbreaking is defined by the conditions

$$(5.15) \quad \begin{aligned} A_{\alpha z} \Big|_{z=0} &= 0, \\ \nabla_z A_{\alpha x} \Big|_{z=0} &= \nabla_z A_{\alpha y} \Big|_{z=0} = 0. \end{aligned}$$

In a cylindrical pore, additional care needs to be given to the boundary conditions due to the presence of curvature on scales comparable to the coherence length. While the boundary condition for maximal pairbreaking is not modified, the curved surface of the pore modifies the minimal pairbreaking boundary condition for the azimuthal orbital components of the order parameter, $A_{\alpha\phi}$. Fetter and Buchholtz proposed a minimal pairbreaking boundary condition in GL theory based on the Euler-Lagrange boundary term of the GL equations with a cylindrical surface,[20]

$$(5.16) \quad \frac{\partial A_{\alpha z}}{\partial r} \Big|_{r=R} = 0, \quad A_{\alpha r} \Big|_{r=R} = 0,$$

$$(5.17) \quad \frac{\partial A_{\alpha\phi}}{\partial r} \Big|_{r=R} = \frac{1}{R} A_{\alpha\phi} \Big|_{r=R}.$$

We introduce an extension of these boundary conditions which interpolates between the two extremes of minimal and maximal pairbreaking. The extension is based on Ambegaokar, de Gennes, and Rainer’s (AdGR) analysis[5] of the effects of diffuse scattering by an atomically rough surface on the transverse components of the p-wave orbital order parameter. AdGR showed that diffuse scattering leads to a boundary condition in which the components that are transverse to the average normal direction of the surface are finite, but extrapolate linearly to zero past the boundary at a distance $b_T = 0.54\xi_0$. This idea can be turned into a more general boundary condition for GL theory in a cylindrical geometry as

$$\begin{aligned}
 A_{\alpha r}|_{r=R} &= 0, \\
 \frac{\partial A_{\alpha z}}{\partial r}\Big|_{r=R} &= -\frac{1}{b_T}A_{\alpha z}|_{r=R}, \\
 \frac{\partial A_{\alpha\phi}}{\partial r}\Big|_{r=R} &= \left(\frac{1}{R} - \frac{1}{b_T}\right)A_{\alpha\phi}|_{r=R}.
 \end{aligned}
 \tag{5.18}$$

where $b'_T \equiv b_T/\xi_0$ can be treated as a parameter that varies between the maximal pairbreaking ($b'_T \rightarrow 0$) and minimal pairbreaking ($b'_T \rightarrow \infty$) limits. This generalized “AdGR” boundary condition provides a useful extension of the typical Ginzburg-Landau boundary conditions.

5.4. Superfluid Phases

The pore geometry reduces the maximal symmetry group for confined ^3He to

$$\mathbf{G} = \text{SO}(3)_S \times \text{D}_{\infty\text{h}} \times \mathbb{T}
 \tag{5.19}$$

where $D_{\infty h}$ is the point group of the pore and is obtained from the point group of the circle, $C_{\infty v} = SO(2) \times \{e, \pi_{zx}\}$, by $D_{\infty h} = C_{\infty v} \times \{e, \pi_{xy}\}$, where π_{xy} is a reflection through the $x - y$ plane. By numerically minimizing the GL free energy with respect to all order parameter components we identify four equilibrium superfluid phases for the 200 nm diameter pore. In these calculations we assume the phases are translationally invariant along the z axis.

Recently Aoyama has shown that a translational symmetry breaking “stripe” B-like phase along the axis of the channel may be possible in cylindrical geometries, stabilized with an anisotropic boundary condition that implements specular reflection for scattering along z , but retro-reflection in the $r-\phi$ plane. This enhances $A_{\alpha z}$ on the boundary relative to $A_{\alpha\phi}$.^[9] Our boundary condition has the opposite anisotropy. Thus, with our formulation it is unclear if conditions allow for an energetically stable B-like stripe phase. This question will be addressed in a separate report.

5.4.1. Polar (P_z) Phase

Radial confinement in a cylindrical pore leads to the stability of the one-dimensional polar (P_z) phase below $T_{c1} \leq T_c$, where T_{c1} is the transition temperature from the normal state. The P_z phase is a time-reversal invariant equal-spin pairing (ESP) phase with an order parameter of form

$$(5.20) \quad A_{\alpha i} = \Delta_z(r) \hat{d}_\alpha \hat{z}_i,$$

with radial profile shown in Fig. 5.2. The P_z order parameter becomes spatially homogeneous with $T_{c1} \rightarrow T_c$ in the limit of specular scattering, and will be the first superfluid

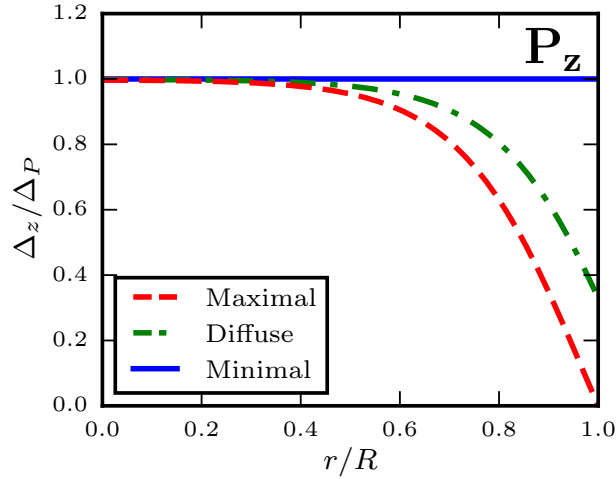


Figure 5.2. Order parameter amplitudes for the P_z phase as a function of r at $p = 26$ bar and $T = 0.5T_c$ for retro-reflection (maximal pair-breaking), diffuse ($b'_T = 0.54$), and specular (minimal pair-breaking) boundary conditions. Values are scaled by the unconfined polar phase amplitude $\Delta_P^2 = |\alpha(T)|/2\beta_{12345}$. For minimal pairbreaking boundary conditions the P_z phase is spatially homogeneous within the pore.

phase upon cooling from the normal state, except for the exceptional case of perfect specular reflection and perfect cylindrical cross-section (see Sec. 5.4.3). The residual symmetry group of the P_z phase is $H = \text{SO}(2)_{S_d} \times Z_2^{\text{spin}} \times D_{\infty h}^{L,\pi} \times T$, where $D_{\infty h}^{L,\pi} \equiv C_{\infty v} \times \{e, e^{i\pi}\pi_{xy}\}$. Thus, the P_z phase breaks spin rotational symmetry but retains the full orbital point group, $D_{\infty h}$, by combining it with an element of the gauge group. Since the radius $R = 100$ nm of the pore is much less than the dipole coherence length, $\xi_D \approx 10 - 20 \mu\text{m}$, the spin quantization axis, \hat{d} , for the ESP state is to high accuracy uniform in space. All transitions to and from the P_z phase that we find are second order.

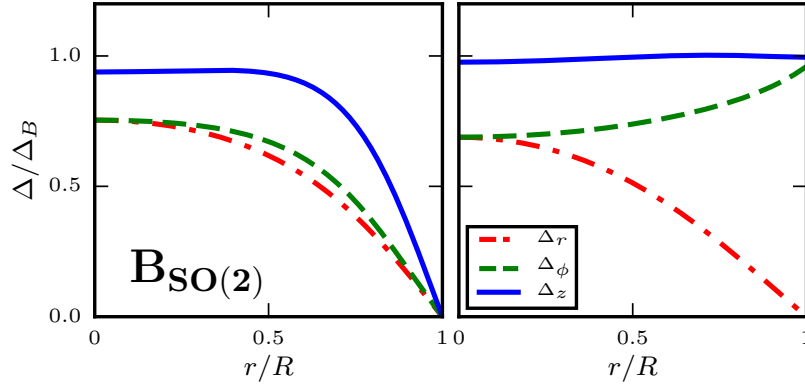


Figure 5.3. Order parameter amplitudes for the $B_{\text{SO}(2)}$ phase as a function of r at $p = 26$ bar and $T = 0.5 T_c$. The left figure depicts maximal pairbreaking ($b'_T = 0$) while the right shows minimal pairbreaking ($b'_T = \infty$). Values are scaled by the bulk B phase order parameter, $\Delta_B^2 = |\alpha(T)|/6(\beta_{12} + 1/3\beta_{345})$.

5.4.2. $B_{\text{SO}(2)}$ Phase

The $B_{\text{SO}(2)}$ phase is the analogue to the bulk B phase for the cylindrical pore geometry, and is stabilized at low temperatures and preferentially favored by strong pairbreaking on the boundary. The residual symmetry of the $B_{\text{SO}(2)}$ phase is $\mathbf{H} = \mathbf{D}_{\text{oh}}^{\text{L+S}} \times \mathbf{T}$, joint spin and orbital \mathbf{D}_{oh} transformations combined with time-reversal. The order parameter is represented as

$$(5.21) \quad A_{\alpha i} = \Delta_r(r) \hat{r}_\alpha \hat{r}_i + \Delta_\phi(r) \hat{\phi}_\alpha \hat{\phi}_i + \Delta_z(r) \hat{z}_\alpha \hat{z}_i,$$

with the radial profiles shown in Fig. 5.3.

5.4.3. $A_{\text{SO}(2)}$ Phase

In addition to the P_z and $B_{\text{SO}(2)}$ phases, we find two stable chiral A-like phases. The higher symmetry $A_{\text{SO}(2)}$ phase, reminiscent of the “radial disgyration texture” of bulk $^3\text{He-A}$, is favored by weak pair-breaking on the boundary. The residual symmetry group of the

$\text{A}_{\text{SO}(2)}$ phase is $\text{H} = \text{SO}(2)_{\text{Sd}} \times \text{Z}_2^{\text{spin}} \times \text{D}_{\infty\text{h}}^{\text{L,T}}$, where $\text{D}_{\infty\text{h}}^{\text{L,T}} \equiv \text{SO}(2) \times \{\text{e}, \text{t}\pi_{zx}\} \times \{\text{e}, e^{i\pi}\text{t}\pi_{xy}\}$ and t is time reversal. The order parameter takes the form

$$(5.22) \quad A_{\alpha i} = \hat{d}_{\alpha} [\Delta_z(r) \hat{z}_i + i \Delta_{\phi}(r) \hat{\phi}_i]$$

which is transverse to the pore boundary with radial profiles shown in Fig. 5.4. The chiral vector,

$$(5.23) \quad \vec{l} = -\Delta_z(r) \Delta_{\phi}(r) \hat{r},$$

shown in Fig. 5.5, is radial except at the origin where \vec{l} vanishes; the gradient terms in the GL functional require $\Delta_{\phi} = 0$, yielding a polar order parameter at the core of the cylindrical pore. The resulting chiral field is analogous to a radial disgyration - a topological line defect of bulk $^3\text{He-A}$. This form for \vec{l} results in a zero average of $\vec{l}(\vec{r})$ over the cylindrical pore, which leads to distinctly different NMR frequency shift for the $\text{A}_{\text{SO}(2)}$ phase as compared with a chiral state with a non-vanishing average chiral axis, $\langle \vec{l}(\vec{r}) \rangle \neq 0$, as discussed in Sec. 5.6. For the specular boundary condition proposed in Ref. [20] (Eq. 5.18 with $b'_T \rightarrow \infty$), the $\text{A}_{\text{SO}(2)}$ phase entirely supplants the P_z phase, and onsets at the bulk transition temperature T_c , despite being spatially inhomogeneous.

5.4.4. A_{C_2} Phase

A lower symmetry A-like phase, denoted as A_{C_2} , is an inhomogenous version of the the circular disgyration, or Pan Am texture.[54, 37] This phase spontaneously breaks continuous $\text{SO}(2)_L$ symmetry of the cylinder and, unlike the $\text{A}_{\text{SO}(2)}$ phase, has a finite value for the spatially averaged chiral axis, $\langle \vec{l} \rangle \neq 0$, that may point in any direction in the $x - y$

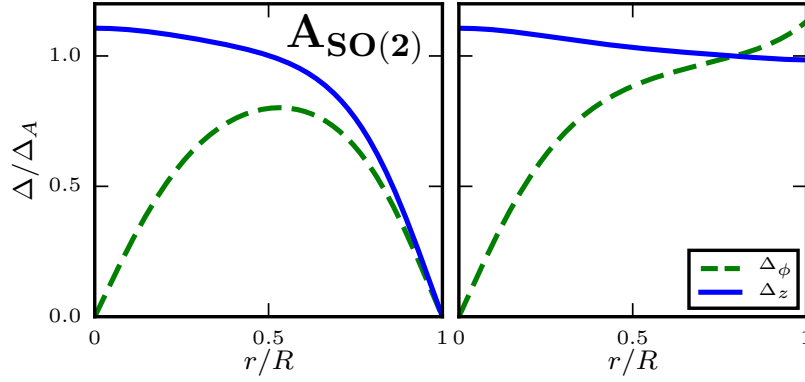


Figure 5.4. Order parameter amplitudes for the $A_{\text{SO}(2)}$ phase as a function of r at $p = 26$ bar and $T = 0.5 T_c$. The left figure depicts maximal pairbreaking while the right shows minimal pairbreaking. Values are scaled by the bulk A phase order parameter, $\Delta_A^2 = |\alpha(T)|/4\beta_{245}$.

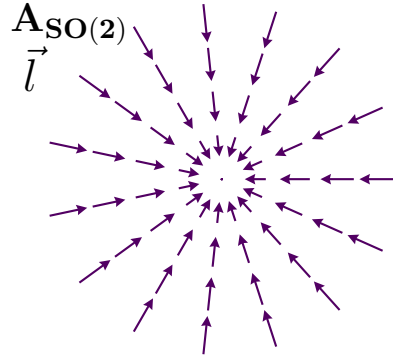


Figure 5.5. Chiral axis \hat{l} for the $A_{\text{SO}(2)}$ phase at $p = 26$ bar, $T = 0.5 T_c$, and minimal pairbreaking boundaries. Arrow lengths are scaled by $|\Delta_\phi|$.

plane. For convenience we take $\langle \vec{l} \rangle \parallel \hat{y}$, with an order parameter of the form

$$(5.24) \quad A_{\alpha i} = \hat{d}_\alpha [\Delta_z(r, \phi) \hat{z}_i + i \Delta_r(r, \phi) \hat{r}_i + i \Delta_\phi(r, \phi) \hat{\phi}_i].$$

The residual symmetry group is then $H = \text{SO}(2)_{\text{Sd}} \times \text{Z}_2^{\text{spin}} \times \text{D}_{2\text{h}}^{\text{L,T}}$, where $\text{D}_{2\text{h}}^{\text{L,T}} \equiv$

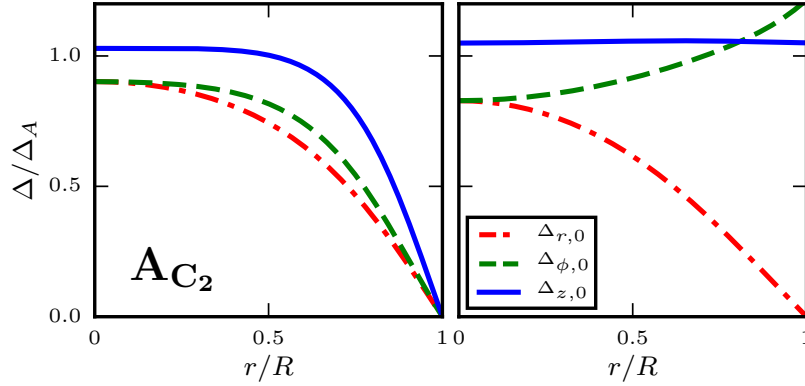


Figure 5.6. Dominant order parameter amplitudes for the AC_2 phase at $p = 26$ bar and $T = 0.5 T_c$. The left figure depicts maximal pairbreaking while the right shows minimal pairbreaking. Values are scaled by the bulk A phase amplitude $\Delta_A^2 = |\alpha(T)|/4\beta_{245}$.

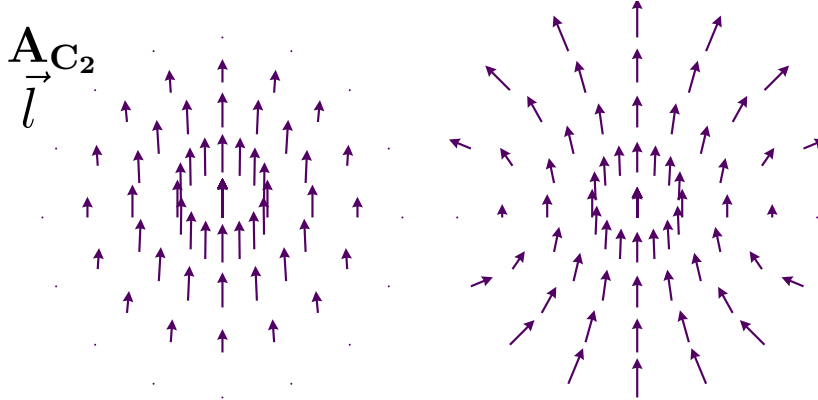


Figure 5.7. Chiral axis \hat{l} for the AC_2 phase at $p = 26$ bar and $T = 0.5 T_c$. (Left) Maximal pairbreaking boundaries result in a nearly uniform \hat{l} direction. (Right) Minimal pairbreaking, on the other hand, gives the characteristic “Pan Am” configuration. Arrow lengths are scaled by $(\Delta_r^2 + \Delta_\phi^2)^{1/2}$.

$\{\mathbf{e}, t\mathbf{c}_2, \pi_{zx}, t\pi_{zy}\} \times \{\mathbf{e}, e^{i\pi}t\pi_{xy}\}$. The AC_2 phase has a pair of disgyrations on the boundary along an axis perpendicular to \hat{z} and $\langle \hat{l} \rangle$, as can be seen for the case of minimal pairbreaking in Fig. 5.7. The AC_2 phase is energetically favorable relative to the $\text{ASO}(2)$

phase for strong pairbreaking on the boundary. In this case the boundary effectively “censors” the energy cost of the A_{C_2} disgyrations. The suppression of the disgyrations is evident in Fig. 5.7.

The A_{C_2} phase is the only phase we find with broken axial symmetry, and thus explicit ϕ dependence. It is convenient to expand its amplitudes in terms of sines and cosines that respect symmetry,

$$(5.25) \quad A_{\alpha i} = \hat{d}_\alpha \sum_{j=0}^{\infty} \left\{ i \Delta_{r,j}(r) \cos[(2j+1)\phi] \hat{r}_i - i \Delta_{\phi,j}(r) \sin[(2j+1)\phi] \hat{\phi}_i + \Delta_{z,j}(r) \cos(2j\phi) \hat{z}_i \right\}.$$

Numerical solutions to the GL equations converge rapidly as a function of the number of azimuthal harmonics, which greatly simplifies the numerical minimization compared to allowing for an arbitrary ϕ dependence.

5.5. Phase Diagram

The phase diagram for superfluid ^3He confined within a pore is strongly dependent upon the boundary conditions. We first fix $R = 100$ nm and consider the phase diagram for four different values of b'_T , ranging from minimal to maximal pairbreaking as shown in Figures 5.8 and 5.9. For strong pairbreaking (Fig. 5.8) the phase diagram is dominated by the $B_{SO(2)}$, A_{C_2} , and P_z phases. In this regime, our phase diagram differs from previous calculations[53, 32] due to the appearance of the A_{C_2} phase, which for strong pairbreaking has a lower free energy than that of the $A_{SO(2)}$ phase. As pairbreaking decreases on the boundary, the $A_{SO(2)}$ phase appears at high pressure, with a tri-critical point separating the $B_{SO(2)}$, $A_{SO(2)}$ and A_{C_2} phases. The $A_{SO(2)}$ phase occupies most of the superfluid

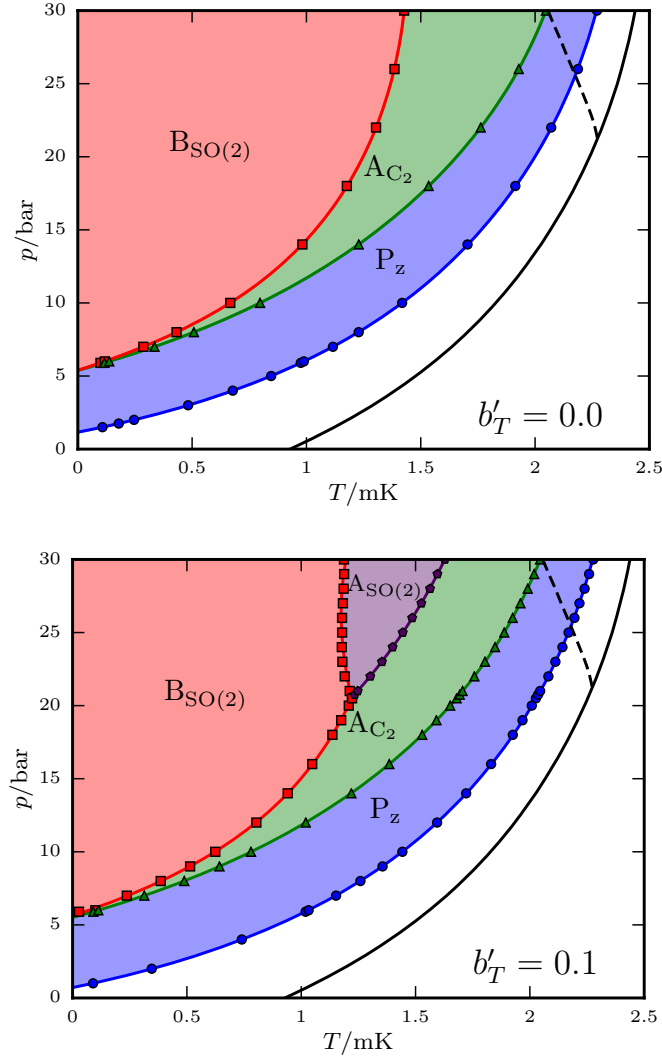


Figure 5.8. Phase diagrams for $b'_T = 0$ (maximal pairbreaking) and $b'_T = 0.1$. The $A_{\text{SO}(2)}$ phase does not appear at all for maximal pairbreaking; as pairbreaking at the boundary is relaxed it is stabilized at high pressure and displaces the $B_{\text{SO}(2)}$ and A_{C_2} phases.

phase diagram for minimal pairbreaking boundaries. It must be noted, however, that any deviation from the perfect specular condition $b'_T = \infty$ will suppress $A_{\alpha\phi}$ at the boundary

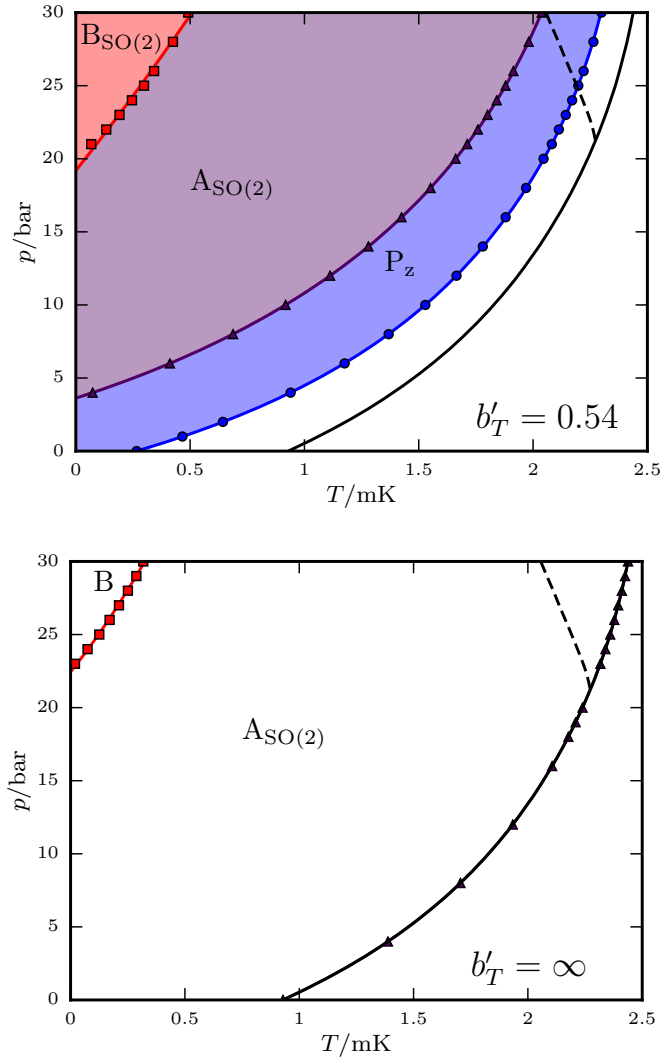


Figure 5.9. Phase diagrams for $b'_T = 0.54$ and $b'_T = \infty$ (minimal pairbreaking). As pairbreaking decreases, the A_{C_2} phase is suppressed completely and the stable range of the $B_{SO(2)}$ phase is decreased significantly. For minimal pairbreaking the $A_{SO(2)}$ phase onsets at $T = T_c$ with the P_z phase absent.

near T_c , and thus the P_z phase should always be expected to be the highest temperature superfluid phase observed experimentally.

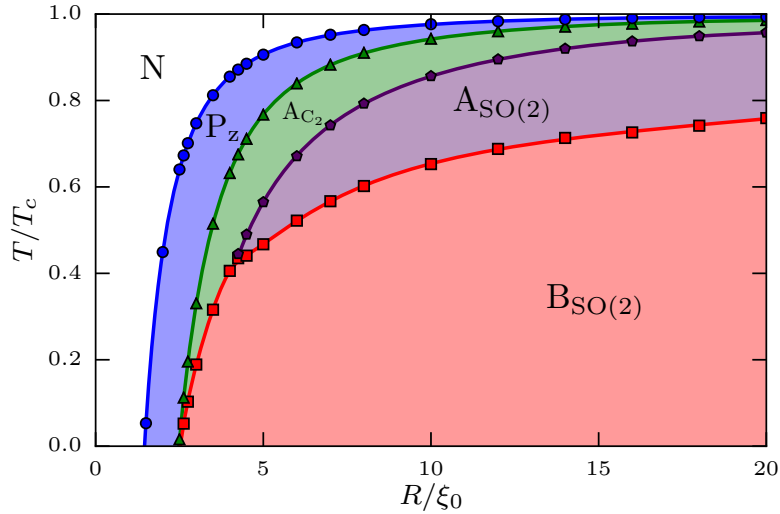


Figure 5.10. Temperature-confinement phase diagram for fixed $b'_T = 0.1$, $p = 26$ bar and the β parameters of Ref. [23].

We also consider the influence of the pore radius, R , on stability of the various phases. Fig. 5.10 shows the phase diagram of stable phases in a cylindrical channel as a function of the pore radius relative to the coherence length, R/ξ_0 . For a range of sufficiently small R/ξ_0 only the P_z phase is stable; the $B_{SO(2)}$, A_{C_2} , and $A_{SO(2)}$ phases enter the diagram with increasing R . The $A_{SO(2)}$ phase is favored over the A_{C_2} phase for large radii; however, the relative stability of these two chiral phases is sensitive to boundary scattering, i.e. b'_T , as shown in Figs. 5.8 and 5.9. For larger radii of order the dipole coherence length, $R \approx \xi_D \approx 10 \mu\text{m}$, the spin quantization axis, \hat{d} , for the A_{C_2} and $A_{SO(2)}$ phases is no longer constrained to be spatially uniform, and for $R \gg \xi_D$ these phases become “dipole-locked” with $\hat{d} \parallel \hat{l}$. [20]

We also tested the robustness of our predictions for the phase diagram against a different set of strong-coupling β parameters, specifically the Sauls-Serene set of $\Delta\beta_i^{\text{sc}}$ calculated on the basis of leading order strong-coupling theory [72] based on a quasiparticle

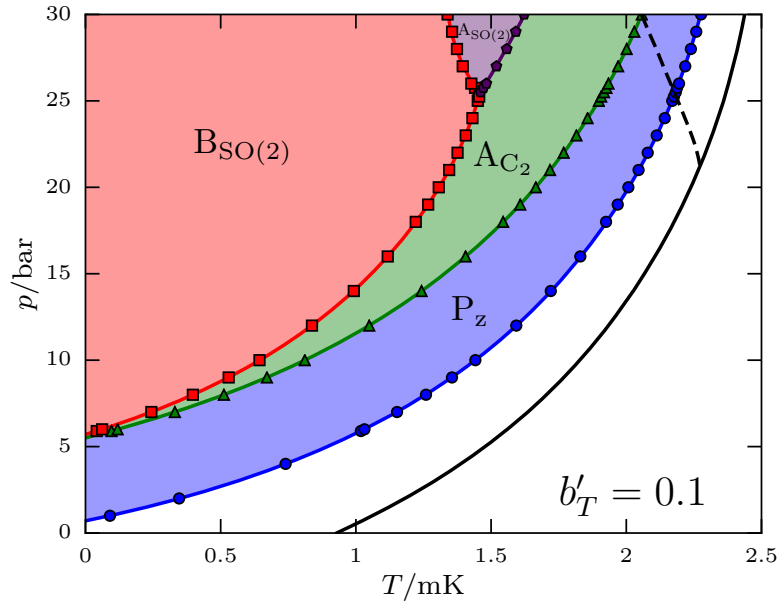


Figure 5.11. Phase diagram for $b'_T = 0.1$ using the β parameters of Sauls and Serene.[81] The resulting phase boundaries are largely left unchanged except for the shift upward in pressure of the tricritical point, roughly corresponding to the difference of the Choi et al[23] polycritical point, $p_{\text{PCP}} \approx 21$ bar, and the Sauls and Serene polycritical point, $p_{\text{PCP}} \approx 28$ bar.

scattering amplitude that accounts for both the normal-state effective mass, ferromagnetic enhancement of the spin susceptibility and transport coefficients.[81] These β parameters account for the relative stability of the bulk A- and B-phases, but have distinctly different predictions for the pressure dependences of the strong-coupling corrections: $\Delta\beta_i^{\text{sc}}$. The key result is that the structure of the phase diagram is unchanged with a different set of strong-coupling β parameters, i.e. the relative stability of the P_z , $B_{\text{SO}(2)}$, A_{C_2} , and $A_{\text{SO}(2)}$ phases is unchanged between the two sets of strong-coupling β parameters. This is shown in Fig. 5.10.

5.6. NMR Signatures

The superfluid phases obtained for the narrow pore neglect the nuclear magnetic dipole energy. This is an excellent approximation since the nuclear dipole-dipole interaction energy for dipoles separated by the mean interatomic spacing a is very small compared to the pairing energy scale, $\frac{1}{a^3} (\gamma\hbar/2)^2 \approx 10^{-4} \text{ mK} \ll T_c \approx \text{mK}$. Nevertheless, the dipole energy gives rise to two important effects - (i) it partially resolves relative spin-orbital degeneracy of the equilibrium states, and (ii) it generates a dynamical torque from the Cooper pairs acting on the total spin when the latter is driven out of equilibrium. The dipolar torque leads to NMR frequency shifts that are characteristic signatures of the broken symmetry phases. In the following we report results for the nonlinear NMR frequency shifts that are “fingerprints” of the $P_{\mathbf{z}}$, $A_{\mathbf{SO}(2)}$, $A_{\mathbf{C}_2}$, and $B_{\mathbf{SO}(2)}$ phases. Our analysis is based on a spatial and temporal averaging of the Leggett equations[48] for the nonlinear spin dynamics of superfluid ^3He .

The dipolar interaction breaks relative spin-orbit rotation symmetry, thus reducing the maximal rotational symmetry from $\text{SO}(3)_S \times \text{SO}(3)_L$ to $\text{SO}(3)_{L+S}$. This is reflected by additional terms in the GL free energy functional, $\Delta\Omega_D = \int_V d^3r f_D[A]$, where

$$(5.26) \quad f_D = g_D (|\text{Tr}A|^2 + \text{Tr}AA^*)$$

is the mean pairing contribution to the nuclear dipolar interaction energy, with $g_D \sim (N(0)\gamma\hbar/2)^2 > 0$. A convenient expression for g_D is $g_D = \frac{\chi}{2\gamma^2} \Omega_A^2 / \Delta_A^2$, where the A-phase susceptibility, $\chi = \chi_N$, is equal to the normal-state spin susceptibility, Δ_A is the bulk A-phase order parameter, and Ω_A is the corresponding longitudinal resonance frequency. The dipole energy is a weak perturbation that resolves (partially) the relative spin- and

orbital degeneracy of the zero-field phases of the cylindrical pore. In particular, for the ESP states of the form $A_{\alpha i} = \hat{d}_\alpha \Delta_i(\vec{r})$ the dipolar energy is given by $f_D = g_D |\hat{d} \cdot \vec{\Delta}|^2$, which is minimized if \hat{d} *locally* orients perpendicular to the two dominant orbital components. However, spatial variations of the order parameter cost gradient energy. In the case of the orbital components the spatial profiles are already optimized by minimizing the GL functional subject to the boundary conditions of the confining geometry. For the inhomogeneous phases of superfluid ^3He in a pore of radius $R = 100$ nm, the spatial variations of the orbital components occur on a length scale that is short compared to the dipole coherence length, $\xi_D \equiv \sqrt{g_D/K_1} \approx 10$ μm . Thus, spatial variations of \hat{d} on such short length scales of the pore geometry cost much more than the dipole energy. As a result \hat{d} “unlocks” from the *local* variations of the orbital order parameter. This allows us to average the orbital components over the cross-section of the cylindrical pore and treat the spin degrees of freedom as spatially uniform on the scale of R . For the non-ESP $\text{B}_{\text{SO}(2)}$ phase the spin structure is described by an orthogonal matrix, $\mathbf{R}[\alpha, \beta, \gamma]$, representing the *relative* rotation of the spin and orbital coordinates.

The orientation of the spin coordinates of the Cooper pairs is also influenced by the nuclear Zeeman energy,

$$(5.27) \quad \Delta\Omega_Z = g_z \int_V d^3r H_\alpha (A_{\alpha i} A_{\beta i}^*) H_\beta,$$

where

$$(5.28) \quad g_z = \frac{N(0)\gamma^2\hbar^2}{(1 + F_0^a)^2} \frac{7\zeta(3)}{48\pi^2 T_c^2} > 0,$$

is the Zeeman coupling constant in the weak-coupling limit. For ESP states the static NMR field prefers $\hat{d} \perp \vec{H}$.

5.6.1. Fast vs. slow spin dynamics

The nuclear dipolar energy generates frequency shifts, $\Delta\omega = \omega - \omega_L$, of the NMR resonance line for superfluid ^3He away from the Larmor frequency, $\omega_L = \gamma H$, that are sensitive to the spin and orbital structure of the ordered phase, the strength and orientation of the static NMR field, and the *rf* field (“tipping field”) used to excite the nuclear spins. In the high field limit, $\omega_L \gg \Omega$, where $\Omega \sim \Omega_A$ is the dynamical timescale set by the dipole energy, we use Fomin’s formulation of the spin dynamics based on the separation of fast and slow timescales for the dynamics of the magnetization (see also Ref. [22]), or total spin, $\vec{S}(t)$, and the order parameter, $A(t)$. The “fast” response is on the scale set by the Larmor frequency, $\omega \sim \omega_L$, while the “slow” response is set by the dipolar frequency of order Ω_A . [33] Note that the static NMR field is still assumed to be small in the sense that the Zeeman energy is much smaller than the condensation and gradient energies associated with the orbital components of the order parameter. Thus, the dynamical contributions to the nuclear dipole and Zeeman energies can be calculated on the basis of the solutions for the orbital order parameter in zero field. However, for static NMR fields greater than the Dipole field, $H \gg H_D \approx 30 \text{ G}$, the equilibrium orientation of the spin components of the order parameter is determined primarily by the Zeeman energy, with the dipole energy resolving any remaining degeneracy in the equilibrium orientation of the \hat{d} vector, or the rotation matrix \mathbf{R} for the $\text{B}_{\text{SO}(2)}$ state. This provides us with the initial equilibrium conditions for orientation of the spin components of the order parameter.

The spin dynamics of the superfluid phases is parametrized in terms of rotation matrices for the precession of the order parameter, e.g. $A(t)$ and total spin, $\vec{S}(t)$, following an initial *rf* excitation of the spin system. An *rf* impulse applied at $t = 0$ rotates (“tips”) the total spin, $\vec{S}(t = 0^+)$ by an angle β relative to the equilibrium spin, $\vec{S}_0 || \vec{H} \equiv H\hat{z}'$. The resulting dynamics of the order parameter for timescales, $0 < t \ll 2\pi/\Omega$, is then parametrized by[**33**]

$$(5.29) \quad A(t) = \mathbf{R}_{\mathbf{z}'}(\omega t) \mathbf{R}_{\mathbf{y}'}(\beta) \mathbf{R}_{\mathbf{z}'}(-\omega t + \vartheta) A_0,$$

where $\mathbf{y}' \perp \mathbf{z}'$ is the direction of the *rf* tipping field, and the rotation angles are defined by one “fast” angle, ωt , and two “slow” dynamical angles, β and ϑ . Inserting this expression into Eq. 5.26 for the dipole energy and averaging the result over the fast time scale, $2\pi/\omega$, gives the fast-time and short-distance scale averaged dipole energy density,

$$(5.30) \quad \overline{f_D} = \frac{\omega}{2\pi} \int_0^{\frac{2\pi}{\omega}} dt \frac{1}{V_{\text{cell}}} \int d^3r f_D[A(\vec{r}, t)].$$

This averaged dipolar energy functional determines the transverse NMR frequency shift $\Delta\omega$ as a function of tipping angle β for various orientations of the NMR field, \vec{H} , relative to the order parameter within the pore geometry. The variable ϑ – the generalization of Leggett’s rotation angle for the bulk B-phase – is fixed by the stationary condition of $\overline{f_D}$. The transverse NMR frequency shift as a function of tipping angle is then given by[**33**]

$$(5.31) \quad \omega\Delta\omega = \frac{\gamma^2}{\chi} \frac{1}{\sin\beta} \frac{d}{d\beta} \overline{f_D},$$

which provides the key NMR signatures for the phases of ^3He under strong confinement.

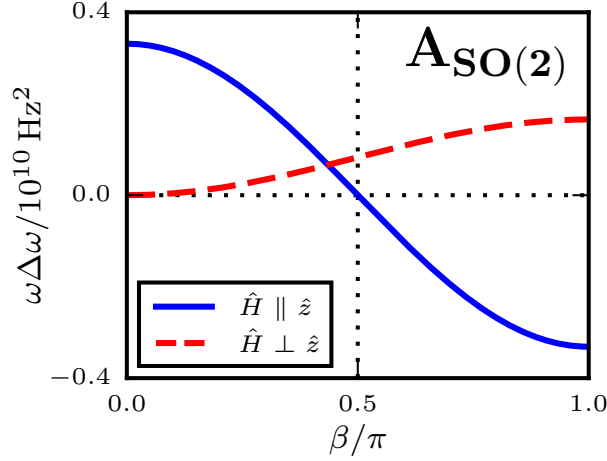


Figure 5.12. Frequency shift of the $A_{\text{SO}(2)}$ phase at $p = 26$ bar, $T = 0.5 T_c$, and $b'_T = 0$. The P_z phase has the same functional form, but with larger amplitude.

5.6.2. P_z and $A_{\text{SO}(2)}$ Phases

The P_z and $A_{\text{SO}(2)}$ phases are both ESP phases parameterized by a real \hat{d} vector with order parameters given by Eqs. 5.20 and 5.22, respectively. Spatial averaging of the dipole energy for these two phases leads to a dipole energy of the same form for both phases,

$$(5.32) \quad f_D = g_D (2 \langle \Delta_z^2 \rangle - \langle \Delta_\phi^2 \rangle) (\hat{d} \cdot \hat{z})^2,$$

where \hat{z} is the axis of the cylindrical pore, and \hat{d} is homogeneous and oriented in equilibrium in the plane perpendicular to the NMR field \vec{H} and along a direction that minimizes Eq. 5.32.

Parameterizing the direction of the NMR field in the coordinate system of the cylindrical pore by $\hat{z}' = \{\cos \phi \sin \theta, \sin \phi \sin \theta, \cos \theta\}$, carrying out the transformation Eq. 5.29

yields $\overline{f_D}$ in Eq. 5.30,

$$(5.33) \quad \overline{f_D} = \frac{1}{8} g_D (\langle \Delta_\phi^2 \rangle - 2 \langle \Delta_z^2 \rangle) [2(\cos \beta + 1)^2 \cos^2 \vartheta \sin^2 \theta + 4 \cos^2 \beta - (2 \cos \beta + 7 \cos^2 \beta) \sin^2 \theta] .$$

Since $\langle \Delta_\phi^2 \rangle - 2 \langle \Delta_z^2 \rangle < 0$ in the pore, $\overline{f_D}$ is minimized with respect to ϑ with $\vartheta = 0$. Finally, a general expression for the transverse shifts as a function of tipping angle is obtained with Eq. 5.31,

$$(5.34) \quad \omega \Delta \omega = \frac{\gamma^2}{\chi_N} g_D (2 \langle \Delta_z^2 \rangle - \langle \Delta_\phi^2 \rangle) \times \left[\cos(\beta) - \sin^2(\theta) \left(\frac{5 \cos(\beta) - 1}{4} \right) \right] .$$

The dependences on the tipping angle, β , and the polar orientation of the NMR field, θ , are identical for both the P_z and $A_{SO(2)}$ phases - only the magnitude of the shift differs between the two phases. Note in particular that the shift vanishes precisely at $\beta = \pi/2$ for $\vec{H} \parallel \hat{z}$. The result for the $A_{SO(2)}$ phase is equivalent to what is predicted for a 2D orbital glass phase of ${}^3\text{He-A}$. [28] Although the P_z and $A_{SO(2)}$ phases differ only quantitatively in their transverse NMR frequency shift, they can still be distinguished in sufficiently clean pores by the change in temperature dependence near the second order phase transition between the two phases (see Fig. 5.9), in particular the discontinuity in the derivative of the frequency shift, $d\Delta\omega/dT|_{T_{c_2}}$.

5.6.3. A_{C_2} Phase

The A_{C_2} phase, with order parameter given by Eq. 5.24, breaks $SO(2)$ orbital symmetry, and exhibits distinctly different NMR signatures compared to those of the $A_{SO(2)}$ phase.

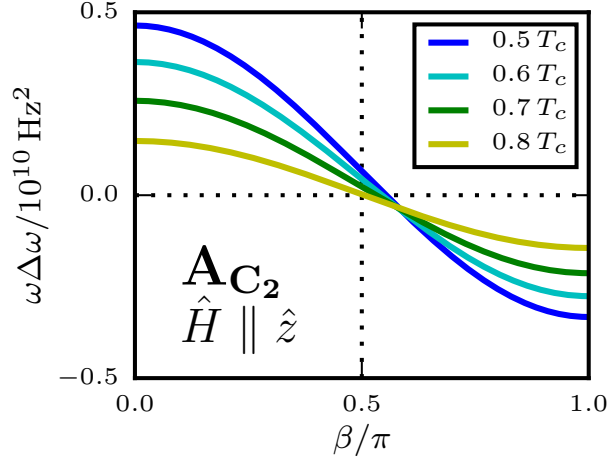


Figure 5.13. Transverse frequency shifts for the A_{C_2} phase with $\vec{H} \parallel \hat{z}$ at $p = 26$ bar, temperatures $T = 0.5 - 0.8 T_c$, and maximal pairbreaking with $b'_T = 0$.

Here we consider the two cases $\vec{H} \parallel \hat{z}$ and $\vec{H} \perp \hat{z}$. For $\vec{H} \perp \hat{z}$ the residual D_{2h} symmetry leads to a dependence of the transverse frequency shift on the azimuthal angle of \vec{H} . Due to the ϕ dependence of the order parameter it is convenient to work in Cartesian coordinates with the chiral axis fixed along $\langle \vec{l} \rangle \parallel \hat{y}$. The resulting spatial averages of the order parameter profiles entering the average dipole energy become,

$$\begin{aligned}
 \langle \Delta_x^2 \rangle &= \langle (\Delta_r \cos \phi - \Delta_\phi \sin \phi)^2 \rangle \\
 \langle \Delta_y^2 \rangle &= \langle (\Delta_r \sin \phi + \Delta_\phi \cos \phi)^2 \rangle \\
 \langle \Delta_x \Delta_y \rangle &= \langle (\Delta_r \cos \phi - \Delta_\phi \sin \phi) \\
 &\quad \times (\Delta_r \sin \phi + \Delta_\phi \cos \phi) \rangle = 0,
 \end{aligned}
 \tag{5.35}$$

For $\vec{H} \parallel \hat{z}$, the result for the transverse frequency shift for the AC_2 phase becomes

$$\begin{aligned}
 \omega\Delta\omega^{(\parallel)} &= \frac{1}{2} \frac{\gamma^2}{\chi_N} g_D \{ \langle \Delta_y^2 \rangle - \langle \Delta_x^2 \rangle \\
 &\quad - (3 \langle \Delta_x^2 \rangle + \langle \Delta_y^2 \rangle - 4 \langle \Delta_z^2 \rangle) \cos \beta \\
 &\quad + 2 | \langle \Delta_y^2 \rangle - \langle \Delta_x^2 \rangle | (1 + \cos \beta) \} .
 \end{aligned}
 \tag{5.36}$$

The results for $\omega\Delta\omega$ for several temperatures are shown in Fig. 5.13. The shift is similar to that for the P_z and $\text{ASO}(2)$ phases, except for the asymmetry of the positive and negative shifts. Note also that $\Delta\omega$ vanishes at a temperature-dependent angle $\beta^* > \pi/2$.

In contrast, for $\vec{H} = H(\cos \varphi \hat{x} + \sin \varphi \hat{y})$ the shift, $\omega\Delta\omega$, depends on the azimuthal angle φ of the static field, in addition to the tipping angle β . For an order parameter of the form in Eq. 5.24 we have $\langle \vec{l} \rangle \parallel \hat{y}$, and the resulting transverse frequency shift as a function of φ and β becomes,

$$\begin{aligned}
 \omega\Delta\omega^{(\perp)} &= \frac{1}{4} \frac{\gamma^2}{\chi_N} g_D \{ (\langle \Delta_x^2 \rangle + \langle \Delta_y^2 \rangle - 2 \langle \Delta_z^2 \rangle) (\cos \beta - 1) \\
 &\quad + (\langle \Delta_x^2 \rangle - \langle \Delta_y^2 \rangle) (1 + 7 \cos \beta) \cos 2\varphi \} .
 \end{aligned}
 \tag{5.37}$$

The results for several field orientations, $\varphi = 0, \pi/4, \pi/2$, are shown in Fig. 5.14. The tipping angle dependences for $\vec{H} \parallel \langle \vec{l} \rangle$ and $\vec{H} \perp \langle \vec{l} \rangle$ are of the same functional form as the corresponding cases for bulk $^3\text{He-A}$. There is a “magic” tipping angle of $\beta_x = \cos^{-1}(-1/7) \approx 0.545\pi$ at which $\Delta\omega(\varphi = 0) = \Delta\omega(\varphi = \pi/2)$ independent of temperature. The tipping angle dependence for $\varphi = \pi/4$ is much weaker, and qualitatively similar to that for the $\text{ASO}(2)$ phase with $\vec{H} \perp \hat{z}$. Observation of these results for several field

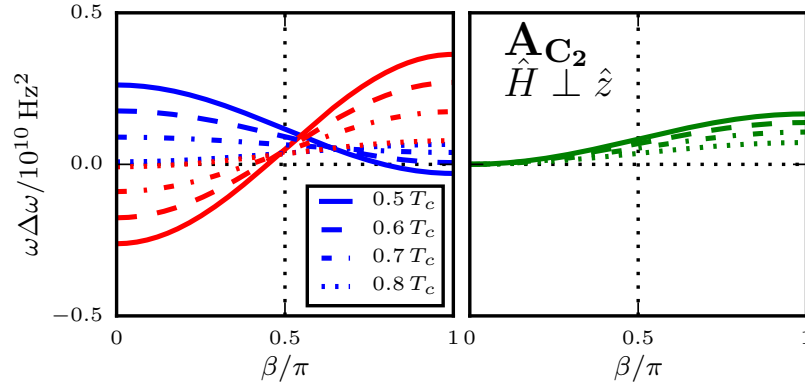


Figure 5.14. Transverse frequency shifts for the $\Lambda_{\mathbf{C}_2}$ phase with $\vec{H} \perp \hat{z}$ at $p = 26$ bar, temperatures $T = 0.5 - 0.8 T_c$, and maximal pairbreaking with $b'_T = 0$. The left panel shows the shifts for in-plane field orientation $\varphi = 0$ (blue), and $\varphi = \pi/2$ (red). The right panel shows the shifts for $\varphi = \pi/4$, which has the same functional form as that of the $\Lambda_{\mathbf{SO}(2)}$ phase.

orientations would provide a clear identification of the $\Lambda_{\mathbf{C}_2}$ phase and determine the direction of the mean chiral axis.

5.6.4. $\mathbf{B}_{\mathbf{SO}(2)}$ Phase

The $\mathbf{B}_{\mathbf{SO}(2)}$ phase is a non-ESP phase with a reduced and anisotropic spin susceptibility below T_c . The $\mathbf{B}_{\mathbf{SO}(2)}$ phase also exhibits tipping angle dependence of the frequency shift similar to that of ${}^3\text{He-B}$. In particular, for $\vec{H} \perp \hat{z}$ the shift is a polar-distorted Brinkman-Smith mode[17], and for $\vec{H} \parallel \hat{z}$ we find the “perpendicular” mode[27] that is qualitatively similar, but with important quantitative differences compared to bulk ${}^3\text{He-B}$.

For $\vec{H} \parallel \hat{z}$, the Zeeman energy is minimized in equilibrium by a spin-rotation $\mathbf{R}_{\hat{n}}(\pi/2)$, where \hat{n} is in the $x - y$ plane. This rotation leads to a positive transverse frequency shift that is maximal at small tipping angles, unlike the Brinkman-Smith mode. The quantitative description of the frequency shift depends on the spatial averages of the

$\text{BSO}(2)$ gap parameters,

$$\begin{aligned}
 P &= \langle \Delta_r \Delta_z \rangle + \langle \Delta_\phi \Delta_z \rangle \\
 Q &= \langle \Delta_r^2 \rangle + 2 \langle \Delta_r \Delta_\phi \rangle + \langle \Delta_\phi^2 \rangle \\
 R &= \langle \Delta_r^2 \rangle + \langle \Delta_\phi^2 \rangle + 4 \langle \Delta_z^2 \rangle ,
 \end{aligned}
 \tag{5.38}$$

with the resulting transverse shift for $\vec{H} \parallel \hat{z}$ given by

$$\begin{aligned}
 \omega \Delta \omega^{(\parallel)} &= \frac{1}{8} \frac{\gamma^2}{\chi_B} g_D \{ 4R \cos \beta + 4P (1 + 4 \cos \beta) \cos \vartheta \\
 &\quad - Q (1 + \cos \beta) \cos 2\vartheta \} ,
 \end{aligned}
 \tag{5.39}$$

where the Leggett angle is

$$\cos \vartheta = \begin{cases} +1 & : \beta \leq \beta'_L , \\ \frac{2P(2 \cos \beta - 1)}{Q(1 + \cos \beta)} & : \beta'_L < \beta < \beta_L , \\ -1 & : \beta \geq \beta_L , \end{cases}
 \tag{5.40}$$

with $\cos \beta'_L = (2P + Q)/(4P - Q)$ and $\cos \beta_L \equiv (2P - Q)/(4P + Q)$. Note that χ_B entering both Eqs. 5.39 and 5.42 is given by $\chi_B = \chi_N/[1 + g_z/\chi_N(\langle \Delta_r^2 \rangle + \langle \Delta_\phi^2 \rangle)] < \chi_N$. This result is obtained in both cases by minimizing the Zeeman energy for the specific field orientation. The left panel of Fig. 5.15 shows the tipping-angle dependence of the frequency shift $\Delta \omega^{(\parallel)}$ for temperatures starting just below the transition to $\text{BSO}(2)\text{-AC}_2$ phase boundary at $p = 10$ bar. At this pressure transition from the P_z phase to the $\text{BSO}(2)$ phase is interrupted by a narrow sliver of AC_2 phase. Thus, near the $\text{BSO}(2)\text{-AC}_2$ phase boundary, the P_z order parameter is dominant and that is reflected in the tipping angle

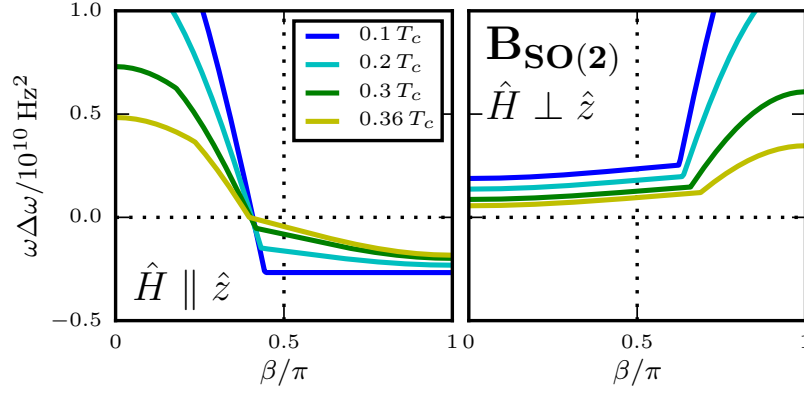


Figure 5.15. Transverse frequency shifts for the $\text{B}_{\text{SO}(2)}$ phase at $p = 10$ bar, temperatures $T = 0.1 T_c$, $0.2 T_c$, $0.3 T_c$, $0.36 T_c$, and maximal pair-breaking, $b'_T = 0$.

dependence for $T = 0.36 T_c$. At lower temperatures the transverse components of the $\text{B}_{\text{SO}(2)}$ become significant and the transverse shift evolves towards a form characteristic of the B-phase with a sharp transition at β_L . The polar distortion is still manifest as the negative shift for $\beta > \beta_L$.

For the static NMR field $\vec{H} \perp \hat{z}$ the relevant averages of the $\text{B}_{\text{SO}(2)}$ gap are

$$\begin{aligned}
 P &= \langle \Delta_r^2 \rangle + \langle \Delta_\phi^2 \rangle + 2 \langle \Delta_r \Delta_\phi \rangle + 2 \langle \Delta_r \Delta_z \rangle + 2 \langle \Delta_\phi \Delta_z \rangle \\
 Q &= 3 \langle \Delta_r^2 \rangle + 3 \langle \Delta_\phi^2 \rangle + 2 \langle \Delta_r \Delta_\phi \rangle \\
 &\quad + 8 \langle \Delta_r \Delta_z \rangle + 8 \langle \Delta_\phi \Delta_z \rangle + 8 \langle \Delta_z^2 \rangle \\
 (5.41) \quad R &= 11 \langle \Delta_r^2 \rangle + 11 \langle \Delta_\phi^2 \rangle + 18 \langle \Delta_r \Delta_\phi \rangle + 8 \langle \Delta_z^2 \rangle,
 \end{aligned}$$

leading to a transverse shift

$$(5.42) \quad \omega \Delta \omega^{(\perp)} = -\frac{1}{16} \frac{\gamma^2}{\chi_B} g_D \{2R \cos \beta + 4P (1 + 4 \cos \beta) \cos \vartheta + Q (1 + \cos \beta) \cos 2\vartheta\} ,$$

where

$$(5.43) \quad \cos \vartheta = \begin{cases} \frac{-2P(2 \cos \beta - 1)}{Q(1 + \cos \beta)} & : \beta < \beta_L. \\ 1 & : \beta \geq \beta_L. \end{cases}$$

and $\cos \beta_L = (2P - Q)/(4P + Q)$. Unlike bulk $^3\text{He-B}$, the confinement induced anisotropy of the $\mathbb{B}_{\text{SO}(2)}$ order parameter results in a nonzero transverse frequency shift even at small tipping angles, and a temperature dependent critical angle β_L . Once again the frequency shift shows the evolution from a functional form close to the P_z phase for $T = 0.36T_c$ towards the polar distorted B-phase at low temperature.

5.7. Summary and Outlook

For ^3He in a long cylindrical pore of radius $R = 100$ nm, the relative stability of superfluid phases is strongly dependent on pressure both through the combination of strong-coupling corrections to the fourth-order GL free energy and changes in the effective confinement ratio $R/\xi_0(p)$, and the degree of pairbreaking by boundary scattering. We find four different equilibrium phases over the full pressure range for boundary conditions spanning the range from maximal pairbreaking (retro-reflective boundaries) to minimal pairbreaking (specular reflective boundaries). The first instability is to the z -aligned polar P_z phase, except for the idealized case of perfect specular reflection for a perfectly circular pore. A polar distorted B-like phase is stabilized at sufficiently low temperatures

within our theory for the strong-coupling effects based on the GL functional. We find two symmetry inequivalent chiral A-like phases, the axially symmetric $A_{\text{SO}(2)}$ phase with a radially directed chiral field and a polar core favored in the limit of weak pairbreaking, and the broken axial symmetry chiral A_{C_2} phase with chirality directed perpendicular to the axis of the pore. The $A_{\text{SO}(2)}$ phase dominates the phase diagram for specularly reflecting boundaries while the A_{C_2} phase appears at intermediate temperatures and higher pressures separating the P_z and $B_{\text{SO}(2)}$ phases. The four equilibrium phases can be identified by their distinct NMR frequency shifts as functions of tipping angle and NMR field orientation. NMR experiments utilizing arrays of equivalent nano-pores should be able to test these predictions and uniquely identify the polar phase as well as the new prediction of the broken symmetry chiral A_{C_2} phase.

The interplay of complex symmetry breaking, spatial confinement, surface disorder and strong-interactions beyond weak-coupling BCS leads to a remarkably rich phase diagram of broken symmetry states in what is perhaps the simplest of confining geometries, the cylindrical pore. We expect an even wider spectrum of broken symmetry phases with unique physical properties in more complex confining geometries,[**103**] or when confinement is in competition with external fields or the formation of topological defects.[**96, 99**] Indeed theoretical reports of new phases of superfluid ^3He in thin films and cavities have simulated the development of nano-scale cavities, MEMS and nano-fluidic oscillators and new nano-scale materials for experimental search and discovery of new quantum ground states. In the latter category the infusion of quantum fluids into highly porous anisotropic aerogels has opened a new window into the role of confinement on complex symmetry

breaking. New chiral and ESP phases of superfluid ^3He in uniaxially stretched and compressed silica aerogels have been reported,[**15, 71, 78**] and in a new class of nano-scale confining media, called “nematic” aerogels, there is strong evidence to support the observation of a polar P_z phase of ^3He in this strongly anisotropic *random* medium.[**11, 29**] From the vantage point of our predictions for ^3He confined in a long cylindrical pore there are strong similarities between the phase diagram for $R = 100$ nm cylindrical pores and the experimental phase diagram of ^3He in nematic aerogels, including the normal to P_z transition, and uniaxially deformed B-like and chiral A-like phases. ² It is remarkable that the subtle correlations giving rise to chirality of an A_{C_2} or $A_{SO(2)}$ phase survives the random potential of these disordered porous solids. The observations pose challenges for theorists to provide a quantitative understanding of how complex symmetry breaking and long-range order remain so robust in random anisotropic materials.

²In Chapter 4 we describe a model of nafen aerogels that exhibits analogous phases.

5.8. Material Parameters

The following tables summarize the pressure dependent material parameters that determine the superfluid phases in strong-coupling GL theory.

p [bar]	T_c [mK]	v_f [m/s]	ξ_0 [nm]	$\Delta\beta_1^{\text{sc}}$	$\Delta\beta_2^{\text{sc}}$	$\Delta\beta_3^{\text{sc}}$	$\Delta\beta_4^{\text{sc}}$	$\Delta\beta_5^{\text{sc}}$
0.0	0.929	59.03	77.21	0.03	-0.11	0.10	-0.15	0.16
2.0	1.181	55.41	57.04	0.03	-0.04	-0.14	-0.37	0.19
4.0	1.388	52.36	45.85	0.02	-0.01	-0.24	-0.48	0.19
6.0	1.560	49.77	38.77	0.02	-0.01	-0.28	-0.54	0.18
8.0	1.705	47.56	33.91	0.02	-0.02	-0.30	-0.58	0.17
10.0	1.828	45.66	30.37	0.01	-0.03	-0.31	-0.60	0.15
12.0	1.934	44.00	27.66	0.01	-0.04	-0.31	-0.61	0.13
14.0	2.026	42.51	25.51	0.00	-0.05	-0.30	-0.62	0.11
16.0	2.106	41.17	23.76	0.00	-0.05	-0.27	-0.66	0.10
18.0	2.177	39.92	22.29	0.00	-0.06	-0.27	-0.68	0.09
20.0	2.239	38.74	21.03	-0.01	-0.06	-0.26	-0.69	0.07
22.0	2.293	37.61	19.94	-0.01	-0.07	-0.26	-0.71	0.06
24.0	2.339	36.53	18.99	-0.01	-0.07	-0.26	-0.72	0.04
26.0	2.378	35.50	18.15	-0.02	-0.07	-0.27	-0.73	0.03
28.0	2.411	34.53	17.41	-0.02	-0.07	-0.27	-0.74	0.01
30.0	2.438	33.63	16.77	-0.02	-0.07	-0.28	-0.74	-0.01
32.0	2.463	32.85	16.22	-0.03	-0.07	-0.27	-0.75	-0.02
34.0	2.486	32.23	15.76	-0.03	-0.07	-0.27	-0.75	-0.03

Table 5.1. Material parameters for ^3He vs. pressure, with T_c from Ref. [39], v_f calculated with m^* from Ref. [39] and density n from Ref. [101]. Coherence lengths are calculated as $\xi_0 = \hbar v_f / 2\pi k_B T_c$. Strong-coupling $\Delta\beta_i^{\text{sc}}$ parameters at T_c in units of $|\beta_1^{\text{wc}}|$ are from Ref. [23].

n	$\Delta\beta_1^{\text{sc}}$	$\Delta\beta_2^{\text{sc}}$	$\Delta\beta_3^{\text{sc}}$	$\Delta\beta_4^{\text{sc}}$	$\Delta\beta_5^{\text{sc}}$
0	3.070×10^{-2}	-1.074×10^{-1}	1.038×10^{-1}	-1.593×10^{-1}	1.610×10^{-1}
1	-2.081×10^{-3}	5.412×10^{-2}	-1.752×10^{-1}	-1.350×10^{-1}	2.263×10^{-2}
2	2.133×10^{-5}	-1.081×10^{-2}	3.488×10^{-2}	1.815×10^{-2}	-4.921×10^{-3}
3	-4.189×10^{-7}	1.025×10^{-3}	-4.243×10^{-3}	-1.339×10^{-3}	3.810×10^{-4}
4	—	-5.526×10^{-5}	3.316×10^{-4}	5.316×10^{-5}	-1.529×10^{-5}
5	—	1.722×10^{-6}	-1.623×10^{-5}	-1.073×10^{-6}	3.071×10^{-7}
6	—	-2.876×10^{-8}	4.755×10^{-7}	8.636×10^{-9}	-2.438×10^{-9}
7	—	1.991×10^{-10}	-7.587×10^{-9}	—	—
8	—	—	5.063×10^{-11}	—	—

Table 5.2. Coefficients of a polynomial fit to the strong-coupling β parameters from Ref. [23] of the form $\Delta\beta_i^{\text{sc}} = \sum_n a_n^{(i)} p^n$.

$p[\text{bar}]$	$\Delta\beta_1^{\text{sc}}$	$\Delta\beta_2^{\text{sc}}$	$\Delta\beta_3^{\text{sc}}$	$\Delta\beta_4^{\text{sc}}$	$\Delta\beta_5^{\text{sc}}$
0	-0.008	-0.033	-0.043	-0.054	-0.055
12	-0.034	-0.080	-0.117	-0.199	-0.194
16	-0.041	-0.088	-0.129	-0.230	-0.236
20	-0.048	-0.095	-0.136	-0.254	-0.277
24	-0.055	-0.101	-0.140	-0.272	-0.320
26	-0.059	-0.103	-0.140	-0.280	-0.344
28	-0.062	-0.105	-0.139	-0.287	-0.370
30	-0.066	-0.106	-0.137	-0.292	-0.398
32	-0.070	-0.106	-0.132	-0.296	-0.429
34.4	-0.074	-0.103	-0.123	-0.298	-0.469

Table 5.3. Sauls-Serene $\Delta\beta_i^{\text{sc}}$ parameters[81] for ${}^3\text{He}$ vs. pressure. The values at $p = 0$ bar were obtained by extrapolating the published $\Delta\beta_i^{\text{sc}}$, which were calculated only down to 12 bar, to their weak-coupling values at $\lim_{p \rightarrow p_0} T_c(p)/T_F(p) = 0$, which corresponds to a negative pressure of $p_0 = -5$ bar.

n	$\Delta\beta_1^{\text{sc}}$	$\Delta\beta_2^{\text{sc}}$	$\Delta\beta_3^{\text{sc}}$	$\Delta\beta_4^{\text{sc}}$	$\Delta\beta_5^{\text{sc}}$
0	-8.311×10^{-3}	-3.334×10^{-2}	-4.298×10^{-2}	-5.416×10^{-2}	-5.505×10^{-2}
1	-2.404×10^{-3}	-4.716×10^{-3}	-7.988×10^{-3}	-1.550×10^{-2}	-1.427×10^{-2}
2	2.813×10^{-5}	8.032×10^{-5}	1.637×10^{-4}	3.174×10^{-4}	2.942×10^{-4}
3	-4.024×10^{-7}	-9.400×10^{-8}	-1.345×10^{-8}	-2.138×10^{-6}	-6.654×10^{-6}

Table 5.4. Coefficients of a polynomial fit to the Sauls-Serene β parameters in Table 5.3 of the form $\Delta\beta_i^{\text{sc}} = \sum_n a_n^{(i)} p^n$.

5.9. Acknowledgements

The research of JJW and JAS was supported by the National Science Foundation (Grant DMR-1106315). We acknowledge key discussions with Erkki Thuneberg and Anton

Vorontsov on boundary conditions for the GL theory of ^3He in confined geometries, and with Bill Halperin and Andrew Zimmerman on experimental realizations of superfluidity with strong confinement that provided important motivation for this study.

CHAPTER 6

**Publication: Spontaneous Helical Order of a Chiral p -wave
Superfluid Confined in Nanoscale Channels**

6.1. Abstract

Strong interactions that favor chiral p -wave pairing, combined with strong pair breaking by confining boundaries, are shown to lead to new equilibrium states with different broken symmetries. Based on a strong-coupling extension of the Ginzburg-Landau (GL) theory that accurately accounts for the thermodynamics and phase diagram of the bulk phases of superfluid ^3He , we predict new phases of superfluid ^3He for confined geometries that spontaneously break rotational and translational symmetry in combination with parity and time-reversal symmetry.¹ One of the newly predicted phases exhibits a unique combination of chiral and helical order that is energetically stable in cylindrical channels of radius approaching the Cooper pair coherence length, e.g. $R \sim 100$ nm. Precise numerical minimization of the free energy yields a broad region of stability of the helical phase as a function of pressure and temperature, in addition to three translationally invariant phases with distinct broken spin- and orbital rotation symmetries. The helical phase is stable at both high and low pressures and favored by boundaries with strong pair-breaking. We present calculations of transverse NMR frequency shifts as functions of

¹This chapter extends Chapter 5 to include phases that spontaneously break translational symmetry along the axis of the cylindrical channel.

rf pulse tipping angle, magnetic field orientation, and temperature as signatures of these broken symmetry phases.

6.2. Introduction

The superfluid phases of ^3He are paradigms for spontaneous symmetry breaking in condensed matter and quantum field theory [95, 79]. The bulk A- and B phases are BCS condensates of p-wave, spin-triplet Cooper pairs [49]. The broken symmetries of these phases, which are well established, underpin the non-trivial topologies of both ground states [94, 61]. However, the bulk phases are only *two realizations* of the 18-dimensional manifold of spin-triplet, p-wave condensates. When ^3He is subjected to a confining potential on scales approaching the Cooper pair coherence length, $\xi_0 \approx 160 - 770 \text{ \AA}$ depending on pressure, new ground states with novel broken symmetries are stabilized [14, 99, 104, 105].

In this Letter we report theoretical predictions of the equilibrium phases of superfluid ^3He when confined in quasi-one-dimensional channels with radial confinement ranging from $R = 2 - 20 \xi_0(p)$. Among these phases is a novel “helical” phase of ^3He that spontaneously breaks both time-reversal and translational symmetry along the channel. The broken translational symmetry is realized as a *double helix* of disclination lines of the chiral axis confined on the boundary of the cylinder walls. The double-helix phase is predicted to be stable over a large region of the pressure-temperature phase diagram for channels with radius $R = 100 \text{ nm}$.

6.3. Ginzburg-Landau Theory

Our results are based on a strong-coupling extension of Ginzburg-Landau (GL) theory that accurately reproduces the relative stability for the bulk A- and B-phases, including the A-B phase transition [104]. The GL theory is formulated as a functional of the order parameter, the condensate amplitude for Cooper pairs, $\langle \psi_\sigma(\mathbf{p})\psi_{\sigma'}(-\mathbf{p}) \rangle$ in the spin-momentum basis. For spin-triplet, p-wave Cooper pairs the order parameter can be expressed in terms of a 3×3 matrix $A_{\alpha i}$ of complex amplitudes that transforms as the vector representation of $\text{SO}(3)_\text{S}$ with respect to the spin index α , and as the vector representation of $\text{SO}(3)_\text{L}$ with respect to the orbital momentum index i . In cylindrical coordinates the order parameter matrix may be represented as

$$(6.1) \quad A = \begin{pmatrix} A_{rr} & A_{r\phi} & A_{rz} \\ A_{\phi r} & A_{\phi\phi} & A_{\phi z} \\ A_{zr} & A_{z\phi} & A_{zz} \end{pmatrix},$$

where we choose aligned spin and orbital coordinate axes. The GL free energy functional,

$$(6.2) \quad \Omega[A] = \int_V d^3r (f_{\text{bulk}}[A] + f_{\text{grad}}[A]),$$

is expressed in terms of a bulk free energy density [91],

$$(6.3) \quad \begin{aligned} f_{\text{bulk}}[A] = & \alpha(T) \text{Tr} (AA^\dagger) + \beta_1 |\text{Tr}(AA^T)|^2 \\ & + \beta_2 [\text{Tr}(AA^\dagger)]^2 + \beta_3 \text{Tr} [AA^T(AA^T)^*] \\ & + \beta_4 \text{Tr} [(AA^\dagger)^2] + \beta_5 \text{Tr} [AA^\dagger(AA^\dagger)^*], \end{aligned}$$

and the gradient energies,

$$(6.4) \quad f_{\text{grad}}[A] = K_1 A_{\alpha j, k}^* A_{\alpha j, k} + K_2 A_{\alpha j, j}^* A_{\alpha k, k} + K_3 A_{\alpha j, k}^* A_{\alpha k, j},$$

where A^\dagger (A^T) is the adjoint (transpose) of A , $A_{\alpha i, j} = \partial_j A_{\alpha i}$, and the transformation of the gradient free energy from the Cartesian representation to cylindrical coordinates given in Eq. (6) of Ref. [104]. The material parameters, α , $\{\beta_i | i = 1 \dots 5\}$, and $\{K_a | a = 1, 2, 3\}$ multiplying the invariants defining the GL functional are determined by the microscopic pairing theory for ^3He . In weak-coupling theory these parameters are given in Refs. [91, 104].

Ginzburg-Landau theory is widely used in studying inhomogeneous superconducting phases, notably vortex states in type II superconductors [2], as well as Fulde-Ferrell-Larkin-Ovchinnikov states at high field and low temperatures [4]. In the case of ^3He a strong-coupling extension of the weak-coupling GL theory that accounts for the relative stability of the bulk A- and B phases, and specifically the A-B transition line, $T_{\text{AB}}(p)$ for pressures above the polycritical point, $p \gtrsim p_c$ was introduced in Ref. [104]. The strong-coupling functional is defined by the corrections to the fourth-order weak-coupling material parameters,

$$(6.5) \quad \beta_i(p, T) = \beta_i^{\text{wc}}(p, T_c(p)) + \frac{T}{T_c} \Delta\beta_i^{\text{sc}}(p),$$

with $\Delta\beta_i^{\text{sc}}(p) = \beta_i(p, T_c(p)) - \beta_i^{\text{wc}}(p, T_c(p))$. The weak-coupling parameters, $\beta_i^{\text{wc}}(p, T_c(p))$ are calculated from a Luttinger-Ward formulation of the weak-coupling microscopic free-energy functional and evaluated using the known pressure-dependent Fermi-liquid material parameters, provided in Table I of Ref. [104]. The $\Delta\beta_i^{\text{sc}}(p)$ have been obtained from

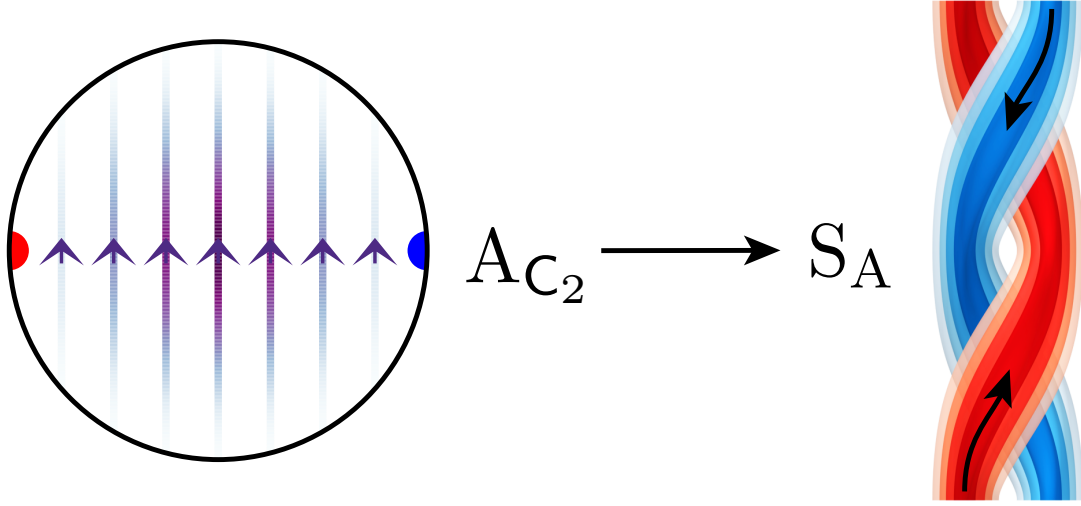


Figure 6.1. Left: The chiral axis $\hat{l}(\mathbf{r})$ for the A_{C_2} phase at $p = 26$ bar, $T = 0.7T_c$ with strong pairbreaking ($b'_T = 0.1$). The chiral axis is confined in the $r - \phi$ plane. The arrow color density is scaled by the amplitude, $(\Delta_r^2 + \Delta_\phi^2)^{1/2}$. The red and blue dots locate the two disgyrations, which support supercurrents propagating along $+z$ and $-z$, respectively. Right: Supercurrent isosurfaces in the S_A phase, calculated using the full order parameter in Eq. 6.13 of the Appendix.

analysis of measurements of the strong-coupling enhancement of heat capacity jumps, NMR frequency shifts and the Zeeman splitting of superfluid transition in a magnetic field [23]. The results we report are based on the strong-coupling parameters reported in Table I of Ref. [104]. We emphasize that the extended GL functional accounts for the relative stability of competing phases at temperatures well below $T_c(p)$, including the bulk A and B phases at high pressures [104], and the A to stripe phase transition in thin films of ^3He [105], and in the former case has been validated by our microscopic calculations of $T_{AB}(p)$ and the strong-coupling beta parameters, $\Delta\beta_i^{\text{sc}}(p)$, based on the formulation of the strong-coupling theory developed in Refs. [72, 81, 80, 86].

The geometry we consider here is an infinitely long cylindrical channel of radius R . For the channel walls we use boundary conditions that include a variable order parameter “slip length” b_T inspired by the analysis of Ambegaokar, de Gennes, and Rainer [5], as well as the influence of boundary curvature [20]. The resulting conditions at $r = R$ are [104],

$$(6.6) \quad \begin{aligned} A_{\alpha r}|_{r=R} = 0, \quad \frac{\partial A_{\alpha z}}{\partial r} \Big|_{r=R} &= -\frac{1}{b_T} A_{\alpha z}|_{r=R}, \\ \frac{\partial A_{\alpha\phi}}{\partial r} \Big|_{r=R} &= \left(\frac{1}{R} - \frac{1}{b_T} \right) A_{\alpha\phi}|_{r=R}. \end{aligned}$$

where the transverse extrapolation parameter $b'_T \equiv b_T/\xi_0$ varies between the $b'_T \rightarrow 0$ (maximal pairbreaking) and $b'_T \rightarrow \infty$ (minimal pairbreaking) limits.

The equilibrium order parameter is obtained by minimizing the GL free energy functional, i.e. by solving the Euler-Lagrange equations, $\delta\Omega[A]/\delta A^\dagger = 0$. When restricted to translationally invariant states we obtain four phases stable in different regions of the $p - T$ phase diagram: the P_z phase with Cooper pairs nematically aligned along the axis of the cylindrical channel is the first unstable mode from the normal state. At a lower temperature Cooper pairs with orbital wave functions transverse to z become unstable. Strong-coupling and strong pair breaking on the boundary lead to two distinct chiral phases with different symmetries. The first is a second-order transition from the P_z phase to the A_{C_2} phase with the chiral axis aligned in the plane perpendicular to the z axis. The A_{C_2} phase spontaneously breaks $SO(2)$ rotation symmetry. At lower temperatures the cylindrically isotropic chiral phase, $A_{SO(2)}$, is stabilized, and at even lower temperatures,

the polar-distorted $\text{B}_{\text{SO}(2)}$ phase is favored. Both $\text{A}_{\text{SO}(2)}$ and $\text{B}_{\text{SO}(2)}$ phases are separated by first-order transitions [104].

6.4. Dynamical Instability

The chiral A_{C_2} phase is an inhomogenous analog of bulk $^3\text{He-A}$, with a spatially averaged angular momentum (chiral) axis $\langle \hat{l} \rangle$ aligned along a fixed but arbitrary direction in the $r - \phi$ plane, as shown in Figure 6.1. For maximal pairbreaking boundary conditions the A_{C_2} order parameter is given by

$$(6.7) \quad A_{\alpha i} = \hat{d}_\alpha \cos\left(\frac{\pi r}{2R}\right) \left\{ \Delta'_z \hat{z}_i + i \Delta'_r (\cos(\phi - \vartheta) \hat{r}_i - \sin(\phi - \vartheta) \hat{\phi}_i) \right\}.$$

where $\vartheta + \pi/2$ is the angle of the average direction of the angular momentum axis, $\langle \vec{l} \rangle$ in the $r - \phi$ plane. The in-plane chiral axis spontaneously breaks the continuous $\text{SO}(2)$ rotational symmetry of the confining potential. The corresponding continuous degeneracy of the A_{C_2} phase implies the existence of a Nambu-Goldstone (NG) mode associated with massless, long-wavelength excitation of the orientation, ϑ , of $\langle \vec{l} \rangle$.

The dynamical equation for the NG mode is obtained from the action for the space-time fluctuations of the Cooper pairs relative to the A_{C_2} ground state, $\mathcal{A}_{\alpha i}(\mathbf{r}, t) = A_{\alpha i}(\mathbf{r}, t) - A_{\alpha i}^{\text{A}_{\text{C}_2}}(\mathbf{r})$,

$$(6.8) \quad \mathcal{S} = \int_V dt d^3r \left\{ \tau \text{Tr} \left(\dot{\mathcal{A}} \dot{\mathcal{A}}^\dagger \right) - \mathcal{U}[\mathcal{A}] \right\},$$

where $\mathcal{U}[\mathcal{A}]$ is the effective potential derived from an expansion of the free energy functional, $\Omega[\mathcal{A}]$, to quadratic order in the fluctuations, \mathcal{A} , of order parameter. The additional invariant represents the kinetic energy of the Cooper pair fluctuations, with the effective

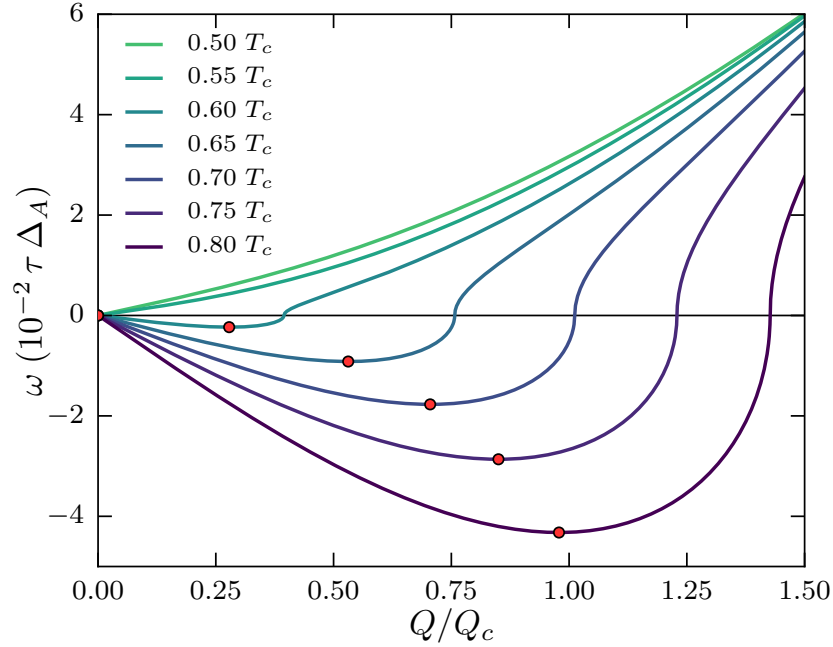


Figure 6.2. NG mode dispersion, ω_- , as a function of Q and T and scaled by the bulk A-phase amplitude at $p = 26$ bar and $R = 100$ nm. Negative values denote imaginary values of ω_- . The circles indicate the most unstable mode, Q/Q_c , for each temperature. $Q_c \approx \pi/674$ nm = 4.66×10^{-3} nm $^{-1}$ is the maximum value of the most unstable mode at the $S_{\mathbf{A}}\text{-}P_{\mathbf{z}}$ transition.

inertia given by $\tau = 7\zeta(3)N_f/48(\pi k_B T_c)^2$ in the weak-coupling BCS limit [60], where N_f is the normal-state density of states at the Fermi energy.

For the NG mode the action is a functional of the degeneracy variable corresponding to space-time fluctuations of the orientation of the chiral axis, $\vartheta(t, z)$, and the fluctuations of the polar component of the Cooper amplitude, $\delta_z''(t, z)$, that couples linearly to $\vartheta(t, z)$

through the gradient energy. The order parameter that incorporates these fluctuations is

$$\begin{aligned}
A_{\alpha i} = \hat{d}_\alpha \cos\left(\frac{\pi r}{2R}\right) & \left\{ i \Delta_r'' \cos[\phi - \vartheta(t, z)] \hat{r}_i \right. \\
& \left. - i \Delta_r'' \sin[\phi - \vartheta(t, z)] \hat{\phi}_i + \Delta_z' \hat{z}_i \right\} \\
(6.9) \quad & - i \delta_z''(t, z) \sin\left(\frac{\pi r}{R}\right) \sin[\phi - \vartheta(t, z)] \hat{d}_\alpha \hat{z}_i,
\end{aligned}$$

where Δ_r'' and Δ_z' take their equilibrium values found by minimizing the free energy functional with the order parameter in Eq. 6.7. Since the fluctuations depend only on time, t , and the coordinate, z , along the channel, we can integrate out the dependences on r and ϕ . We then express the action in Fourier space, in which case we obtain a sum over independent Fourier modes of the form, $\vartheta(t, z) = \vartheta \cos(\omega t + Qz)$ and $\delta_z''(t, z) = \delta_z'' \sin(\omega t + Qz)$. The Euler-Lagrange equations reduce to eigenvalue equations for the coupled mode amplitudes,

$$\begin{aligned}
(6.10) \quad \omega^2 \vartheta &= c^2 Q^2 \vartheta + \frac{8(3\pi - 4)}{9(\pi^2 - 4)\Delta_r''} \left(\frac{\pi c}{R}\right) cQ \delta_z'' \\
\omega^2 \delta_z'' &= \frac{1}{\tau} \left\{ \alpha + \left(1 - \frac{16}{9\pi^2}\right) (\beta_{13} + \beta_{245})(\Delta_r''^2 + \Delta_z'^2) \right. \\
& \quad \left. + 3c^2 Q^2 + \left(\frac{\pi c}{R}\right)^2 \left[1 + \frac{2}{\pi^2} \text{Cin}(2\pi)\right] \right\} \delta_z'' \\
(6.11) \quad & + \frac{16(3\pi - 4)\Delta_r''}{9\pi^2} \left(\frac{\pi c}{R}\right) cQ \vartheta,
\end{aligned}$$

where $\text{Cin}(2\pi) = \int_0^{2\pi} du (1 - \cos u)/u$. The weak-coupling relation $K_1 = K_2 = K_3 \equiv K$ has been used, and we introduced the velocity, $c \equiv \sqrt{K/\tau} = v_f/\sqrt{5}$, where v_f is the Fermi velocity.

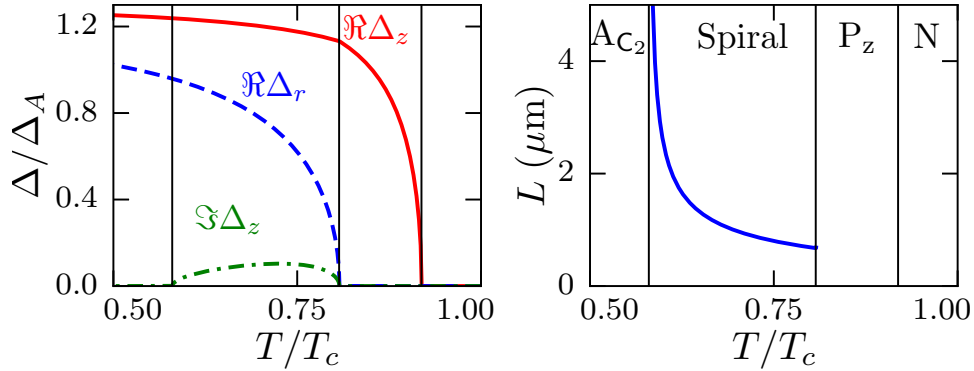


Figure 6.3. (Left) The amplitudes Δ'_z , (red); Δ''_r , (blue); and Δ''_z , (green) for the S_A order parameter phase, at $p = 26$ bar, $R = 100\text{nm}$ and scaled by the bulk A phase amplitude $\Delta_A = \sqrt{|\alpha(T)|/4\beta_{245}}$. The black vertical lines denote the continuous phase transitions A_{C_2} - S_A , S_A - P_z , and P_z -Normal with increasing temperature. (Right) The temperature dependence of the half-period L .

There are two eigenmodes corresponding to bosonic excitations with dispersions $\omega_{\pm}(Q)$. The low frequency mode, $\omega_-(Q)$ is identified as the NG mode with an excitation that is a pure rotation by ϑ , with a linear dispersion $\omega_-(Q) \propto Q$ for $Q \rightarrow 0$. Indeed the A_{C_2} phase supports low-frequency bosonic excitations corresponding to oscillations of the chiral axis, as shown in Fig. 6.2 for $R = 100$ nm, $p = 26$ bar and $T/T_c = 0.5$. However, the mode softens as the temperature increases. Above a critical temperature of $T^* \approx 0.57T_c$ the stiffness supporting the NG mode vanishes, and a conjugate pair of imaginary eigenfrequencies appear signalling a helical instability of the A_{C_2} phase. Figure 6.2 shows the evolution from the dispersion relation from the region of a stable A_{C_2} phase indicated by positive frequencies. Negative values correspond to the magnitude of the imaginary frequencies of the unstable NG mode. The wavevector of the most unstable mode, $Q_c(T)$, is indicated at each temperature. As we show below the instability is stabilized to a new

chiral phase with spontaneously broken translation symmetry along z by nonlinear terms in the GL free energy.

6.5. Double Helix Phase

The structure of the broken translation symmetry of this new phase, designated as $S_{\mathbf{A}}$, is that of a *double helix*, easily visualized by the propagating rotation of the pair disgyrations as shown in Fig. 6.1. This phase has continuous *helical* symmetry under the set of rotations by $-\Theta$ about $\hat{\mathbf{z}}$, $R_z[-\Theta]$ combined with the translation along z a distance $+\Theta/Q$, $T_z[+\Theta/Q]$. Note also the helical flow of the counter-propagating supercurrents that are confined near the two disgyrations. The model for the order parameter in Eq. 6.9 allows us to study the temperature evolution of the equilibrium $S_{\mathbf{A}}$ phase, with rotary propagation $\vartheta(z) = Qz$, shown in Fig. 6.3. Note that half-period, $L = \pi/Q$, is a minimum at the $S_{\mathbf{A}}\text{-}P_{\mathbf{z}}$ transition, with $L \approx 37 \xi_0 \approx 674 \text{ nm}$ at $p = 26 \text{ bar}$, and diverges as the $S_{\mathbf{A}}\text{-}A_{\mathbf{C}_2}$ transition is approached. The structure of the $S_{\mathbf{A}}$ phase obtained from the variational model, as well as the second-order phase transitions between $A_{\mathbf{C}_2}\text{-}S_{\mathbf{A}}$ phases, and $S_{\mathbf{A}}\text{-}P_{\mathbf{z}}$ phase, agree closely with the numerical minimization of the full GL functional (see Appendix).

6.6. Phase Diagram

We find *six* distinct phases for cylindrical channels: the translationally invariant $P_{\mathbf{z}}$, $A_{\mathbf{SO}(2)}$, $A_{\mathbf{C}_2}$, and $B_{\mathbf{SO}(2)}$ phases reported in Ref. [104], the double helix $S_{\mathbf{A}}$ phase, and a periodic domain-wall B-phase, $s_{\mathbf{B}}$, predicted by Aoyama [9]. The $s_{\mathbf{B}}$ phase is defined by domain walls separating polar-distorted B-like phases along the z axis. We impose

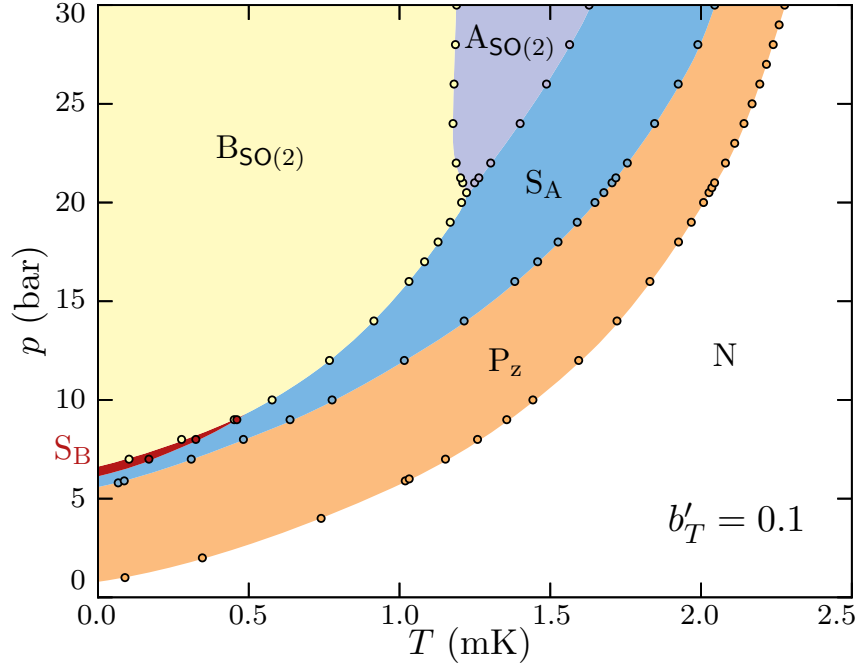


Figure 6.4. Phase diagram for the cylindrical channel with $R = 100\text{nm}$ and strong pairbreaking, $b'_T = 0.1$. The labels $S_{\mathbf{A}}$ and $s_{\mathbf{B}}$ correspond to the helical and B-like stripe phases, respectively. The $A_{\text{SO}(2)}$ phase appears at the highest pressures, and the A_{C_2} phase is suppressed by the more stable $S_{\mathbf{A}}$ phase. The $s_{\mathbf{B}}$ phase appears in a narrow region at low pressure and low temperature.

boundary conditions for the half-period, L , of the order parameter at $z = 0$ and $z = L$, where L is determined in the minimization of the free energy functional.

Figure 6.4 shows the phase diagram for a $R = 100\text{ nm}$ cylindrical channel with strong pairbreaking, $b'_T = 0.1$. The polar $P_{\mathbf{z}}$ phase, with Cooper pairs nematicallly oriented along the channel is the first superfluid phase to nucleate from the normal state. At a lower temperature the transverse orbital components appear; the chiral $S_{\mathbf{A}}$ phase develops at second-order instability from the $P_{\mathbf{z}}$ phase. Compared to an earlier calculation [104] that assumed translational invariance along the channel, we find that the A_{C_2} phase is replaced by the more stable $S_{\mathbf{A}}$ phase. At the higher pressures, the isotropic chiral A

phase is favored over the helical phase, separated by a first-order transition line, which then terminates at a tricritical point, below which the helical phase is unstable to the polar-distorted B phase, $\text{B}_{\text{SO}(2)}$, also separated by a first-order transition. At still lower pressures the s_{B} phase is stable in a very small window of the phase diagram. The $\text{A}_{\text{SO}(2)}$ and s_{B} phases are very sensitive to surface pair-breaking, and are completely suppressed for maximal pairbreaking (see Appendix). Finally, as the surface boundary condition approaches specular reflection the A_{C_2} and S_{A} phases are supplanted by the $\text{A}_{\text{SO}(2)}$ phase. A more detailed presentation of the phase diagram, including a phase diagram as a function of channel radius R , is presented in the Appendix.

6.7. NMR Signatures

Nuclear magnetic resonance (NMR) spectroscopy is a tool for identifying inhomogeneous phases of superfluid ^3He [28]. The frequency shift of the NMR line relative to the Larmor frequency is sensitive to the spin and orbital correlations of the order parameter that minimizes the nuclear magnetic dipole energy, $\Delta\Omega_D = \int_V d^3r g_D (|\text{Tr}A|^2 + \text{Tr}AA^*)$. The dipole energy lifts the degeneracy of the equilibrium states with respect to relative spin-orbit rotations. Thus, deviations from the minimum dipole energy configuration lead to dipolar torques generated by the spin-triplet Cooper pairs that shift the NMR resonance frequency away from the Larmor frequency. The magnitude of the shift is determined by the dipole coupling, $g_D = \frac{\chi_N}{2\gamma^2} \Omega_A^2 / \Delta_A^2$, which can be expressed in terms of normal-state spin susceptibility, χ_N , and the bulk A-phase longitudinal resonance frequency, Ω_A . We follow the analysis described in Ref. [104] for the transverse NMR frequency shifts of the translationally invariant phases of ^3He confined in nano-pores to calculate the frequency

shifts of the $S_{\mathbf{A}}$ phase. In particular, the spatially averaged dipole energy density for the $S_{\mathbf{A}}$ phase is $f_D = g_D \langle \Delta^2 \rangle_{S_{\mathbf{A}}} (\hat{d} \cdot \hat{z})^2$, with $\langle \Delta^2 \rangle_{S_{\mathbf{A}}} = 2 \langle \Delta_z^2 \rangle - \langle \Delta_\phi^2 \rangle - \langle \Delta_r^2 \rangle$ where $\langle \Delta_i^2 \rangle = \int_V d^3r \sum_\alpha |A_{\alpha i}|^2$ and \hat{d} lies in the plane of the channel and perpendicular to the static magnetic field axis \hat{H} . This results in a frequency shift of the same form as that of the $P_{\mathbf{z}}$ and $\Lambda_{\text{SO}(2)}$ phases [104], but with amplitude $\propto \langle \Delta^2 \rangle_{S_{\mathbf{A}}}$,

$$(6.12) \quad \omega \Delta\omega = \frac{\gamma^2}{\chi_N} g_D \langle \Delta^2 \rangle_{S_{\mathbf{A}}} \left[\cos \beta - \sin^2 \theta \left(\frac{5 \cos \beta - 1}{4} \right) \right],$$

where β is the pulsed NMR tipping angle and θ is the angle of the static field relative to the z axis. Figure 6.5 shows the frequency shift for $\beta \rightarrow 0$ as a function of temperature for the $S_{\mathbf{A}}$ variational order parameter defined in Eq. 6.9 and plotted in Fig. 6.3 for two field orientations. The second order transition at the $P_{\mathbf{z}}$ - $S_{\mathbf{A}}$ boundary shows a discontinuity in the slope of $\Delta\omega(T)$, and an apparent jump occurs at the $S_{\mathbf{A}}$ - Λ_{C_2} transition. In fact this is a smooth crossover confined to a narrow temperature range related to the divergence of the period of the $S_{\mathbf{A}}$ phase. The detailed NMR spectrum close to this transition is more complex because the spatial variations of the $S_{\mathbf{A}}$ phase, set by the half-period, L , can exceed the dipole coherence length, $\xi_D \equiv \sqrt{g_D/K_1} \approx 10 \mu\text{m}$ near to the $S_{\mathbf{A}}$ - Λ_{C_2} transition. The \hat{d} vector becomes inhomogeneous, spatial averaging breaks down and the NMR line will broaden as the temperature approaches the $S_{\mathbf{A}}$ - Λ_{C_2} transition in a narrow window indicated by the gray shading in Fig. 6.5. A narrow NMR line is restored in the Λ_{C_2} phase.

6.8. Conclusions and Beyond ^3He

We find six distinct equilibrium phases within highly confined cylindrical channels, including two phases that break translation symmetry along the channel. In particular,

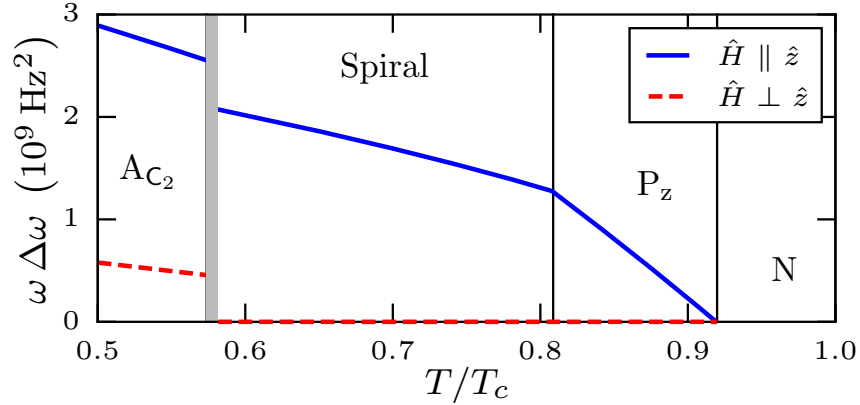


Figure 6.5. Small tipping angle ($\beta \approx 0$) transverse frequency shift for the $S_{\mathbf{A}}$ phase as a function of temperature. The $S_{\mathbf{A}}$ phase order parameter is that shown in Fig. 6.3. The $S_{\mathbf{A}}$ and P_z frequency shifts are found using Eq. 6.12, and the A_{C_2} frequency shifts are given by Eqs. 36 and 37 in Ref. [104]. The grey shaded region denotes the region of the $S_{\mathbf{A}}$ phase where the half-period L exceeds $\xi_D \approx 10 \mu\text{m}$.

we predict a “helical” phase, $S_{\mathbf{A}}$, which spontaneously breaks time-reversal symmetry and translational symmetry, but retains rotary-translation (helical) symmetry. The double-helix structure of this phase is predicted to be stable over a significant region of p-T phase diagram for long cylindrical pores of radius approaching the Cooper pair coherence length ξ_0 , and to show a distinct NMR signature.

The novel broken symmetry phases of ^3He are based on competing interactions in a strongly correlated Fermi liquid with unconventional pairing, combined with strong pair breaking by confining boundaries. This situation can arise in a broad range of unconventional superconductors, including chiral superconductors such as Sr_2RuO_4 and UPt_3 , as well as the cuprates. Indeed theoretical predictions of novel broken translational symmetry phases are reported for d-wave superconductors subject to strong confinement

[97, 43], and it seems likely that there are more novel broken symmetry phases in multi-component, unconventional superconductors awaiting discovery.

Acknowledgements — This research was supported by National Science Foundation Grant DMR-1508730. We thank Bill Halperin and Andrew Zimmerman for discussions on confined phases of ^3He that contributed to this research. We also thank Michael Moore for bringing Ref. [14] to our attention.

6.9. Appendix

Order Parameter for the Double Helix Phase — Numerical minimization of the GL functional to determine the exact structure of the $S_{\mathbf{A}}$ phase is made efficient, without loss of accuracy, by developing the ϕ -dependence as an expansion in symmetry-preserving harmonics,

$$\begin{aligned}
 A_{\alpha i} = \hat{d}_{\alpha} \sum_{j=0}^{\infty} \left\{ \right. & \Delta'_{r,j}(r) \sin[2j(\phi + Qz)] \hat{r}_i \\
 & + i \Delta''_{r,j}(r) \cos[(2j + 1)(\phi + Qz)] \hat{r}_i \\
 & + \Delta'_{\phi,j}(r) \cos[2j(\phi + Qz)] \hat{\phi}_i \\
 & + i \Delta''_{\phi,j}(r) \sin[(2j + 1)(\phi + Qz)] \hat{\phi}_i \\
 & + \Delta'_{z,j}(r) \cos[2j(\phi + Qz)] \hat{z}_i \\
 & \left. + i \Delta''_{z,j}(r) \sin[(2j + 1)(\phi + Qz)] \hat{z}_i \right\} .
 \end{aligned}
 \tag{6.13}$$

The numerical result for the $S_{\mathbf{A}}$ phase converges rapidly to the exact solution with the addition of higher harmonics.

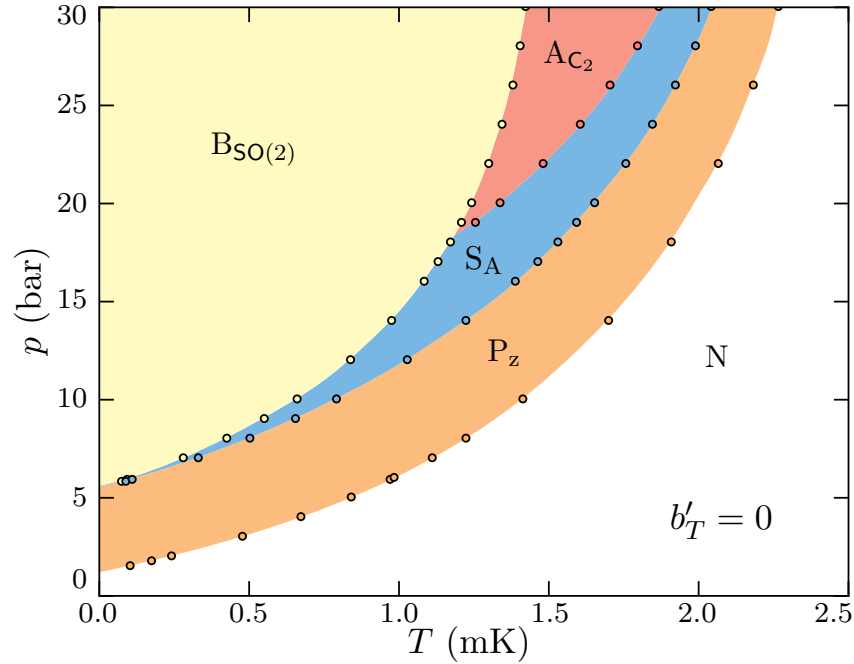


Figure 6.6. Phase diagram for the cylindrical channel with $R = 100\text{nm}$ and $b'_T = 0$ (maximal pairbreaking). The S_A phase has displaced much of the A_{C_2} phase compared to the phase diagram calculated for only z translationally invariant phases [104].

Sensitivity of the Phase Diagram to Strong Pairbreaking — The anisotropic chiral A_{C_2} and S_A phases are favored under conditions of strong pairbreaking on the boundary because the energy cost of the boundary half-disgrations is minimal due to suppression of all the order parameter components. By contrast the $A_{SO(2)}$ phase, which hosts a radial disgyration at the center of the cell is disfavored over both anisotropic chiral phases.

This is reflected in the phase diagram for maximal pairbreaking, $b'_T = 0$, shown in Fig. 6.6 for a $R = 100\text{ nm}$ cylindrical channel. Note that strong-coupling, which is relatively stronger at higher temperatures favors the helical phase over the translationally invariant A_{C_2} phase. Also note that s_B phase is not stable at this confinement ($R = 100\text{ nm}$) for maximal pair-breaking.

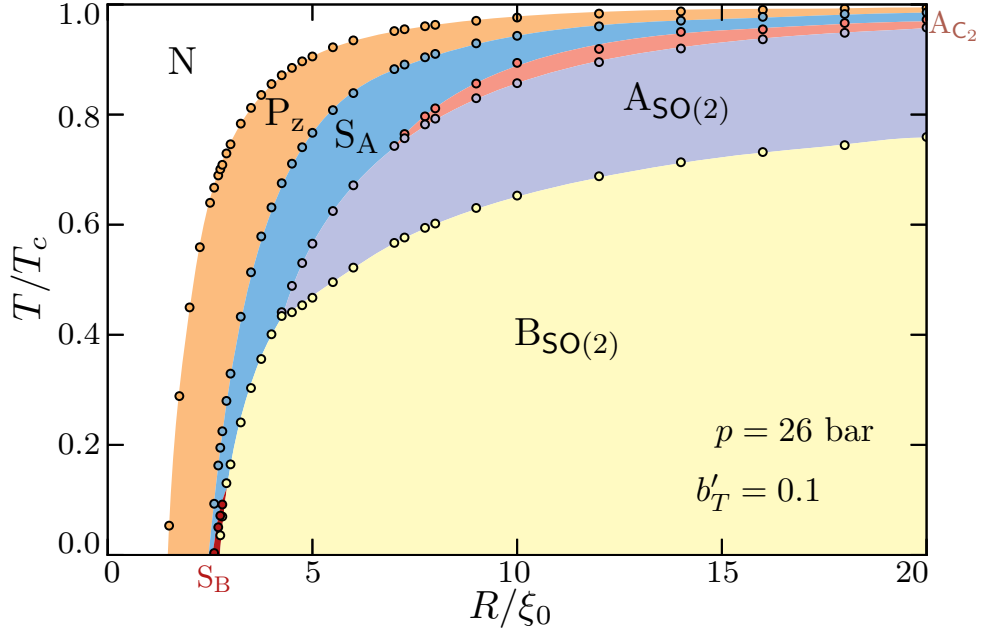


Figure 6.7. Phase diagram: temperature versus radius for cylindrical channel at $p = 26$ bar with strong pairbreaking. $b'_T = 0.1$. All six phases we have found are shown in this diagram, although the s_B phase is stable in a very narrow window of R and T .

We also include the phase diagram as a function of the channel radius R (Fig. 6.7) for $p = 26$ bar and $b'_T = 0.1$. The S_A phase is clearly favored by high confinement relative to the A_{C_2} , $A_{SO(2)}$, and $B_{SO(2)}$ phases. However, at this pressure the s_B phase is very fragile and stable only at very low temperatures where non-local corrections to the gradient energy, which are not included in the extended GL functional, are likely relevant. We also note that there is a critical radius above which the A_{C_2} phase appears.

CHAPTER 7

Publication: Strong-coupling and the Stripe phase of ^3He **7.1. Abstract**

Thin films of superfluid ^3He were predicted, based on weak-coupling BCS theory, to have a stable phase which spontaneously breaks translational symmetry in the plane of the film. This crystalline superfluid, or “stripe” phase, develops as a one dimensional periodic array of domain walls separating degenerate B phase domains. We report calculations of the phases and phase diagram for superfluid ^3He in thin films using a strong-coupling Ginzburg-Landau theory that accurately reproduces the bulk ^3He superfluid phase diagram. We find that the stability of the Stripe phase is diminished relative to the A phase, but the Stripe phase is stable in a large range of temperatures, pressures, confinement, and surface conditions.

7.2. Introduction

The theoretical prediction of a crystalline superfluid, or “stripe” phase, that spontaneously breaks translational symmetry in thin films of ^3He [99], along with advances in nanoscale fabrication and experimental instrumentation [50], has renewed interest in the properties of superfluid ^3He in thin films and confined geometries. In the weak-coupling limit of BCS theory the Stripe phase is predicted to be stable in a large region of temperature and pressure for films of thickness $D \sim 700$ nm. However, recent experiments on

^3He confined in slabs of thickness $D \approx 700$ nm and $D \approx 1080$ nm have failed to detect evidence of the Stripe phase [50].¹

A limitation of the Vorontsov and Sauls theory is that it does not include strong-coupling corrections to the BCS free energy. In bulk ^3He , weak-coupling theory predicts a stable B phase at all temperatures and pressures; however, the A phase is found to be stable experimentally at T_c and pressures above $p_{\text{PCP}} \approx 21.22$ bar, with a first-order transition at $T_{\text{AB}} < T_c$ to the B phase. Theoretically accounting for the stability of the A phase requires including next-to-leading order corrections to the full free energy functional, i.e. corrections to the weak-coupling functional [72]. While these strong-coupling corrections are largest at high pressures, they remain significant even for $p \sim 0$ bar[23]. Thus, for superfluid ^3He confined within a film, it is to be expected that strong-coupling effects will increase the stability of the A phase relative to both the B- and Stripe phases, which could diminish, or even eliminate, the experimentally accessible region of the Stripe phase.

In this paper we report our study of the A-Stripe and Stripe-B superfluid transitions using a Ginzburg-Landau (GL) functional that incorporates strong-coupling corrections to the weak-coupling GL material coefficients and accurately reproduces the bulk superfluid ^3He phase diagram [104]. Within this strong-coupling GL theory we calculate the superfluid order parameter and phase diagram as a function of pressure, temperature, confinement, and surface conditions.

¹Levitin et al[52] have recently reported evidence of spatial modulation in a 1080 nm slab.

7.3. Ginzburg-Landau Theory

The general form of the p-wave, spin triplet order parameter for ^3He is given by the mean-field pairing self energy, which can be expanded in the basis of symmetric Pauli matrices ($S = 1$) and vector basis of orbital momenta ($L = 1$),

$$(7.1) \quad \hat{\Delta}(\hat{p}) = \sum_{\alpha i} A_{\alpha i} (i\sigma_{\alpha}\sigma_y) \hat{p}_i,$$

where \hat{p} is the direction of relative momentum of the Cooper pairs defined on the Fermi surface, and $A_{\alpha i}$ are the elements of a 3×3 complex matrix,

$$(7.2) \quad A = \begin{pmatrix} A_{xx} & A_{xy} & A_{xz} \\ A_{yx} & A_{yy} & A_{yz} \\ A_{zx} & A_{zy} & A_{zz} \end{pmatrix},$$

that transforms as a vector under spin rotations (with respect to α) and (separately) as a vector under orbital rotations (with respect to i). We choose aligned spin and orbital coordinate axes.

7.3.1. Free energy functional

To determine the order parameter and the phase diagram of ^3He in a film geometry, we solve the Euler-Lagrange equations of the Ginzburg-Landau functional, subject to relevant boundary conditions, and calculate the order parameter and the stationary free energy. The GL functional is defined by bulk and gradient energies with temperature dependent

strong-coupling corrections, and is supplemented by boundary conditions that we can tune from maximal to minimal pair-breaking [104].

The Ginzburg-Landau free energy functional is expressed in terms of invariants constructed from the order parameter matrix, A , and is given by [91]

$$(7.3) \quad \Omega[A] = \int_V d\vec{R} \left\{ \alpha(T) \text{Tr} (AA^\dagger) + \beta_1 |\text{Tr}(AA^T)|^2 + \beta_2 [\text{Tr}(AA^\dagger)]^2 \right. \\ \left. + \beta_3 \text{Tr} [AA^T(AA^T)^*] + \beta_4 \text{Tr} [(AA^\dagger)^2] + \beta_5 \text{Tr} [AA^\dagger(AA^\dagger)^*] \right. \\ \left. + K_1 (\nabla_k A_{\alpha j} \nabla_k A_{\alpha j}^*) + K_2 (\nabla_j A_{\alpha j} \nabla_k A_{\alpha k}^*) + K_3 (\nabla_k A_{\alpha j} \nabla_j A_{\alpha k}^*) \right\} .$$

In the weak-coupling limit the GL material parameters are given by

$$(7.4) \quad \alpha^{\text{wc}}(T) = \frac{1}{3} N(0) (T/T_c - 1) ,$$

$$(7.5) \quad 2\beta_1^{\text{wc}} = -\beta_2^{\text{wc}} = -\beta_3^{\text{wc}} = -\beta_4^{\text{wc}} = \beta_5^{\text{wc}} ,$$

$$(7.6) \quad \beta_1^{\text{wc}} = -\frac{N(0)}{(\pi k_B T_c)^2} \left\{ \frac{1}{30} \left[\frac{7}{8} \zeta(3) \right] \right\} ,$$

$$(7.7) \quad K_1^{\text{wc}} = K_2^{\text{wc}} = K_3^{\text{wc}} = \frac{7\zeta(3)}{60} N(0) \xi_0^2 ,$$

and determined by the normal-state, single-spin density of states at the Fermi energy, $N(0)$, the bulk transition temperature, T_c , and the Fermi velocity, v_f . The Cooper pair correlation length $\xi_0 \equiv \hbar v_f / 2\pi k_B T_c$ varies from $\xi_0 \simeq 770 \text{ \AA}$ at $p = 0$ bar to $\xi_0 \simeq 160 \text{ \AA}$ at $p = 34$ bar.

7.3.2. Strong-coupling corrections

The fourth order β parameters that enter the GL free energy functional are modified by next-to-leading order corrections to the full Luttinger-Ward free energy functional [72]. These corrections scale as $\Delta\beta_i^{\text{sc}} \sim \beta_i^{\text{wc}}(T/T_F)$ near T_c . Combining the $\Delta\beta_i^{\text{sc}}$ with the weak-coupling coefficients in the bulk GL functional yields the critical pressure, p_{PCP} , above which the A phase is stable relative to the B phase. For $p > p_{\text{PCP}}$ the temperature scaling of the strong-coupling corrections relative to the weak-coupling β parameters breaks the degeneracy in temperature between the A and B phases at the critical pressure and accounts for the pressure dependence of the A-B transition line, $T_{\text{AB}}(p)$, and thus an accurate bulk phase diagram [104]. The resulting strong-coupling β parameters are given by

$$(7.8) \quad \beta_i(T, p) = \beta_i^{\text{wc}}(p, T_c(p)) + \frac{T}{T_c} \Delta\beta_i^{\text{sc}}(p).$$

Figure 7.1 shows the experimental bulk superfluid phase diagram as well as the phase diagram calculated from strong-coupling GL theory using $\Delta\beta_i^{\text{sc}}$ coefficients obtained based on analysis of selected experiments by Choi et al. [23]. These β coefficients differ substantially from those calculated from strong-coupling theory based on a quasiparticle scattering amplitude that accounts for the normal Fermi liquid properties of ^3He . Figure 7.2 shows the bulk phase diagram calculated using the $\Delta\beta_i^{\text{sc}}$ from Sauls & Serene[81]. This set of β coefficients has a higher polycritical pressure than experiment; however, the pressure dependence of the $\Delta\beta_i^{\text{sc}}$ represents the expectation based on strong-coupling

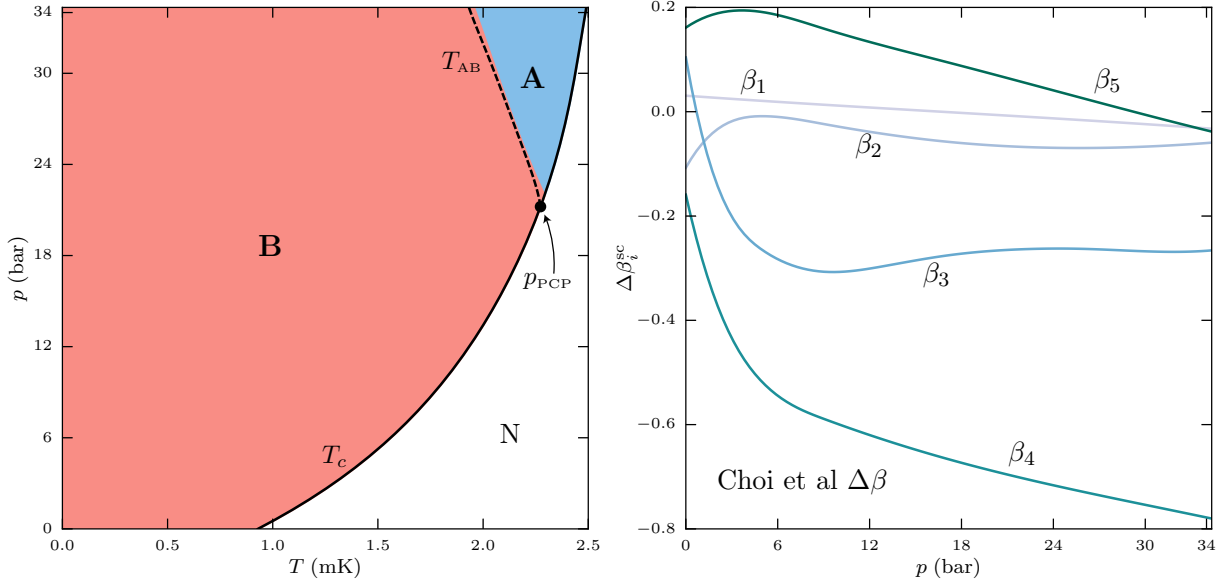


Figure 7.1. (Left) Bulk phase diagram with lines showing the measured phase transitions and shading showing the calculated regions of phase stability based on GL theory. The $\Delta\beta_i^{\text{sc}}$ coefficients are from Choi et al[23] and are plotted in the right panel.

theory dominated scattering from ferromagnetic spin-fluctuations. Below $p = 12$ bar the $\Delta\beta_i^{\text{sc}}$ are extrapolated to zero at a negative pressure corresponding to $T_c = 0$ [104].²

7.3.3. Boundary Conditions

Confinement is represented in the GL theory through boundary conditions. For infinite, planar surfaces there are two limiting cases: maximal pairbreaking, due to the retroreflection of quasiparticles[77], and minimal pairbreaking, corresponding to specular reflection [5]. For a surface on the $x - y$ plane with ^3He filling $z > 0$, maximal pairbreaking is

²In Chapter 8 we report an improved microscopic strong-coupling model that reproduces the bulk phase diagram along with its resulting GL parameters.

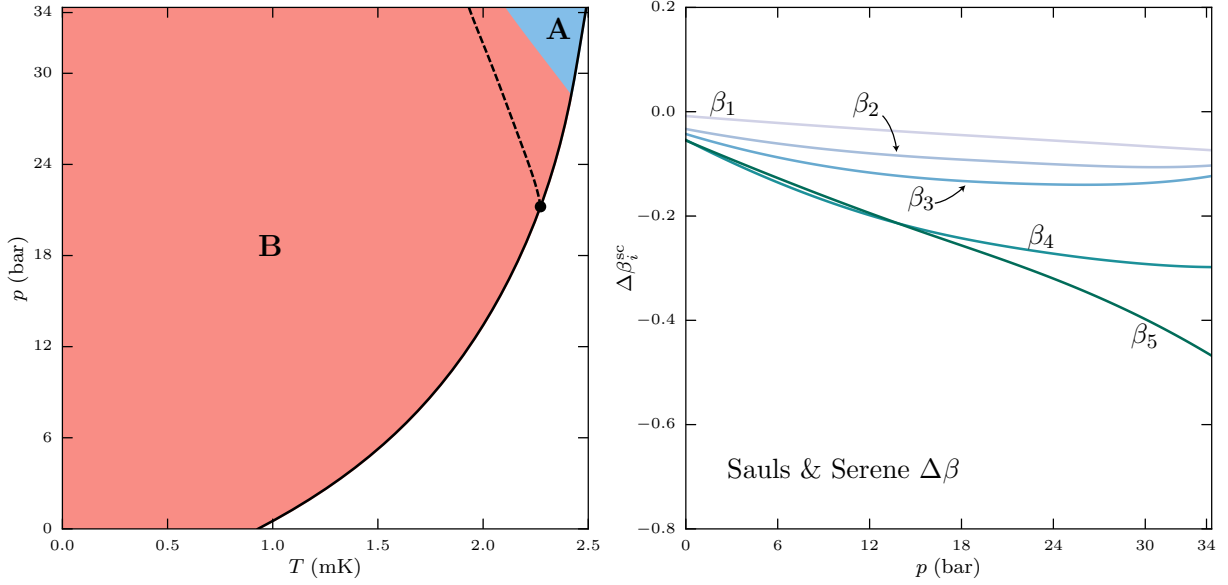


Figure 7.2. (Left) Bulk phase diagram where the shaded regions represents the phases calculated from GL theory with the $\Delta\beta_i^{\text{sc}}$ of Sauls & Serene [81]. These strong-coupling corrections are plotted in the right panel.

defined within GL theory by

$$(7.9) \quad A_{\alpha i}|_{z=0} = 0 \quad \forall i \in \{x, y, z\},$$

while minimal pairbreaking is defined by

$$(7.10) \quad \begin{aligned} A_{\alpha z}|_{z=0} &= 0, \\ \nabla_z A_{\alpha x}|_{z=0} &= \nabla_z A_{\alpha y}|_{z=0} = 0. \end{aligned}$$

These boundary conditions may be extended by interpolating between the two extremes. In particular, Ambegaokar, de Gennes, and Rainer (AdGR) showed that diffuse scattering from an atomically rough surface leads to a GL boundary condition in which

the transverse orbital components of the order parameter are finite at the surface, but extrapolate linearly to zero a distance $b_T = 0.54\xi_0$ past the boundary. Thus, we introduce more general boundary conditions defined by

$$(7.11) \quad \begin{aligned} A_{\alpha z}|_{z=0} &= 0, \\ \nabla_z A_{\alpha x}|_{z=0} &= \frac{1}{b_T} A_{\alpha x}|_{z=0} \\ \nabla_z A_{\alpha y}|_{z=0} &= \frac{1}{b_T} A_{\alpha y}|_{z=0}, \end{aligned}$$

where $b_T = b'_T \xi_0$ is the extrapolation length. The parameter b'_T is allowed to vary from $b'_T = 0$, maximal pairbreaking, to $b'_T \rightarrow \infty$, minimal pairbreaking. The film geometry consists of two infinite coplanar surfaces separated by a distance D with ${}^3\text{He}$ filling the region between them. The boundary conditions in Eq. 7.11 are imposed at $z = \pm D/2$.

7.3.4. Extrapolating GL theory to low temperatures

Ginzburg-Landau theory is only expected to be accurate in the vicinity of T_c . This is easily seen in the order parameter amplitude, $\Delta^2 \sim 1 - T/T_c$, which varies linearly in T down to $T = 0$; whereas the weak-coupling BCS order parameter saturates at low temperatures. In confined ${}^3\text{He}$, this difference is reflected in the characteristic length scale for variations of the order parameter, which in GL theory is

$$(7.12) \quad \xi_{GL}(T) = \left[\frac{7\zeta(3)/20}{1 - T/T_c} \right]^{1/2} \left(\frac{\hbar v_f}{2\pi k_B T_c} \right).$$

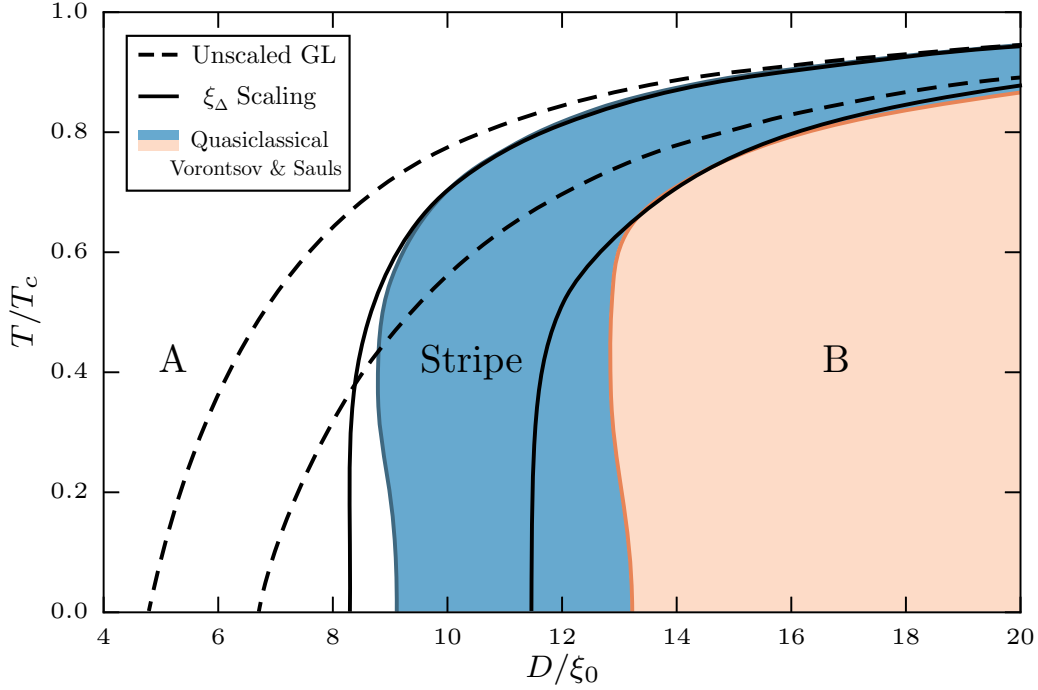


Figure 7.3. Comparison of the phase diagrams calculated within weak-coupling quasiclassical theory (blue and orange lines), weak-coupling GL theory (dashed lines), and weak-coupling GL theory with D rescaled by $\xi_{GL}(T)/\xi_\Delta(T)$ (solid black lines).

In weak-coupling BCS theory, the characteristic length scale is

$$(7.13) \quad \xi_\Delta(T) = \frac{\hbar v_f}{\sqrt{10\Delta_B^{\text{BCS}}(T)}},$$

which is significantly larger than $\xi_{GL}(T)$ at low temperatures. In order to more accurately extrapolate the spatial variations of the order parameter, as well as the confinement phase diagram, to lower temperatures we rescale the film of thickness in the GL equations $D \rightarrow D(T)$ with

$$(7.14) \quad D(T) = D(T_c) \frac{\xi_{GL}(T)}{\xi_\Delta(T)},$$

where $D(T_c) = D$ is the thickness of the film and $D(T)$ is a rescaled thickness used within the GL theory calculation. Figure 7.3 shows the effect of this rescaling on the weak-coupling GL theory phase diagram for the region of stability of the Stripe phase in comparison to the Stripe phase region obtained in weak-coupling quasiclassical theory [99]. Rescaling lengths in the GL theory in terms of $\xi_\Delta(T)$ gives a more accurate representation of the confinement phase diagram than simple extrapolation of the GL results to low temperature. The deviations that remain reflect the non-locality of the quasiclassical theory for inhomogeneous phases for $T \ll T_c$.

7.4. Stripe phase

The Stripe phase spontaneously breaks translational symmetry in the plane of the film. We assume it does so along the x axis, leaving the order parameter translationally invariant along the y direction. Broken translational symmetry leads to a new length scale, L , which is the half-period of the Stripe phase order parameter; L is an emergent length scale, which varies with temperature, pressure, film thickness, and the surface boundary condition, and must be determined by numerical minimization of the GL free energy in parallel with the self-consistent determination of the order parameter.

7.4.1. Order parameter

The Stripe phase is predicted to be stable in superfluid ^3He films of thickness $D \sim 10\xi_0$ [99]. In weak-coupling theory this phase appears as a second order transition between the Planar and B phases, and for $D \lesssim D_{c_2} \approx 13\xi_0$, corresponds to a periodic array of degenerate B-phase domains separated by domain walls [99].

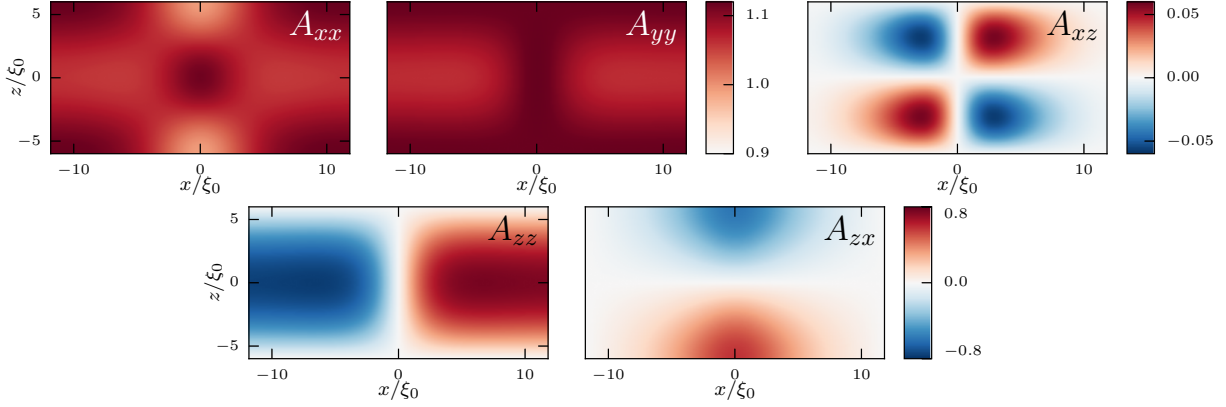


Figure 7.4. Stripe phase order parameter for specular surfaces as functions x and z for $D = 12\xi_0$, $p = 3$ bar, $T = 0.5T_c$, and calculated period $L \approx 23.6\xi_0$. The amplitudes are scaled in units of the bulk B phase order parameter, $\Delta_B = \sqrt{|\alpha(T)|/6(\beta_{12} + 1/3\beta_{345})}$.

For broken translational symmetry along the x axis the residual symmetry of the Stripe phase is defined by the point group,

$$\begin{aligned}
 \text{H} &= \{e, c_{2x}^L c_{2x}^S\} \times \{e, \pi_{xz}^L \pi_{xz}^S\} \times \{e, \pi_{xy}^L \pi_{xy}^S\} \\
 (7.15) \quad &\times \{e, \pi_{xz}^L \pi_{xz}^S\} \times \{e, e^{i\pi} c_{2z}^L\} \times \mathbb{T},
 \end{aligned}$$

where c_{2x}^L is an orbital space π rotation about the x axis, π_{xz}^S is a spin space reflection about the xz plane, and \mathbb{T} is the operation of time reversal. Based on this residual symmetry group we can simplify the form of the order parameter for the Stripe phase to

$$(7.16) \quad A(x, z) = \begin{pmatrix} A_{xx} & 0 & A_{xz} \\ 0 & A_{yy} & 0 \\ A_{zx} & 0 & A_{zz} \end{pmatrix},$$

where the remaining five components are functions of x and z , and are all real due to time reversal symmetry.

The spatial dependences of the self-consistent order parameter components for the Stripe phase at pressure $p = 3$ bar, $T/T_c = 0.5$, thickness $D = 12\xi_0$ with specular surfaces are shown in Fig. 7.4. Note that the calculated half period is $L \approx 23.6\xi_0$, and that the dominant components are the diagonal elements, A_{xx} , A_{yy} and A_{zz} . The latter exhibits a domain wall separating degenerate B-like order parameters with $\text{sgn}(A_{zz}) = \pm 1$. The pair-breaking of A_{zz} on the boundaries is alleviated by the large off-diagonal component, A_{zx} , at the junction with the domain wall. The remaining symmetry allowed amplitude, A_{xz} , clearly exhibits the symmetry with respect to $c_{2x}^L c_{2x}^S$, but is smaller by an order of magnitude.

The stability of the Stripe phase results from a tradeoff between the lowering of the energy at junctions where the surfaces intersect the domain wall (note the gradient energy in Fig. 7.5) and the cost in energy, away from the film surface, due to the suppression of the order parameter along the domain wall. The total condensation energy density, with separate bulk and gradient energy densities, is shown in Fig. 7.5.

7.4.2. Variational Model

The magnitude of the half-period of the Stripe phase, L , is most easily determined using a variational form of the order parameter; L is a minimum at the Stripe-Planar transition and diverges at the Stripe-B transition. At the Stripe-Planar transition, and for specular

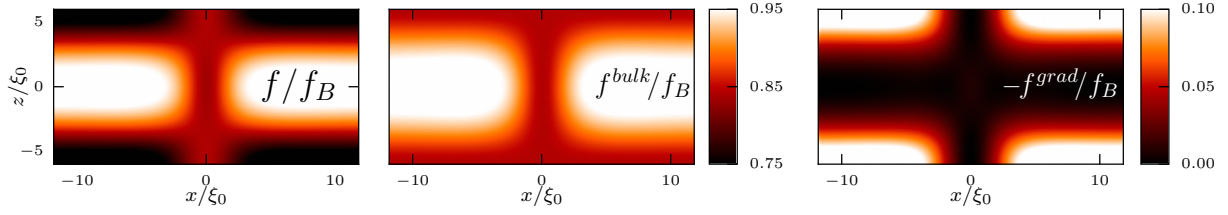


Figure 7.5. Energy density of the Stripe phase with specular surfaces for $D = 12\xi_0$, $p = 3$ bar, $T = 0.5T_c$, and calculated period $L \approx 23.6\xi_0$. The energy density f is scaled by the unconfined bulk energy density $f_B = \frac{1}{2}\alpha(T)\Delta_B(T)^2 < 0$, and is also shown separated into bulk and gradient contributions.

boundaries, L may be derived from the variational order parameter,

$$(7.17) \quad A(x, z) = \begin{pmatrix} \Delta_{xx} & 0 & 0 \\ 0 & \Delta_{yy} & 0 \\ A_{zx} & 0 & A_{zz} \end{pmatrix},$$

where $A_{zx} = -\Delta_{zx} \cos(\pi x/L) \sin(\pi z/D)$ and $A_{zz} = \Delta_{zz} \sin(\pi x/L) \cos(\pi z/D)$. At the Stripe-Planar transition we assume that

$$(7.18) \quad \Delta_{yy} = \Delta_{xx}, \quad \Delta_{zx} \ll \Delta_{xx}, \quad \text{and} \quad \Delta_{zz} \ll \Delta_{xx}.$$

After spatially averaging and dropping terms greater than second order in Δ_{zx} and Δ_{zz} the resulting GL functional reduces to,

$$(7.19) \quad F_{\text{var}} = 2\alpha\Delta_{xx}^2 + 4\beta_P\Delta_{xx}^4 - \frac{\pi^2 K_{23}\Delta_{zx}\Delta_{zz}}{2DL} \\ + \Delta_{zx}^2 \left\{ \frac{\alpha}{4} + \beta_P\Delta_{xx}^2 + \pi^2 \left(\frac{K_{123}D^2 + K_1L^2}{4D^2L^2} \right) \right\} \\ + \Delta_{zz}^2 \left\{ \frac{\alpha}{4} + \beta_{12}\Delta_{xx}^2 + \pi^2 \left(\frac{K_1D^2 + K_{123}L^2}{4D^2L^2} \right) \right\},$$

where $\beta_{ijk\dots} = \beta_i + \beta_j + \beta_k + \dots$, $K_{ijk\dots} = K_i + K_j + K_k + \dots$ and $\beta_P = \beta_{12} + 1/2\beta_{345}$ determines bulk free energy of the Planar phase. Minimizing F_{var} with respect to Δ_{xx}^2 gives,

$$(7.20) \quad \Delta_{xx}^2 = \frac{|\alpha|}{2\beta_P} - \frac{\Delta_{zx}^2}{8} - \frac{\Delta_{zz}^2\beta_{12}}{8\beta_P}.$$

The reduced free energy functional then simplifies to

$$(7.21) \quad F_{\text{var}} = -\frac{\alpha^2}{4\beta_P} - \frac{\pi^2 K_{23} \Delta_{zx} \Delta_{zz}}{2DL} \\ + \Delta_{zx}^2 \left\{ \pi^2 \left(\frac{K_{123} D^2 + K_1 L^2}{4D^2 L^2} \right) \right\} \\ + \Delta_{zz}^2 \left\{ \alpha \left(\frac{\beta_P - \beta_{12}}{4\beta_P} \right) + \pi^2 \left(\frac{K_1 D^2 + K_{123} L^2}{4D^2 L^2} \right) \right\}.$$

The last three terms in Eq. 7.21 determine when nonzero values of Δ_{zx} and Δ_{zz} are favorable and the Stripe-Planar instability occurs. At the instability

$$(7.22) \quad \alpha(T) = -\frac{\pi^2 \beta_P}{D^2 L^2 (\beta_P - \beta_{12})} \left\{ -2DLK_{23} \left(\frac{\Delta_{zx}}{\Delta_{zz}} \right) \right. \\ \left. + (D^2 K_{123} + L^2 K_1) \left(\frac{\Delta_{zx}}{\Delta_{zz}} \right)^2 + (D^2 K_1 + L^2 K_{123}) \right\}.$$

Minimizing F_{var} with respect to the ratio Δ_{zx}/Δ_{zz} gives

$$(7.23) \quad \frac{\Delta_{zx}}{\Delta_{zz}} = \frac{DLK_{23}}{D^2 K_{123} + L^2 K_1}.$$

Combining Eq. 7.23 with Eq. 7.22 yields the Planar-Stripe instability temperature, T_{PS} , as a function of D and L . Optimizing T_{PS} with respect to the Stripe phase period yields,

$$(7.24) \quad L = \sqrt{\frac{K_{123}}{|K_{23} - K_1|}} D,$$

which for weak-coupling values of K_1 , K_2 , and K_3 , reduces to $L = \sqrt{3}D$.

Although the Planar to Stripe transition is interrupted by a first-order transition to the A phase, the Stripe-Planar instability determines the scale of the half period, L , and the temperature region where the Stripe phase is expected to be stable. The half-period defines the wavenumber, $Q_0 = \pi/\sqrt{3}D$, of the single-mode instability at T_{PS} . The wavenumber varies with the film thickness, D , and temperature. Figure 7.6 shows the temperature dependence of Q for two values of the film thickness starting from the Planar to Stripe instability at T_{PS} , i.e. omitting the A phase. The stability of the A-phase relative to the Planar phase changes the Stripe instability to a first-order transition at a lower temperature T_{AS} . For $D = 11 \xi_0$ the stable region of Stripe phase persists to $T = 0$, while for $D = 11.5 \xi_0$ there is a Stripe to B phase transition at a temperature, $T_{\text{SB}} < T_{\text{PS}}$. In both cases the wavenumber decreases (L increases) as T drops below T_{PS} , with $Q \rightarrow 0$ ($L \rightarrow \infty$) as $T \rightarrow T_{\text{SB}}$. Strong coupling corrections to the free energy lead to a modest increase the period of the Stripe phase away from the Stripe to B transition; however, the transition temperature, T_{SB} , is sensitive to pressure (strong-coupling) as shown in the right panel of Fig. 7.6.

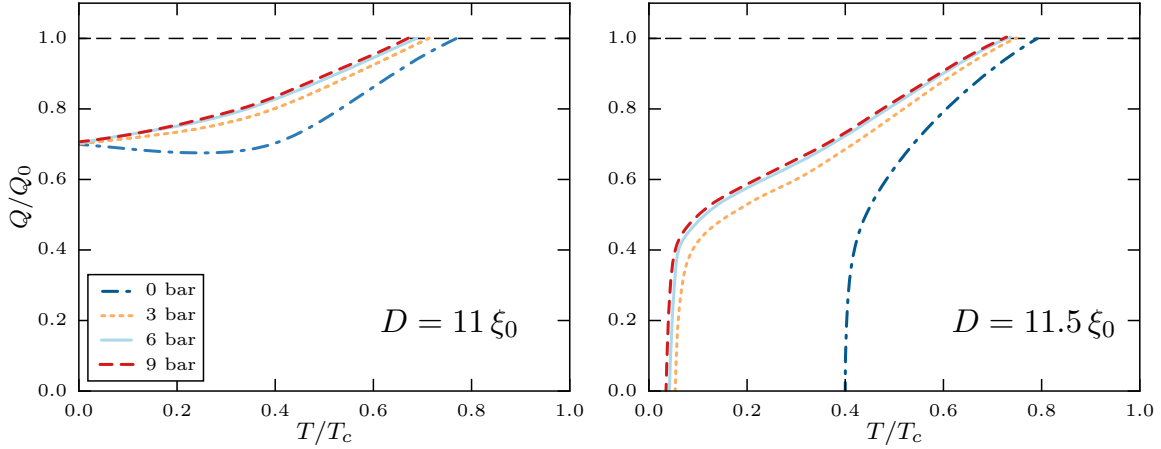


Figure 7.6. Temperature and pressure dependence of the wavenumber Q for film thicknesses $D = 11 \xi_0$, with no Stripe to B transition (left panel), and $D = 11.5 \xi_0$, with a Stripe to B transition (right panel). The onset of the Stripe transition is based on the Planar-Stripe instability, i.e. omitting the A phase.

7.5. Stripe Phase Stability

The most prominent effect of strong-coupling corrections to the weak-coupling BCS theory in bulk superfluid ^3He is the stability of the A phase above $p_{\text{PCP}} = 21.22$ bar. In sufficiently thin films, the A phase is energetically stable relative to the B phase even in weak-coupling theory, and is degenerate with the Planar phase [98, 99]. Strong-coupling corrections favor the A phase over the Planar phase, leading to a stable A-phase in thin films at all pressures. Since the Stripe phase can be understood as a periodic array of degenerate B phase domains separated by time-reversal invariant domain walls, one expects strong-coupling to favor the A phase near the Planar-Stripe instability line. Indeed the A phase suppresses the Planar to Stripe instability temperature. However, the Stripe phase is found to be stable over a wide range of temperatures and pressures.

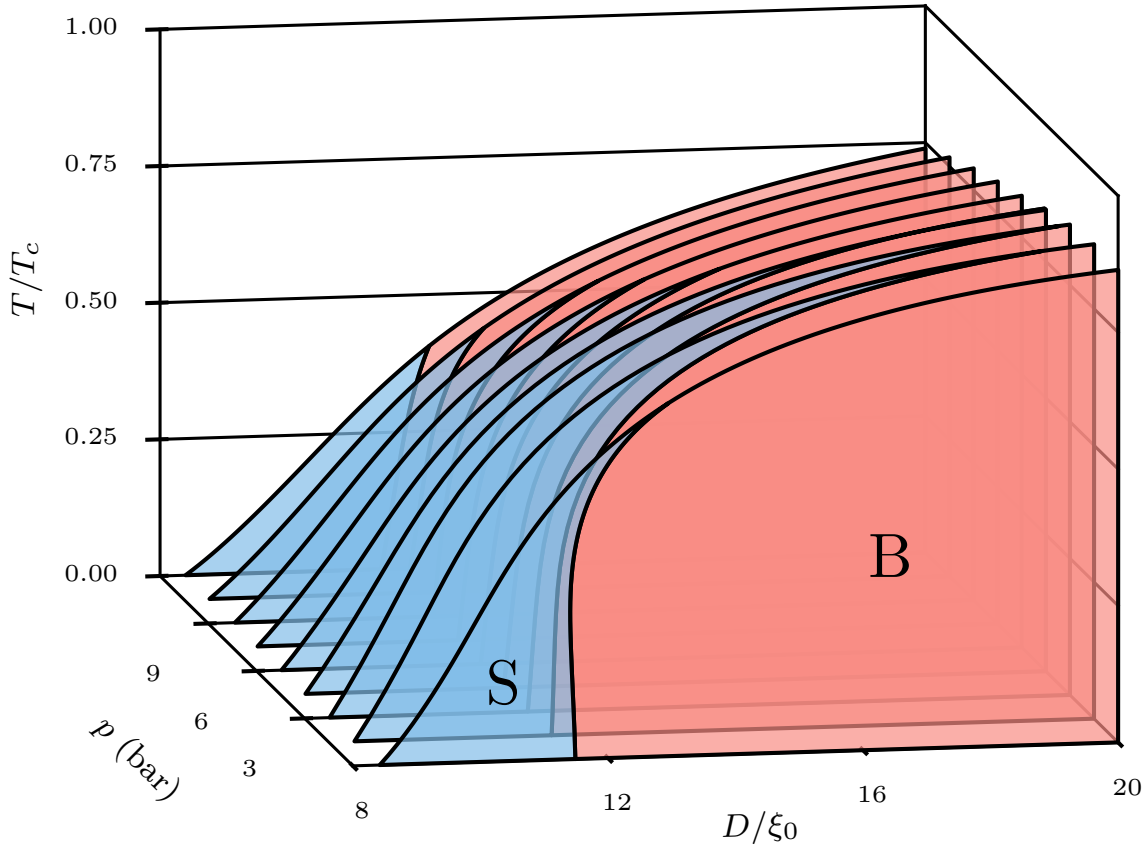


Figure 7.7. Pressure-temperature-confinement phase diagram for the film with minimal pairbreaking boundaries and experimental strong-coupling corrections. The A phase is stable everywhere not excluded by the Stripe and B phases.

Figure 7.7 shows the phase diagram for minimal pairbreaking (specular) surfaces at pressures from 0 to 12 bar, with the Stripe phase onsetting at temperatures above $0.5T_c$. The accuracy of the strong-coupling GL theory is expected to diminish at very low temperatures; therefore we show results for low and intermediate pressures for which the A- to Stripe transition onsets above $0.5T_c$. Note that at $T = 0$ the strong-coupling GL corrections vanish, and the phase boundaries are determined by weak-coupling theory at $T = 0$ and thus pressure independent. This is an artefact of the temperature scaling of

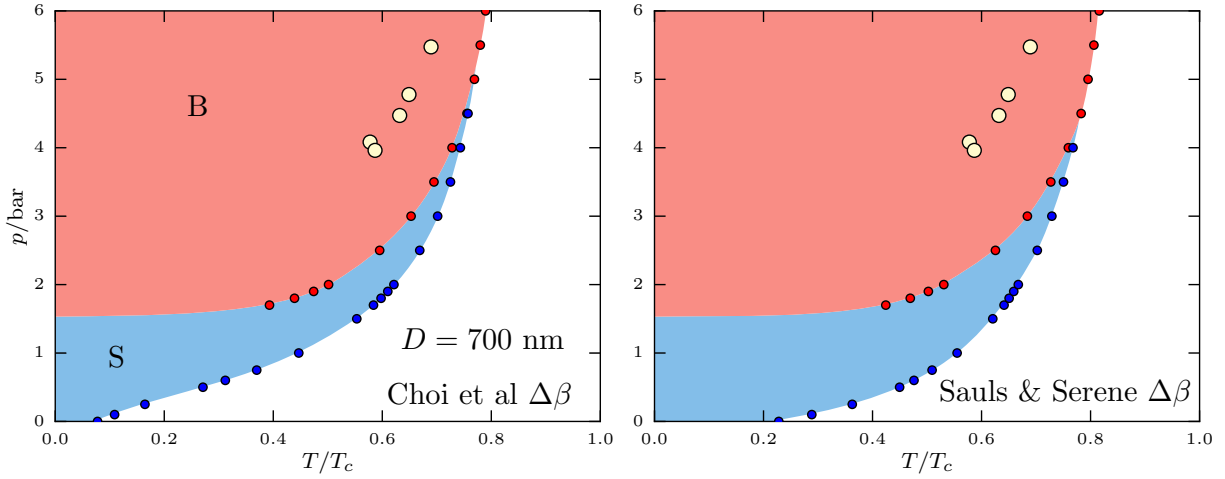


Figure 7.8. Pressure-temperature phase diagram for a film of thickness $D = 700$ nm with minimal pairbreaking (specular) boundary conditions. The A phase is stable everywhere in the white region below the bulk transition temperature. The larger yellow circles are data for the A-B transition based on NMR from Levitin et al obtained with ^4He preplating [50].

the strong-coupling GL parameters. It is known that there are residual strong-coupling corrections at the few percent level in the limit $T = 0$ [86].

A striking difference between the two sets of strong-coupling β parameters shown in Figs. 7.1 and 7.2 is evident at low pressures. The $\Delta\beta_i^{\text{sc}}$ from Choi et al. [24] are non-monotonic between $p = 0$ and $p = 12$ bar, which leads to maximal stability of the Stripe phase at $p \approx 3$ bar. In contrast the theoretically calculated strong-coupling corrections are monotonic functions of pressure and predict maximal stability of the Stripe phase at $p = 0$ bar and decreasing stability with increasing pressure. ³

7.5.1. Pressure-Temperature Phase Diagram

Although a number of experiments have been reported on superfluid ^3He in planar geometries, of particular interest are those involving slabs of thickness $D \approx 700$ nm and $D \approx 1080$ nm, which are in the range of confinement where the Stripe phase is expected to be stable. Levitin et al. [50] (RHUL group) used transverse NMR frequency shifts to determine transition temperatures in these cells. They did not find NMR evidence of the Stripe phase. These experiments were done both with and without preplating the surfaces of the slab with ^4He , the presence of which greatly increases the specularity of the surface. Without the ^4He present, the RHUL group reported large suppression of the onset of the superfluid transition - a suppression larger than that predicted theoretically for maximally pairbreaking retro-reflective surface scattering. The explanation or origin of this anomalous suppression is currently lacking. Thus, we focus on the measurements done with ^4He preplating, which exhibit minimal T_c suppression, and may be modeled theoretically with minimal pairbreaking boundary conditions (specular scattering).

Calculations of the phase diagram for $D = 700$ nm are shown in Fig. 7.8. The A phase onsets at the bulk T_c . There is an A to Stripe transition followed by the Stripe to B transition. For both sets of strong-coupling β parameters, the Stripe phase is predicted to be stable at low pressures and at experimentally accessible temperatures. Although the stability of the A phase is maximal with specular boundary conditions, the calculated A-B or A-S phase transition occurs at significantly higher temperature than that reported by the RHUL group. The discrepancy is sufficiently large that it is well outside uncertainties

³New microscopic calculations in Chapter 8 accurately reproduce the thermodynamic potential and bulk phase diagram without significant non-monotonicity.

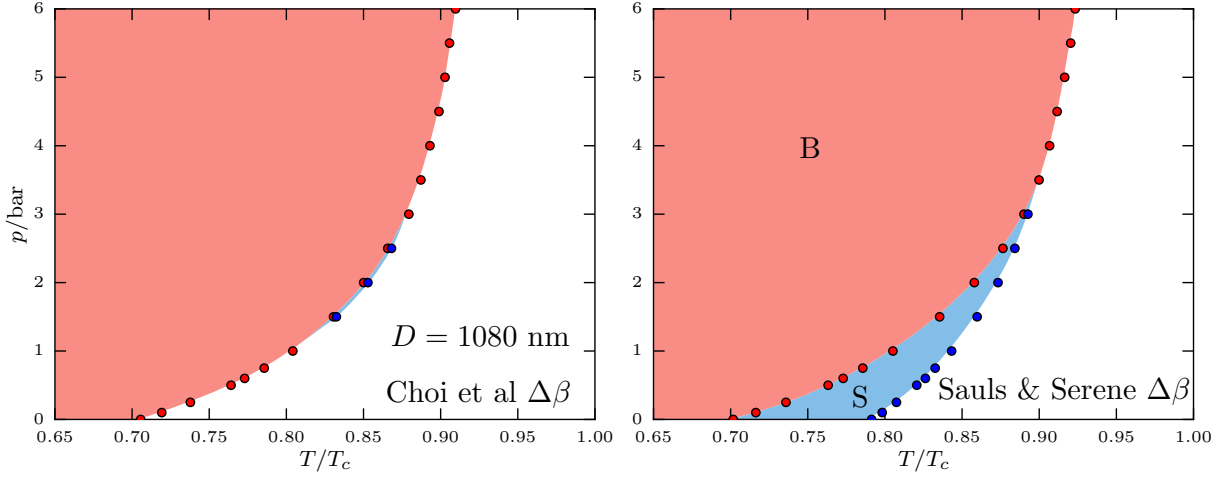


Figure 7.9. Pressure-temperature phase diagram for a film of thickness $D = 1080$ nm with minimal pairbreaking boundaries. The A phase is stable everywhere not excluded by the Stripe and B phases.

in the magnitude of the strong-coupling parameters based bulk A- and B phase free energies. Based on our calculations accessing the Stripe phase would be optimal for pressures between $p = 1$ and $p = 1.5$ bar.

For the thicker slab geometry, $D = 1080$ nm, shown in Figure 7.9, the Stripe phase is predicted to have a negligible region of stability in the pressure-temperature plane based on the β parameters from Choi et al. [24], and only a small window of stability at the lowest pressures based on the theoretically calculated strong-coupling parameters.

7.5.2. Effects of Surface Conditions on the Phase Diagram

We use the variable boundary conditions in Eqs. 7.11 to investigate the sensitivity of the Stripe phase to surface disorder. Figure 7.10 shows the temperature-confinement phase diagram at $p = 3$ bar for maximal ($b'_T = 0$), diffuse ($b'_T = 0.54$), and minimal ($b'_T = \infty$) pairbreaking boundary conditions. Maximal stability of the Stripe phase occurs

for minimal pairbreaking, i.e. specular surfaces, as shown by the blue region of stable Stripe phase. Note that for diffuse scattering the region of Stripe phase stability does not differ significantly from that for specular boundary scattering. Conversely, for maximal pairbreaking the Stripe phase exists only in the vicinity of $T = 0$.

7.6. NMR Signatures of the Stripe Phase

Nuclear magnetic resonance (NMR) spectroscopy of the ^3He order parameter is based on resonance frequency shifts originating from the Cooper pair contribution to the nuclear magnetic dipole energy, $\Delta\Omega_D = \int_V d^3r f_D[A]$, which evaluated to leading order in A is

$$(7.25) \quad f_D = g_D (|TrA|^2 + TrAA^*) ,$$

where $g_D = \frac{\chi}{2\gamma^2} \Omega_A^2 / \Delta_A^2$ is the nuclear dipole coupling, γ is the ^3He nuclear gyromagnetic ratio, χ is the nuclear magnetic susceptibility of normal ^3He , and Ω_A is the A phase longitudinal NMR resonance frequency. The dipole energy, of order $g_D \Delta_A^2$, lifts the degeneracy of relative rotations of the spin- and orbital state of the Cooper pairs.

NMR spectroscopy is based on the NMR frequency shift, $\Delta\omega = \omega - \omega_L$, resulting from the dipolar torque acting on the total nuclear magnetization. The shift depends in general on the orientation of the NMR field, \mathbf{H} , the initial tipping angle, β , generated by the r.f. pulse, and particularly the spin- and orbital structure of the order parameter. We use the reduction of Leggett's theory of NMR in ^3He proposed by Fomin [33],⁴ valid for intermediate magnetic fields, $\Omega_A \ll \omega_L \ll \Delta$, where $\omega_L = \gamma H$ is the Larmor frequency [33]. The key approximation is the first inequality which provides a separation

⁴This theory is explained in detail in Section 5.6.

of “fast” and “slow” timescales for the spin dynamics. The second inequality allows us to neglect the deformation of the order parameter by the Zeeman field. Similarly, for inhomogeneous states we use the separation of length scales for spatial variations of the Stripe phase, of order $L \sim D \approx 1 \mu\text{m}$, both small compared to the dipole coherence length, $\xi_D \equiv \sqrt{g_D/K_1} \approx 20 \mu\text{m}$. The spin degrees of freedom of the order parameter cannot vary on length scales shorter than the dipole coherence length ξ_D . Thus, for $L \ll \xi_D$ the nuclear spin dynamics is determined by the spatially averaged dipole energy. An exception to this spatial averaging occurs near the Stripe-B transition where the period of the Stripe phase diverges. In this limit the dipolar energy varies on sufficiently long spatial scales that the spin dynamics is determined by a spatially varying dipolar potential. Combined with Fomin’s formulation, the separation in scales for spatial variations of the orbital and spin components of the order parameter allows us to calculate the nonlinear NMR frequency shifts for the inhomogeneous phases of the thin film as described in Ref. [104].

7.6.1. Translationally invariant Planar-distorted B phase

For non-equal-spin pairing (non-ESP) states, e.g. the polar distorted B phase or the Stripe phase, the nuclear magnetic susceptibility, χ , is suppressed relative to that of normal ^3He , χ_N . For all non-ESP phases, including the Stripe phase, the susceptibility can be expressed as

$$(7.26) \quad \chi_B = \frac{\chi_N}{1 + 2g_z/\chi_N(\langle\Delta_{zx}^2\rangle + \langle\Delta_{zz}^2\rangle)}.$$

For a non-ESP superfluid phase of a ^3He film with the magnetic field $\vec{H}||\mathbf{z}$, for both the B and Stripe phases, there are two possible dipole orientations corresponding to different

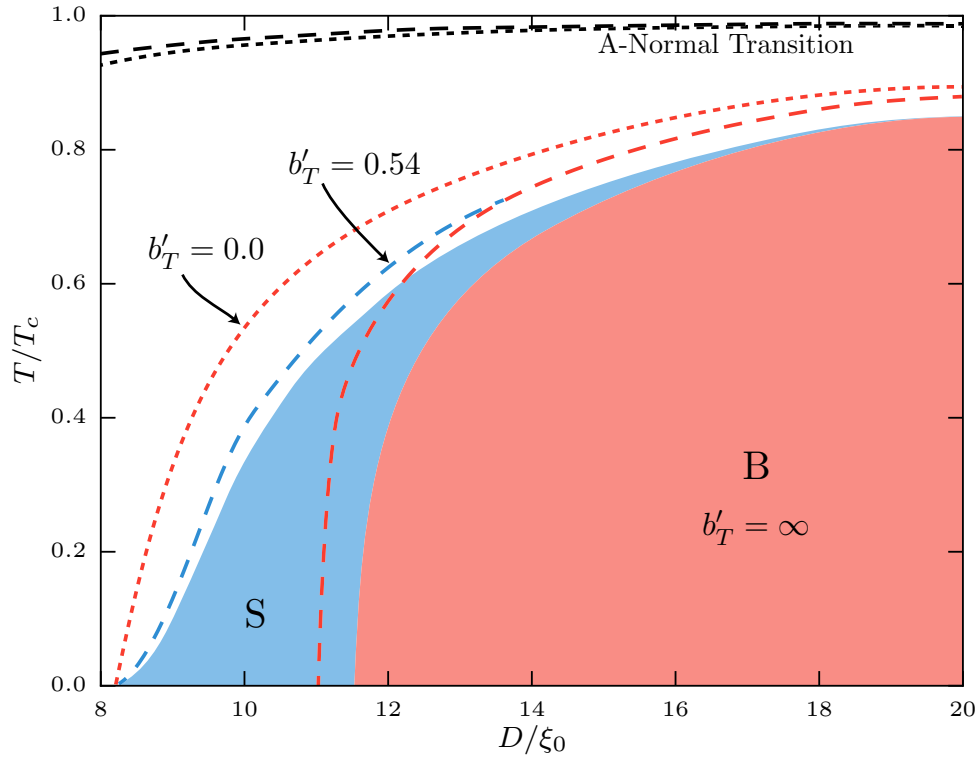


Figure 7.10. Temperature-confinement phase diagram for films at $p = 3$ bar with the Choi et al. strong-coupling corrections. Results for three boundary conditions are shown: minimal pairbreaking, $b'_T \rightarrow \infty$ (solid); diffuse, $b'_T = 0.54$ (dashed); and maximal pairbreaking, $b'_T = 0$ (dotted). For diffuse and maximal pairbreaking, the suppression of the A to Normal phase transitions are also shown.

local minima in the dipole energy [22]. The first orientation is a minimum of the dipole energy and has positive frequency shift, which following Levitin et al[51] we denote as the B^+ state in the case of the translationally invariant B phase. The frequency shift for

the B^+ state is obtained as

(7.27)

$$\omega\Delta\omega^+ = \frac{\gamma^2}{\chi_B} g_D \times \begin{cases} \frac{\langle\Delta_x^2\rangle^2 - \langle A_{xx}A_{zz}\rangle^2}{\langle\Delta_x^2\rangle} + 2\left(\frac{\langle A_{xx}A_{zz}\rangle^2}{\langle\Delta_x^2\rangle} - \langle\Delta_z^2\rangle\right) \cos\beta, & \cos\beta \geq \cos\beta^*, \\ -\langle\Delta_x^2\rangle - \langle A_{xx}A_{zz}\rangle - 2\langle(A_{xx} + A_{zz})^2\rangle \cos\beta, & \cos\beta < \cos\beta^*, \end{cases}$$

where $\langle\dots\rangle = (1/V) \int_V d^3R\dots$ denotes spatial averaging, and

$$(7.28) \quad \cos\beta^* = \frac{1}{2} \left(\frac{\langle A_{xx}A_{zz}\rangle - 2\langle\Delta_x^2\rangle}{\langle A_{xx}A_{zz}\rangle + \langle\Delta_x^2\rangle} \right)$$

is the critical angle.

Axial symmetry of the Planar-distorted B phase implies $\langle\Delta_y^2\rangle = \langle\Delta_x^2\rangle$; thus, only $\langle\Delta_x^2\rangle$, $\langle\Delta_z^2\rangle$, and $\langle A_{xx}A_{zz}\rangle$ are non-zero. This NMR resonance is analogous to the Brinkman-Smith mode in bulk $^3\text{He-B}$, but with a positive frequency shift at small tipping angle and a shifted critical angle.

The translationally invariant, but meta-stable, B_- state, corresponds to a minimum of the dipole energy, and has a frequency shift given by

$$(7.29) \quad \omega\Delta\omega^- = \frac{\gamma^2}{\chi_B} g_D \left\{ -(\langle\Delta_x^2\rangle + 2\langle\Delta_z^2\rangle) \cos\beta \right\}.$$

This mode has a negative frequency shift at small tipping angles and, unlike the B_+ state, has no critical angle, and therefore no deviation from cosine tipping angle dependence. The tipping angle dependences of both Planar-distorted B phase states are shown in Fig. 7.11 plotted as a function of $\cos\beta$. The positive (negative) shift at small tipping angle is the signature of the of the B^+ (B^-) state in the NMR spectra of the RHUL group [50].

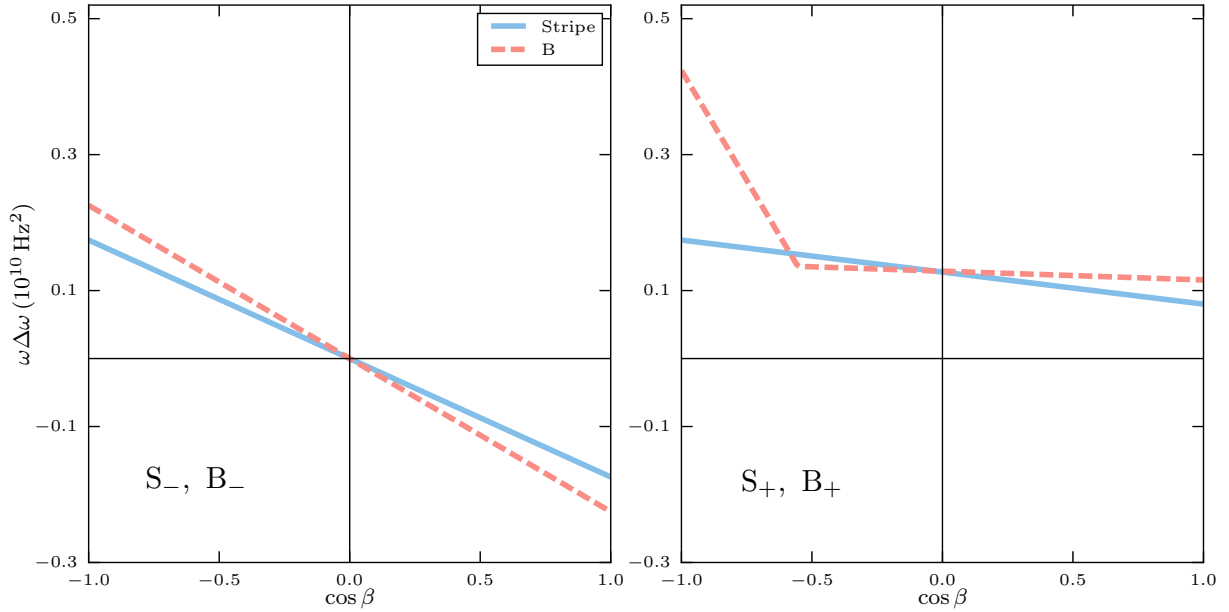


Figure 7.11. Transverse NMR frequency shifts as a function of tipping angle β at $D = 12\xi_0$, $p = 3$ bar, and $T = 0.5T_c$, with minimal pairbreaking for the B^\pm and S^\pm states.

These identifications are confirmed by nonlinear NMR measurements [51] showing both the pure cosine tipping angle dependence of $\omega\Delta\omega$ for the B^- state, and the “kink” in the shift at the critical angle β^* for the B^+ state. Note that for $D = 12\xi_0$ at $p = 3$ bar there is a small slope to the positive shift for $\cos\beta > \cos\beta^*$.

7.6.2. Nonlinear NMR shifts for the S^\pm Stripe phases

The breaking of both translational and rotational symmetry in the plane of the film by the Stripe phase leads to a qualitatively different transverse NMR frequency shift for the Stripe phase with relative spin-orbit rotation corresponding to a minimum of the dipole

energy, i.e. the S^+ state,

$$(7.30) \quad \omega\Delta\omega^+ = \frac{1}{4} \frac{\gamma^2}{\chi_B} g_D \left\{ \langle (A_{yy} + A_{xx})^2 \rangle - \left[\langle (A_{yy} - A_{xx})^2 \rangle + 8 \langle \Delta_z^2 \rangle - 4 (\langle A_{xz}^2 \rangle + \langle A_{zx}^2 \rangle) \right] \cos \beta \right\}.$$

The S^+ phase is distinguished with respect to both the bulk B phase and the Planar-distorted B^+ phase by the absence of a critical tipping angle. This results from spatial averaging over the period of the Stripe phase which contains equal volumes of $A_{zz} > 0$ and $A_{zz} < 0$ giving $\langle A_{xx}A_{zz} \rangle = \langle A_{yy}A_{zz} \rangle = 0$.

By contrast the frequency shift of the metastable S^- phase does not differ substantially from that of the B^- phase,

$$(7.31) \quad \omega\Delta\omega^- = \frac{1}{4} \frac{\gamma^2}{\chi_B} g_D \left\{ \langle (A_{yy} - A_{xx})^2 \rangle (1 + \cos \beta) - \left[2 \langle \Delta_x^2 \rangle + 2 \langle \Delta_y^2 \rangle + 8 \langle \Delta_z^2 \rangle - 4 (\langle A_{xz}^2 \rangle + \langle A_{zx}^2 \rangle) \right] \cos \beta \right\}.$$

Note that the constant term in the shift for the S^- state proportional to the average $\langle (A_{yy} - A_{xx})^2 \rangle$ is absent for the B^- state; however, this constant shift is negligibly small. Figure 7.11 shows the comparison between the translationally invariant B^\pm NMR shifts and those for the corresponding stable and metastable S^\pm Stripe phases. The primary NMR signature of the Stripe phase is the positive shift with an offset, a finite slope and the absence of critical angle. This signature clearly differentiates the S^+ phase from the B^\pm states and the A phase.

7.7. Summary and Outlook

By formulating a GL theory that incorporates pressure and temperature dependent strong-coupling corrections, combined with temperature dependent rescaling of the confinement length, D , we have greatly expanded the region of applicability of GL theory for calculations of the properties of confined superfluid ^3He . Strong-coupling corrections expand the region of stability of the A phase and decrease the region of stability of the Stripe phase; however, the Stripe phase remains stable in a large region of pressure, temperature, and confinement. The stability of the Stripe phase is insensitive to diffuse surface scattering; the phase diagram for specular and fully diffusive scattering predict the Stripe phase to occur in nearly equivalent regions of the phase diagram. Nonlinear NMR measurements are probably the best means of detecting the Stripe phase. The NMR signatures - positive shift with no critical angle - differentiates the S^+ phase from the B^\pm and A phases.

Acknowledgements — The research of JJW and JAS was supported by the National Science Foundation (Grants DMR-1106315 and DMR-1508730).

CHAPTER 8

Strong-coupling: Superfluid ^3He as the precursor to an anti-ferromagnetic solid

8.1. Introduction

While the prior chapters of this thesis have made extensive use of strong-coupling corrections, they have done so in the Ginzburg-Landau theory using strong-coupling material coefficients inferred from experiment. This treatment cannot include low temperatures and small length scales beyond the Ginzburg-Landau regime. It also is subject to substantial theoretical uncertainty, because the strong-coupling corrections inferred by Choi et al[23] look nothing like those previously calculated using microscopic theory[81]. In this chapter we revisit the theory of the stability of the A phase with a microscopic strong-coupling theory based on the Luttinger-Ward free-energy functional and quasiclassical theory.

Attempts to understand the fine details of ^3He quasiparticle interactions and their influence on the superfluid state predate the experimental discovery of the superfluid. Fay and Layzer[31] in 1968 showed that many-body effects could favor p -wave pairing in ferromagnetic (FM) neutral Fermi systems, specifically ^3He . The resulting paramagnon exchange model, and the “feedback mechanism” of Anderson and Brinkman[7], provided a plausible explanation as to what stabilized the superfluid A phase at pressures above p_{PCP} and temperatures near T_c . [47, 16].

The feedback mechanism mediated by paramagnon exchange, however, was mostly qualitative. Attempts to get a quantitative handle on the relative stability of the superfluid phases lead to models including more complicated interactions. One of the most useful formalisms developed for this was the quasiclassical reduction of the Luttinger-Ward free-energy functional developed by Rainer and Serene.[72] The free-energy functional approach could be used to calculate static and dynamic properties for both the normal Fermi liquid and the superfluid phases. Sauls and Serene[81] used this technique to calculate superfluid energetics in the Ginzburg-Landau regime, and it was later shown to fit Greywall's B-phase specific heat measurements exceptionally well.[39]

8.2. Free-energy functional

We consider the quasiclassical reduction of the Luttinger-Ward free-energy functional introduced by Rainer & Serene.[72] The full Luttinger-Ward functional is

$$\begin{aligned}
 \Omega[\widehat{G}, \widehat{\Sigma}] = & -\frac{T}{2} \sum_{\varepsilon_n} \int \frac{d^3k}{(2\pi)^3} \text{Tr}_4 \left\{ \widehat{\Sigma}(\vec{k}, \varepsilon_n) \widehat{G}(\vec{k}, \varepsilon_n) \right. \\
 & \left. + \ln[-\widehat{G}_0^{-1}(\vec{k}, \varepsilon_n) + \widehat{\Sigma}(\vec{k}, \varepsilon_n)] \right\} \\
 (8.1) \quad & + \Phi[\widehat{G}],
 \end{aligned}$$

where the full Nambu space propagators are given by

$$(8.2) \quad \widehat{G}(\vec{k}, \varepsilon_n) = \begin{pmatrix} \widehat{G}(\vec{k}, \varepsilon_n) & \widehat{F}(\vec{k}, \varepsilon_n) \\ \widehat{F}^\dagger(\vec{k}, -\varepsilon_n) & -\widehat{G}^{\text{tr}}(-\vec{k}, -\varepsilon_n) \end{pmatrix}$$

$$(8.3) \quad \widehat{\Sigma}(\vec{k}, \varepsilon_n) = \begin{pmatrix} \widehat{\Sigma}(\vec{k}, \varepsilon_n) & \widehat{\Delta}(\vec{k}, \varepsilon_n) \\ \widehat{\Delta}^\dagger(\vec{k}, -\varepsilon_n) & -\widehat{\Sigma}^{\text{tr}}(-\vec{k}, -\varepsilon_n) \end{pmatrix},$$

with

$$(8.4) \quad G_{\alpha\delta}(\vec{k}, \varepsilon_n) = - \int_0^\beta d\tau e^{i\varepsilon_n\tau} \langle T_\tau a_{\vec{k}\alpha}(\tau) a_{\vec{k}\delta}^\dagger(0) \rangle$$

$$(8.5) \quad G_{\alpha\delta}^T(-\vec{k}, -\varepsilon_n) = - \int_0^\beta d\tau e^{-i\varepsilon_n\tau} \langle T_\tau a_{-\vec{k}\delta}(\tau) a_{-\vec{k}\alpha}^\dagger(0) \rangle$$

$$(8.6) \quad F_{\alpha\delta}(\vec{k}, \varepsilon_n) = - \int_0^\beta d\tau e^{i\varepsilon_n\tau} \langle T_\tau a_{\vec{k}\alpha}(\tau) a_{-\vec{k}\delta}(0) \rangle$$

$$(8.7) \quad F_{\alpha\delta}^\dagger(\vec{k}, \varepsilon_n) = - \int_0^\beta d\tau e^{-i\varepsilon_n\tau} \langle T_\tau a_{-\vec{k}\alpha}^\dagger(\tau) a_{\vec{k}\delta}^\dagger(0) \rangle$$

The propagator \widehat{G} is fixed in terms of $\widehat{\Sigma}$ by the Dyson equation as

$$(8.8) \quad \widehat{G}^{-1}(\vec{k}, \varepsilon_n) = \widehat{G}_0^{-1}(\vec{k}, \varepsilon_n) - \widehat{\Sigma}(\vec{k}, \varepsilon_n),$$

where \widehat{G}_0 is the propagator for noninteracting fermions. Eq. 8.8 leads to the stationarity property

$$(8.9) \quad \delta\Omega[\widehat{G}, \widehat{\Sigma}] / \delta\widehat{\Sigma}^{\text{tr}}(\vec{k}, \varepsilon_n) = 0,$$

in which \widehat{G} and $\widehat{\Sigma}$ are treated as independent. A further stationarity property,

$$(8.10) \quad \delta\Omega[\widehat{G}, \widehat{\Sigma}]/\delta\widehat{G}^{\text{tr}}(\vec{k}, \varepsilon_n) = 0,$$

defines $\Phi[\widehat{G}]$ in terms of the skeleton expansion of the self-energy,

$$(8.11) \quad \widehat{\Sigma} = \widehat{\Sigma}_{\text{skel}} = 2\delta\Phi[\widehat{G}]/\delta\widehat{G}^{\text{tr}}.$$

To form the quasiclassical reduction of the free-energy functional, we first subtract off the normal state Ω_N with

$$(8.12) \quad \begin{aligned} \Delta\widehat{\Sigma} &= \widehat{\Sigma} - \widehat{\Sigma}_N \\ \Delta\widehat{G} &= \widehat{G} - \widehat{G}_N, \end{aligned}$$

and

$$(8.13) \quad \begin{aligned} \Delta\Omega[\Delta\widehat{G}, \Delta\widehat{\Sigma}] &= \Omega[\widehat{\Sigma}] - \Omega[\widehat{\Sigma}_N] \\ &= -\frac{T}{2} \sum_{\varepsilon_n} \int \frac{d^3k}{(2\pi)^3} \text{Tr}_4 \left\{ \Delta\widehat{\Sigma} \widehat{G} \right. \\ &\quad \left. + \ln[-\widehat{G}_N^{-1} + \Delta\widehat{\Sigma}] - \ln[-\widehat{G}_N^{-1}] \right\} + \Delta\Phi[\widehat{G}]. \end{aligned}$$

The subtracted Φ term is given by

$$(8.14) \quad \Delta\Phi[\widehat{G}] = \Phi[\widehat{G}] - \Phi[\widehat{G}_N] - \frac{T}{2} \sum_{\varepsilon_n} \int \frac{d^3k}{(2\pi)^3} \text{Tr}_4[\widehat{\Sigma}_N \Delta\widehat{G}].$$

The quasiclassical reduction proceeds from the observation that the energy scale of the superfluid Cooper pairs, T_c , is much less than the Fermi scale T_f . This allows the

problem to be simplified by restricting the propagator to a shell of width $2E_c$ about the Fermi surface, where $E_c \ll E_f$. The high-energy contributions beyond this shell are essentially integrated out and replaced by phenomenological parameters. The quasiclassical propagator is then defined by

$$(8.15) \quad \widehat{g}(\hat{p}, \varepsilon_n) \equiv \frac{1}{a} \int_{-E_c}^{+E_c} d\xi_p \widehat{\tau}_3 \widehat{G}(\vec{p}, \varepsilon_n)$$

where $\xi_p = v_f(|p| - p_f)$ and a is the weight of the quasiparticle pole in the spectral function used to normalize the propagator. The quasiclassical self-energy we split into leading and next-to-leading order contributions through

$$(8.16) \quad \begin{aligned} \widehat{\sigma} &\equiv \widehat{\Sigma}(p_f \hat{p}, \varepsilon_n) \widehat{\tau}_3 \\ &= \widehat{\sigma}_{\text{wc}} + \widehat{\sigma}_{\text{sc}} \end{aligned}$$

$$(8.17) \quad \begin{aligned} \widehat{\sigma}_{\text{wc}} &= 2 \delta \Delta \Phi[\widehat{g}]_{\text{wc}} / \delta \widehat{g}^{\text{tr}} \\ \widehat{\sigma}_{\text{sc}} &= 2 \delta \Delta \Phi[\widehat{g}]_{\text{sc}} / \delta \widehat{g}^{\text{tr}}, \end{aligned}$$

where $\Delta \Phi_{\text{wc}}$ reproduces the weak-coupling BCS functional, $\Delta \Phi_{\text{sc}}$ contains higher order terms, and $\widehat{\tau}_i$ denote Pauli matrices in particle-hole (Nambu) space. The $\Delta \Phi_{\text{sc}}$ is formally of order $(T/T_c)^3$ and to this order can be evaluated at the weak-coupling stationary point, $\Delta \Phi_{\text{sc}}[\widehat{g}_{\text{wc}}] = \Delta \Phi_{\text{sc}} \left[\int d\xi_p (i\varepsilon_n \widehat{\tau}_3 - \xi_p \widehat{1} - \widehat{\sigma}_{\text{wc}})^{-1} \right]$.

After simplification, the quasiclassical free-energy functional is

$$\begin{aligned}
\Delta\Omega[\widehat{g}, \widehat{\sigma}_{\text{wc}}] = & -\frac{N(0)T}{2} \sum_{\varepsilon_n} \int \frac{d\Omega_p}{4\pi} \text{Tr}_4 \left\{ \widehat{\sigma}_{\text{wc}} \widehat{g} \right. \\
& \left. + \int d\xi_p \left(\ln[-\widehat{G}_0^{-1} + \widehat{\sigma}_{\text{wc}}] - \ln[-\widehat{G}_0^{-1}] \right) \right\} \\
(8.18) \quad & + \Delta\Phi_{\text{wc}}[\widehat{g}] + \Delta\Phi_{\text{sc}}[\widehat{\sigma}_{\text{wc}}].
\end{aligned}$$

where the normal-state quasiparticle propagator is

$$(8.19) \quad \widehat{G}_N^{-1} = i\varepsilon_n \widehat{\tau}_3 - \xi_p \widehat{1}$$

Note that while \widehat{g} is the full propagator, $\widehat{\sigma}_{\text{sc}}$ no longer appears explicitly in Eq. 8.18. This means that we may eliminate \widehat{g} using $\widehat{\sigma} = 2 \delta\Delta\Phi[\widehat{g}]_{\text{wc}}/\delta\widehat{g}^{\text{tr}}$.

For homogeneous, unitary phases without external fields, we can further simplify the functional by taking $\widehat{\sigma} = \widehat{\Delta}$ and evaluate the logarithm and $\Delta\Phi_{\text{wc}}$ in the usual manner[86],

$$\begin{aligned}
\Delta\Omega[\widehat{\Delta}] = & N(0) \int \frac{d\Omega_p}{4\pi} \left\{ \ln(T/T_c) |\Delta|^2 \right. \\
& \left. + \pi T \sum_n \frac{|\Delta|^4}{|\varepsilon_n| (|\varepsilon_n| + \sqrt{\varepsilon_n^2 + |\Delta|^2})^2} \right\} \\
(8.20) \quad & + \Delta\Phi_{\text{sc}}[\widehat{\Delta}].
\end{aligned}$$

The propagator \hat{g} in this approximation is given equivalently by Eilenberger's transport equation and normalization,

$$(8.21) \quad 0 = [i\varepsilon_n \hat{\tau}_3 - \hat{\Delta}, \hat{g}] + i v_F \hat{p}_F \cdot \nabla \hat{g}$$

$$(8.22) \quad \hat{g}^2 = -\pi^2 \hat{1},$$

which for homogeneous equilibrium has the solution

$$(8.23) \quad \hat{g} = -\pi \frac{i\varepsilon_n \hat{\tau}_3 - \hat{\Delta}(\hat{p})}{\sqrt{\varepsilon_n^2 + |\hat{\Delta}(\hat{p})|^2}}.$$

The order parameter $\hat{\Delta}$ is given by the stationarity condition

$$(8.24) \quad \delta\Omega/\delta\hat{\Delta}^{\text{tr}} = 0.$$

The strong-coupling contributions to the free-energy functional are described diagrammatically in terms of four propagators,

$$(8.25) \quad \begin{array}{c} \bullet \leftarrow \bullet \rightarrow \bullet \\ \hat{f} \end{array} = \frac{\pi \hat{\Delta}}{\sqrt{\varepsilon_n^2 + |\hat{\Delta}|^2}}$$

$$(8.26) \quad \begin{array}{c} \bullet \rightarrow \bullet \leftarrow \bullet \\ \underline{\hat{f}} \end{array} = \frac{-\pi \hat{\Delta}^*}{\sqrt{\varepsilon_n^2 + |\hat{\Delta}|^2}}$$

$$(8.27) \quad \begin{array}{c} \bullet \leftarrow \bullet \\ \hat{g}_N \end{array} = -i\pi \operatorname{sgn}(\varepsilon_n) \hat{1}$$

$$(8.28) \quad \begin{array}{c} \bullet \leftarrow \bullet \leftarrow \bullet \\ \hat{g} - \hat{g}_N \end{array} = -i\pi \left(\frac{\varepsilon_n}{\sqrt{\varepsilon_n^2 + |\hat{\Delta}|^2}} - \operatorname{sgn}(\varepsilon_n) \right) \hat{1}$$

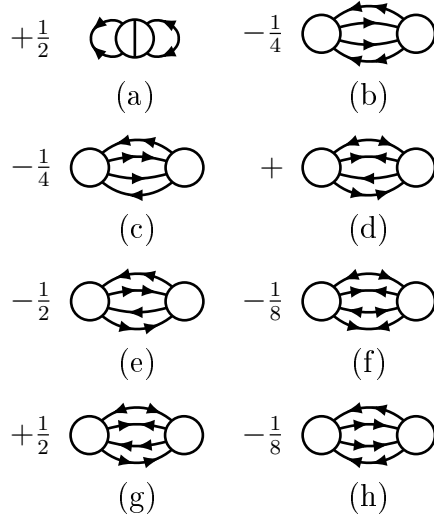


Figure 8.1. Φ diagrams. Diagram (a) generates the usual BCS weak-coupling theory, while diagrams (b) to (h) are next order corrections at $(T_c/T_F)^3$ which contribute to Φ_{sc} and are described further in Appendix A.

where the exact expressions given are valid for the unitary, homogeneous states we consider. The Φ diagrams to order $(T_c/T_F)^3$ are given in Fig. 8.1 and written out explicitly for the A phase in Appendix A.[72] The vertex in the leading diagram (a) is the irreducible particle-particle interaction leading to p -wave superfluidity, while the other vertex appearing in diagrams with four propagator lines is the quasiparticle-quasiparticle scattering amplitude evaluated on the Fermi surface with $\vec{p}_i = p_f \hat{p}_i$ and $\varepsilon_{n_i} = 0$. This vertex T is expressed as

$$(8.29) \quad T_{\alpha, \beta; \gamma, \rho}(\hat{p}_1, \hat{p}_2; \hat{p}_3, \hat{p}_4) = \begin{array}{c} \hat{p}_1, \alpha \quad \hat{p}_2, \beta \\ \swarrow \quad \searrow \\ \textcircled{T} \\ \nearrow \quad \nwarrow \\ \hat{p}_3, \gamma \quad \hat{p}_4, \rho \end{array},$$

where α , β , γ , and ρ are the spin projections (\uparrow or \downarrow) for the incoming and outgoing scattering states.

To order $(T/T_f)^3$ the quasiparticle scattering amplitude reduces to a function of only two variables, which we choose to be the two momentum transfers $q_1 = |\hat{p}_1 - \hat{p}_3|$ and $q_2 = |\hat{p}_1 - \hat{p}_4|$. [81] The vertex is then split into two functions as

$$(8.30) \quad \begin{aligned} T_{\alpha,\beta;\gamma,\rho}(\hat{p}_1, \hat{p}_2; \hat{p}_3, \hat{p}_4) = & \delta_{\alpha\gamma}\delta_{\beta\rho} \nu(q_1) - \delta_{\alpha\rho}\delta_{\beta\gamma} \nu(q_2) \\ & + \vec{\sigma}_{\alpha\gamma} \cdot \vec{\sigma}_{\beta\rho} j(q_1) - \vec{\sigma}_{\alpha\rho} \cdot \vec{\sigma}_{\beta\gamma} j(q_2) \end{aligned}$$

where $\nu(q)$ and $j(q)$ represent the spin-independent and exchange interaction potentials governing the scattering of quasiparticles near the Fermi surface. These potentials, or effective interactions, determine both the thermodynamic and transport Fermi liquid properties of normal ^3He . They also determine the leading order strong coupling corrections to the BCS free energy functional, and thus the relative stability of the A and B phases of superfluid ^3He . Note that Eq. 8.30 assumes that the only spin dependence is that from exchange due to indistinguishable Fermions interacting through a spin-independent potential. The nuclear dipole interaction, a spin-orbit interaction, violates this assumption; however, it is a tiny perturbation compared to the pairing interaction and can be treated perturbatively.

8.3. Frequency dependence of Δ

The Matsubara frequency sums in Φ_{sc} are generally convergent, however they converge at values of ε_n orders of magnitude above the expected weak-coupling cutoff scale $E_c \approx 0.1E_F$. This implies that, were the frequency dependence of the leading weak-coupling

interaction and the order parameter treated self-consistently, then that scale would be provide a frequency cutoff for the Φ_{sc} terms through the frequency dependence of Δ .

While we do not know the exact form of the frequency dependence of the leading pairing interaction, it is reasonable to approximate it as a boson-mediated pairing interaction. We take the pairing interaction with a Lorentzian form. Thus we take the spin-fluctuation mediated pairing interaction to be

$$\begin{aligned} \lambda(\hat{p}, \varepsilon_m; \hat{p}', \varepsilon'_m) &= \lambda(\hat{p} \cdot \hat{p}') \theta(\varepsilon_m, \varepsilon'_m), \\ \theta(\varepsilon_m, \varepsilon'_m) &= \omega_{\text{sf}}^2 / [(\varepsilon_m - \varepsilon'_m)^2 + \omega_{\text{sf}}^2] \end{aligned} \tag{8.31}$$

where the frequency cutoff is determined by the maximum paramagnon energy, $\omega_{\text{sf}} = x_{\text{sf}} E_F (1 + F_0^a)$. The coefficient $x_{\text{sf}} \sim \mathcal{O}(1)$ is pressure independent and determined by fitting to experiment. Treated self-consistently within the weak-coupling free-energy functional, this pairing interaction results in an order parameter that also has a Lorentzian frequency dependence of $\hat{\Delta}(\hat{p}, \varepsilon_m) \approx \hat{\Delta}(\hat{p}) \theta(\varepsilon_m, 0)$. Figure 8.2 shows the frequency dependence of the self-consistent order parameter, and we note that this self-consistent recovery of the form of the pairing interaction is not found for the quartic cutoff used by Sauls and Serene.[80] We therefore treat the order parameter $\hat{\Delta}$ as having this fixed Lorentzian frequency dependence instead of calculating it self-consistently for each individual Matsubara frequency ε_m .

8.4. Experimental Inputs

The material parameters entering the free-energy functional, along with the quasiparticle interaction potentials, must be determined experimentally. For the basic Fermi liquid

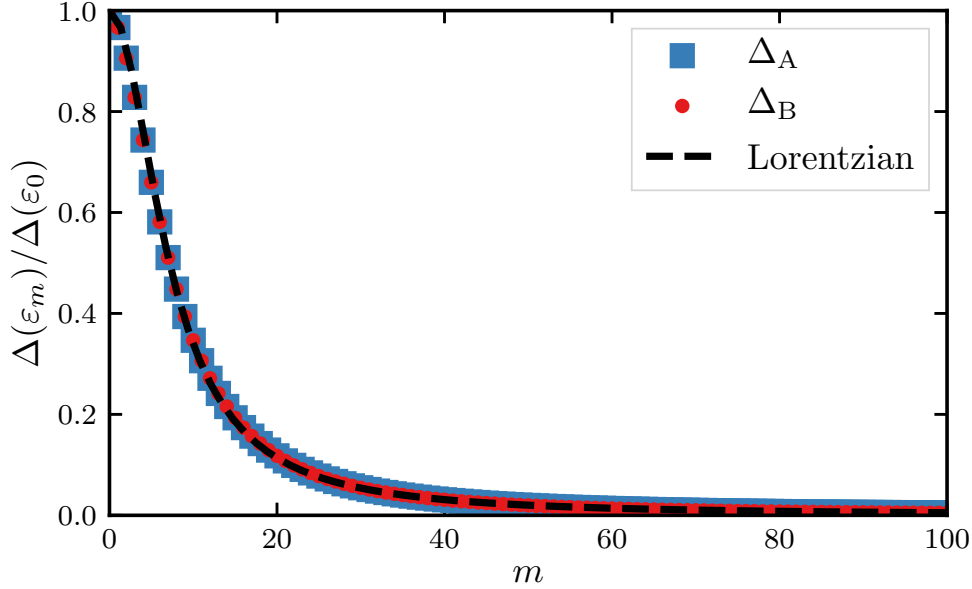


Figure 8.2. The relative order parameter amplitude for the bulk A and B phases as a function of Matsubara index m . The red circles (B phase) and blue squares (A phase) are calculated self-consistently and have nearly identical frequency dependence. The dashed black line is the Lorentzian function with width $\omega_{\text{sf}} = 1.14\omega_{\text{ff}}$ where ω_{ff} is the spectral width of the pairing interaction.

properties, the Fermi momentum p_f , the effective mass m^* , and the molar volume V_m , we use the values found by Greywall[39] but converted to the newer PLTS-2000 temperature scale as described by Goudon in Ref. [36]. This shift in temperature scale results in up to a 5% enhancement of m^* . We also use the magnetic susceptibility measurements, and hence F_0^a , from the Grenoble experiment presented in that paper.[36] The speed of first sound, c_1 , and hence the value of F_0^s , is from the experiment of Ref. [69] with fitting coefficients provided by Ref [41].

Further normal Fermi liquid properties are considered but given far less weight due to significant uncertainties. The Fermi liquid parameter F_2^s , taken from Refs. [56, 42, 30], is found to be most consistent with $F_2^s \approx 0.1$ independent of pressure. We also incorporate

data for three transport measurements: thermal conductivity[**38**], dynamic viscosity[**63**], and spin diffusion[**76**] which constrain angular averages of the T matrix via exact solutions to the Landau-Boltzmann transport equation for these transport properties.[**18**]

We further fit the model to the specific heat jumps of the A and B phase transitions at T_c . For the B phase and the A phase above p_{PCP} we use Greywall's data[**39**] converted to the PLTS-2000 scale. To constrain the A phase specific heat jumps below p_{PCP} , we follow the analysis described by Choi et al[**23**] which uses $g(\beta)$, the g-shift, and the B phase specific heat.

8.5. Quasiparticle interaction potentials

Obtaining a good fit to the experimental input data required a large number of fitting parameters characterizing the potentials $v(q)$ and $j(q)$ appearing in Eq. 8.30 regardless of which polynomial bases or variational functions we tried. We chose to use $l \leq 10$ shifted Legendre polynomials on $q/2k_F \in [0, 1]$ due to their goodness of fit and numerical efficiency. The additional free parameter, the spin fluctuation coefficient, was fixed at all pressures as $x_{\text{sf}} \approx 0.4$. As we do not have enough independent inputs to fully constrain this 21 parameter model, we checked for additional solutions using global optimization; we found no additional minima in the physically reasonable parameter space aside from that reported here. In addition, the overall shape of the potentials was found to be insensitive to small shifts in the key experimental inputs.

Figure 8.3 shows the resulting interaction potentials. The exchange interaction, $-j(q)$, is maximal near $q = 0$, signifying the role of ferromagnetic spin fluctuations. In addition to the ferromagnetic peak we find an additional maximum appearing at the same q value

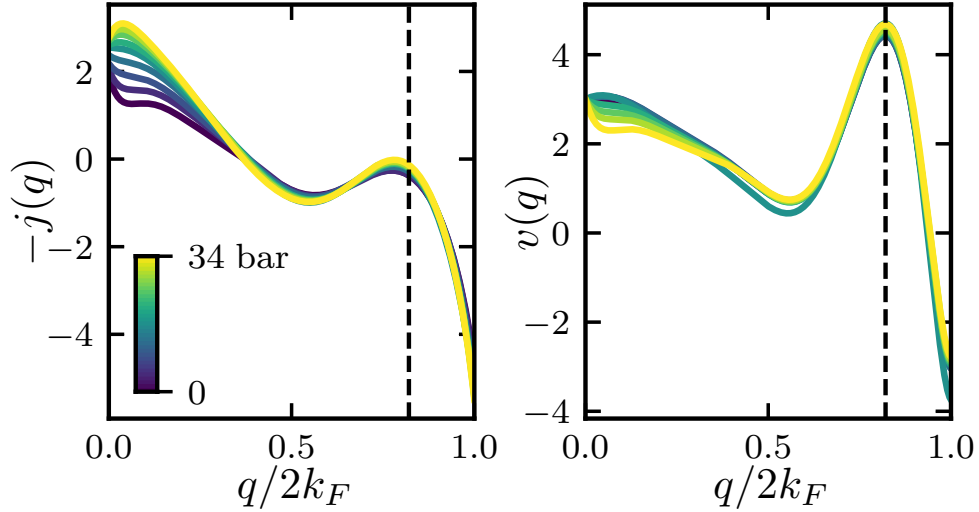


Figure 8.3. The spin-dependent interaction potential $j(q)$ and the spin-independent potential $v(q)$ at pressures from 0 to 34 bar. The curvature variations of the potentials with pressure at small q appear to largely be artifacts of the underconstrained functional forms. The vertical dashed line is the value of q that corresponds to the solid ${}^3\text{He}$ lattice constant at 34 bar.

in both $-j(q)$ and the spin-independent potential $v(q)$. These peaks at a relatively high $q = q_a$ are interpreted as anti-ferromagnetic spin-fluctuation exchange and exchange of long-lived density fluctuations near a Mott transition, respectively. The wave vector, q_a , is found, at the melting pressure 34.4 bar, to match that lattice constant of the anti-ferromagnetic ${}^3\text{He}$ solid,

$$(8.32) \quad q_a = \frac{2\pi}{(2v_a/N_A)^{1/3}} \approx 1.64 k_F,$$

where v_a is the molar volume of the bcc solid ${}^3\text{He}$.^[74] Thus the form of the interaction potentials strongly suggests a link between the interacting ${}^3\text{He}$ Fermi liquid, the strong-coupling stabilization of the A phase, and the anti-ferromagnetic solid phase at higher pressure, which we will discuss further in the Conclusion.

8.6. Specific heat

Having determined the interaction potentials at T_c , we can test the strong-coupling free-energy functional below T_c directly by calculating the superfluid specific heat,

$$(8.33) \quad C - C_N = -T (\partial^2 \Delta\Omega / \partial T^2),$$

as a function of temperature and comparing it to experiment. Evaluating the free-energy functional for the A phase below T_c is particularly challenging, since it is not possible to separate the Matsubara sums from the angular integrals as is the case with the B phase. We implemented the Foam Monte Carlo integration algorithm[44] to accomplish this, the details of which are given in Appendix C.

Figure 8.4 shows a direct comparison at $p = 34$ bar between the temperature dependence of the superfluid specific heat in both A and B phases as measured by Greywall[39], after conversion to the PLTS-2000 temperature scale, and self-consistent calculations using the strong-coupling free-energy functional. The quantitative agreement between theory and experiment is maintained at all pressures and temperatures available. Figure 8.5 shows fractional differences between between our calculation and Greywall's experiment as a function of both temperature and pressure, and demonstrates greater than 95% agreement until $T \approx 0.9$ mK where the thermometry calibration of the experiment is known to be highly uncertain.

We find that, having fit the interaction potentials to our known normal and superfluid properties at T_c , the strong-coupling theory maintains a high degree of accuracy when calculating the specific heat at lower temperatures. While previous work by Sauls, Serene, and Rainer[81, 85] showed a high degree of accuracy in calculating the B phase specific

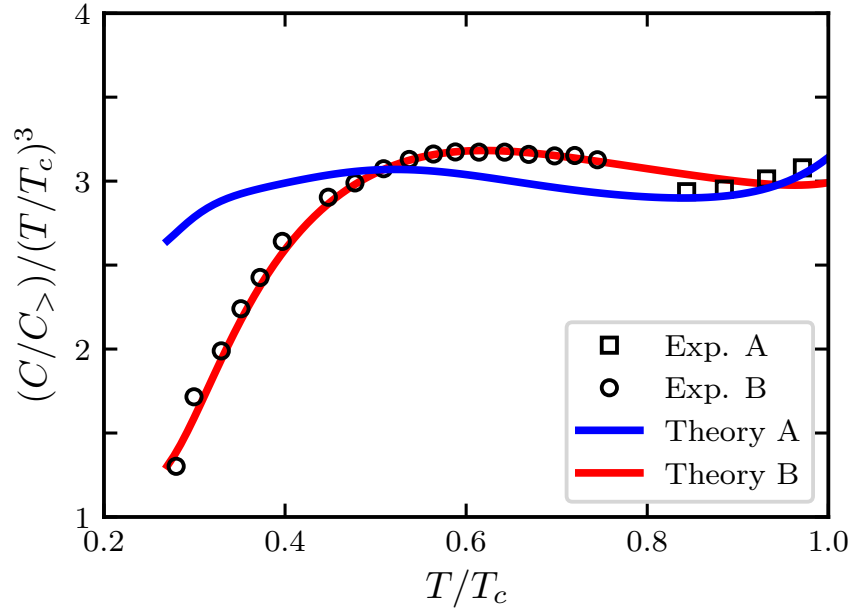


Figure 8.4. Superfluid specific heat as a function of temperature at 34 bar, for both A and B phases, as calculated self-consistently with the strong-coupling free-energy functional (solid lines) and as measured by Greywall[39] (squares and circles).

heat, it did not include the A phase due to numerical difficulty. Here we have shown that the strong-coupling free-energy functional considered is able to accurately reproduce both measured A and B phase specific heat curves.

8.7. Phase diagram

Another key test of the accuracy of the strong-coupling theory is the bulk phase transition line between the A and B phases as a function of temperature and pressure. This T_{AB} is absent in weak-coupling, where only the B phase is stable, and its exact location is extremely sensitive to the relative free energies of the A and B phases. Prior microscopic strong-coupling results have not included this line due to the difficulty of calculating the A phase free-energy below T_c ; however, the T_{AB} line was found to be

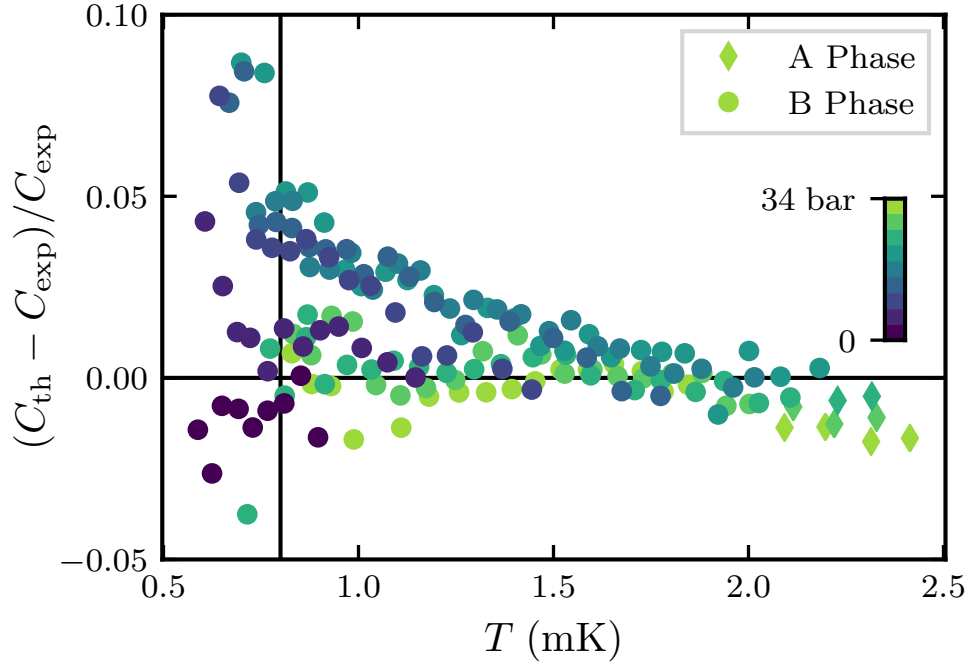


Figure 8.5. Fractional differences between the calculated superfluid specific heat and Greywall’s measurements. For temperatures below the vertical line at $T \sim 0.8$ mK the temperature calibration for the experiment becomes significantly more uncertain.

accurately represented by Ginzburg-Landau theory including both the strong-coupling corrections to the 4th order invariants and their temperature dependence at T_c .**[104]**

We calculate the T_{AB} line through direct comparison of the A and B phase free energies and where they cross. Figure 8.6 shows the bulk phase diagram as measured by Greywall**[39]**, including the measured A-B transition, compared to our calculated T_{AB} line. The agreement is seen to be incredibly good, going from p_{PCP} to the melting pressure at 34.4 bar and capturing the curvature of the T_{AB} line. These results provide strong validation of the effective interaction potentials that determine the strong-coupling corrections to the weak-coupling free energy.

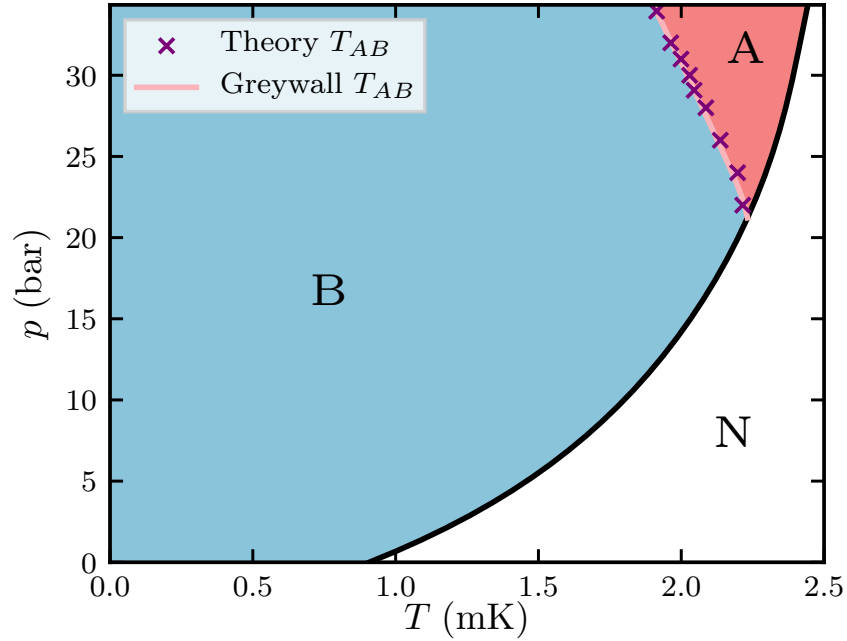


Figure 8.6. Bulk phase diagram adapted from Greywall's measurements[39] and including the self-consistently calculated T_{AB} points.

8.8. Ginzburg-Landau regime

Having shown the accuracy of the strong-coupling free-energy functional for the bulk A and B phases, we can use it to recover the leading corrections to the weak-coupling Ginzburg-Landau theory for ^3He . These corrections appear in the fourth-order β coefficients as[104]

$$(8.34) \quad \beta_i \equiv \beta_i^{\text{wc}} + (T/T_c) \Delta\beta_i^{\text{sc}}.$$

The resulting $\Delta\beta_i^{\text{sc}}$ coefficients are similar to those calculated by Sauls and Serene[81], with the negative $\Delta\beta_5^{\text{sc}}$ dominating at high pressures followed by $\Delta\beta_4^{\text{sc}}$. The theoretical

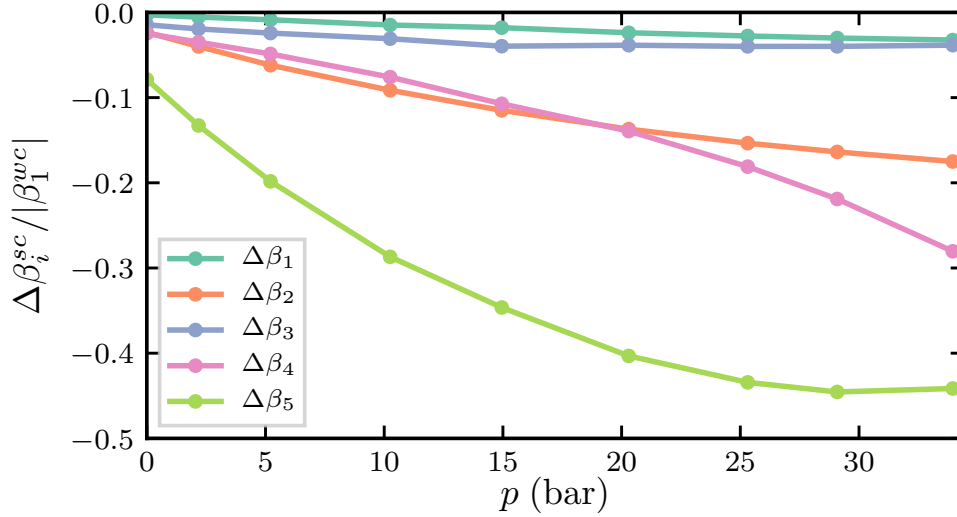


Figure 8.7. Corrections to the fourth-order β coefficients for the ${}^3\text{He}$ Ginzburg-Landau free-energy functional. These corrections are qualitatively similar to those calculated by Sauls and Serene.[**81**]

results for the strong-coupling GL parameters are qualitatively different than that proposed by Choi et al[**23**], which includes positive $\Delta\beta_5^{\text{sc}}$ corrections, shown in Fig. 3.1; these positive corrections are hard, if not impossible, to realize in strong-coupling theory.

8.9. Conclusion

We have obtained extraordinarily good numerical agreement with the measured thermodynamic properties of bulk superfluid ${}^3\text{He}$ using next-to-leading order strong-coupling quasiclassical theory. In particular, this work represents the first accurate quantitative calculation of the T_{AB} line and the A phase specific heat below T_c . Moreover, the quasi-particle interaction potentials necessary for this quantitative accuracy show rich features beyond the ferromagnetic interactions expected from spin-fluctuations. We find that both anti-ferromagnetic and Mott interactions emerge from the fit to our input data,

and that both these interactions exhibit a peak at the same wavevector q_a corresponding the anti-ferromagnetic solid ^3He lattice. The model of superfluid ^3He as an almost localized Fermi liquid was first suggested by Anderson and Brinkman[6] on the basis of its almost pressure-independent F_0^a parameter and strongly pressure dependent effective mass and later expanded by Vollhardt.[92] That significant weight in the interaction potentials is necessarily found at large momentum transfer strongly suggests that the rich phase diagram of ^3He is a product of interactions mediated by both ferromagnetic and anti-ferromagnetic spin-fluctuations, as well as density fluctuations of an almost localized Fermi liquid near a Mott transition.

References

- [1] ABRAMOWITZ, M., AND STEGUN, I. A. *Handbook of Mathematical Functions: With Formulas, Graphs, and Mathematical Tables*. Courier Corporation, 1965.
- [2] ABRIKOSOV, A. A. On the Magnetic Properties of Superconductors of the Second Group. *Sov. Phys. JETP* 5 (1957), 1174.
- [3] ABRIKOSOV, A. A., AND KHALATNIKOV, I. M. The theory of a fermi liquid (the properties of liquid ^3He at low temperatures). *Rep. Prog. Phys.* 22, 1 (1959), 329.
- [4] AGTERBERG, D. F., AND YANG, K. The effect of impurities on Fulde-Ferrell-Larkin-Ovchinnikov superconductors. *J. Phys.: Condens. Matter* 13, 41 (2001), 9259.
- [5] AMBEGAOKAR, V., DEGENNES, P. G., AND RAINER, D. Landau-Ginsburg equations for an anisotropic superfluid. *Phys. Rev. A* 9, 6 (June 1974), 2676–2685.
- [6] ANDERSON, P., AND BRINKMAN, W. *The Helium Liquids*, edited by JGM Armitage and IE Farquhar.
- [7] ANDERSON, P. W., AND BRINKMAN, W. F. Anisotropic Superfluidity in ^3He : A Possible Interpretation of Its Stability as a Spin-Fluctuation Effect. *Phys. Rev. Lett.* 30, 22 (May 1973), 1108–1111.
- [8] ANDERSON, P. W., AND MOREL, P. Generalized Bardeen-Cooper-Schrieffer States and the Proposed Low-Temperature Phase of Liquid ^3He . *Phys. Rev.* 123, 6 (Sept. 1961), 1911–1934.
- [9] AOYAMA, K. Stripe order in superfluid ^3He confined in narrow cylinders. *Phys. Rev. B* 89, 14 (Apr. 2014), 140502.
- [10] ASADCHIKOV, V. E., ASKHADULLIN, R. S., VOLKOV, V. V., DMITRIEV, V. V., KITAEVA, N. K., MARTYNOV, P. N., OSIPOV, A. A., SENIN, A. A., SOLDATOV, A. A., CHEKRYGINA, D. I., AND YUDIN, A. N. Structure and properties of “nematically ordered” aerogels. *Jetp Lett.* 101, 8 (Apr. 2015), 556–561.

- [11] ASKHADULLIN, R. S., DMITRIEV, V. V., KRASNIKHIN, D. A., MARTYNOV, P. N., OSIPOV, A. A., SENIN, A. A., AND YUDIN, A. N. Phase diagram of superfluid ^3He in “nematically ordered” aerogel. *Jetp Lett.* *95*, 6 (May 2012), 326–331.
- [12] AUTTI, S., DMITRIEV, V. V., MÄKINEN, J. T., SOLDATOV, A. A., VOLOVIK, G. E., YUDIN, A. N., ZAVJALOV, V. V., AND ELTSOV, V. B. Observation of Half-Quantum Vortices in Topological Superfluid ^3He . *Phys. Rev. Lett.* *117*, 25 (Dec. 2016), 255301.
- [13] BALIAN, R., AND WERTHAMER, N. R. Superconductivity with Pairs in a Relative p Wave. *Phys. Rev.* *131*, 4 (Aug. 1963), 1553–1564.
- [14] BARTON, G., AND MOORE, M. A. Superfluid ^3He in restricted geometries. *J Low Temp Phys* *21*, 5-6 (Dec. 1975), 489–515.
- [15] BENNETT, R. G., ZHELEV, N., SMITH, E. N., POLLANEN, J., HALPERIN, W. P., AND PARPIA, J. M. Modification of the ^3He Phase Diagram by Anisotropic Disorder. *Phys. Rev. Lett.* *107*, 23 (Nov. 2011), 235504.
- [16] BRINKMAN, W. F., SERENE, J. W., AND ANDERSON, P. W. Spin-fluctuation stabilization of anisotropic superfluid states. *Phys. Rev. A* *10*, 6 (Dec. 1974), 2386–2394.
- [17] BRINKMAN, W. F., AND SMITH, H. Large angle tipping frequency shifts in pulsed NMR for ^3He (B). *Physics Letters A* *53*, 1 (May 1975), 43–44.
- [18] BROOKER, G. A., AND SYKES, J. Transport Properties of a Fermi Liquid. *Phys. Rev. Lett.* *21*, 5 (July 1968), 279–282.
- [19] BRUINSMA, R., AND MAKI, K. Textures in narrow cylinders in superfluid ^3He -A. *J Low Temp Phys* *37*, 5-6 (Dec. 1979), 607–625.
- [20] BUCHHOLTZ, L. J., AND FETTER, A. L. Textures in superfluid ^3He -A: Hydrodynamic and magnetic effects in a cylindrical pore. *Phys. Rev. B* *15*, 11 (June 1977), 5225–5239.
- [21] BUCHHOLTZ, L. J., AND ZWICKNAGL, G. Identification of p -wave superconductors. *Phys. Rev. B* *23*, 11 (June 1981), 5788–5796.
- [22] BUNKOV, Y. M., AND VOLOVIK, G. E. On the Possibility of the Homogeneously Precessing Domain in Bulk ^3He -A. *EPL* *21*, 8 (1993), 837.

- [23] CHOI, H., DAVIS, J. P., POLLANEN, J., HAARD, T. M., AND HALPERIN, W. P. Strong coupling corrections to the Ginzburg-Landau theory of superfluid ^3He . *Phys. Rev. B* *75*, 17 (May 2007), 174503.
- [24] CHOI, H. C., GRAY, A. J., VICENTE, C. L., XIA, J. S., GERVAIS, G., HALPERIN, W. P., MULDER, N., AND LEE, Y. A_1 and A_2 Transitions in Superfluid ^3He in 98% Porosity Aerogel. *Phys. Rev. Lett.* *93*, 14 (Oct. 2004), 145302.
- [25] CHUNG, S. B., AND ZHANG, S.-C. Detecting the Majorana Fermion Surface State of ^3He -B through Spin Relaxation. *Phys. Rev. Lett.* *103*, 23 (Dec. 2009), 235301.
- [26] DE GENNES, P. G., AND RAINER, D. Alignment of anisotropic superfluids by flow. *Physics Letters A* *46*, 7 (Feb. 1974), 429–430.
- [27] DMITRIEV, V. V., ELTSOV, V. B., KRUSIUS, M., RUOHIO, J. J., AND VOLOVIK, G. E. Superflow-stabilized nonlinear NMR in rotating $^3\text{He} - b$. *Phys. Rev. B* *59*, 1 (Jan. 1999), 165–168.
- [28] DMITRIEV, V. V., KRASNIKHIN, D. A., MULDER, N., SENIN, A. A., VOLOVIK, G. E., AND YUDIN, A. N. Orbital glass and spin glass states of ^3He -A in aerogel. *Jetp Lett.* *91*, 11 (June 2010), 599–606.
- [29] DMITRIEV, V. V., SENIN, A. A., SOLDATOV, A. A., AND YUDIN, A. N. Polar Phase of Superfluid ^3He in Anisotropic Aerogel. *Phys. Rev. Lett.* *115*, 16 (Oct. 2015), 165304.
- [30] ENGEL, B. N., AND IHAS, G. G. Velocity of Longitudinal Sound and F_2^s in Liquid ^3He . *Phys. Rev. Lett.* *55*, 9 (Aug. 1985), 955–958.
- [31] FAY, D., AND LAYZER, A. Superfluidity of Low-Density Fermion Systems. *Phys. Rev. Lett.* *20*, 5 (Jan. 1968), 187–190.
- [32] FETTER, A. L., AND ULLAH, S. Superfluid density and critical current of ^3He in confined geometries. *J Low Temp Phys* *70*, 5-6 (Mar. 1988), 515–535.
- [33] FOMIN, I. A. Solution of spin dynamics equations for ^3He superfluid phases in a strong magnetic field. *J Low Temp Phys* *31*, 3-4 (May 1978), 509–526.
- [34] FREEMAN, M. R., GERMAIN, R. S., THUNEBERG, E. V., AND RICHARDSON, R. C. Size effects in thin films of superfluid ^3He . *Phys. Rev. Lett.* *60*, 7 (Feb. 1988), 596–599.

- [35] GONZÁLEZ, M., ZHENG, P., GARCELL, E., LEE, Y., AND CHAN, H. B. Comb-drive micro-electro-mechanical systems oscillators for low temperature experiments. *Review of Scientific Instruments* 84, 2 (Feb. 2013), 025003.
- [36] GOUDON, V. *Magnétisme nucléaire de l'³He liquide : nouvelle détermination du paramètre de Landau F0a*. PhD thesis, Université Joseph-Fourier - Grenoble I, Oct. 2006.
- [37] GOULD, C. M., AND LEE, D. M. Superfluid ³He in Narrow Cylinders. *Phys. Rev. Lett.* 41, 14 (Oct. 1978), 967–970.
- [38] GREYWALL, D. S. Thermal conductivity of normal liquid ³He. *Phys. Rev. B* 29, 9 (May 1984), 4933–4945.
- [39] GREYWALL, D. S. ³He specific heat and thermometry at millikelvin temperatures. *Phys. Rev. B* 33, 11 (June 1986), 7520–7538.
- [40] HAGER, W. W., AND ZHANG, H. Algorithm 851: CG_DESCENT, a Conjugate Gradient Method with Guaranteed Descent. *ACM Trans. Math. Softw.* 32, 1 (Mar. 2006), 113–137.
- [41] HALPERIN, W. P., AND VAROQUAUX, E. CHAPTER 7 - Order-Parameter Collective Modes in Superfluid ³He. In *Modern Problems in Condensed Matter Sciences*, W. P. Halperin and L. P. Pitaevskii, Eds., vol. 26 of *Helium Three*. Elsevier, Jan. 1990, pp. 353–522.
- [42] HAMOT, P. J., LEE, Y., SPRAGUE, D. T., HAARD, T. M., KYCIA, J. B., RAND, M. R., AND HALPERIN, W. P. First- and zero-sound velocity and fermi liquid parameter f_2^s in liquid ³He determined by a path length modulation technique. *J Low Temp Phys* 99, 5 (June 1995), 651–658.
- [43] HOLMVALL, P., VORONTSOV, A. B., FOGELSTRÖM, M., AND LÖFWANDER, T. Broken translational symmetry at edges of high-temperature superconductors. *Nature Communications* 9, 1 (June 2018), 2190.
- [44] JADACH, S. Foam: A general-purpose cellular Monte Carlo event generator. *Computer Physics Communications* 152, 1 (Apr. 2003), 55–100.
- [45] KJÄLDMAN, L. H., KURKIJÄRVI, J., AND RAINER, D. Suppression of p -wave superfluidity in long, narrow pores. *J Low Temp Phys* 33, 5-6 (Dec. 1978), 577–587.

- [46] KUNIMATSU, T., NEMA, H., ISHIGURO, R., KUBOTA, M., TAKAGI, T., SASAKI, Y., AND ISHIKAWA, O. Textures of Rotating Superfluid ^3He -A in a Single Narrow Cylinder. *J Low Temp Phys* 171, 3-4 (May 2013), 280–286.
- [47] LAYZER, A., AND FAY, D. Spin fluctuation exchange: Mechanism for a superfluid transition in liquid ^3He . *Solid State Communications* 15, 3 (Aug. 1974), 599–603.
- [48] LEGGETT, A. J. Interpretation of Recent Results on ^3He below 3 mK: A New Liquid Phase? *Phys. Rev. Lett.* 29, 18 (Oct. 1972), 1227–1230.
- [49] LEGGETT, A. J. A theoretical description of the new phases of liquid ^3He . *Rev. Mod. Phys.* 47, 2 (Apr. 1975), 331–414.
- [50] LEVITIN, L. V., BENNETT, R. G., CASEY, A., COWAN, B., SAUNDERS, J., DRUNG, D., SCHURIG, T., AND PARPIA, J. M. Phase Diagram of the Topological Superfluid ^3He Confined in a Nanoscale Slab Geometry. *Science* 340, 6134 (May 2013), 841–844.
- [51] LEVITIN, L. V., BENNETT, R. G., SUROVTSEV, E. V., PARPIA, J. M., COWAN, B., CASEY, A. J., AND SAUNDERS, J. Surface-Induced Order Parameter Distortion in Superfluid ^3He -B Measured by Nonlinear NMR. *Phys. Rev. Lett.* 111, 23 (Dec. 2013), 235304.
- [52] LEVITIN, L. V., YAGER, B., SUMNER, L., COWAN, B., CASEY, A. J., ZHELEV, N., BENNETT, R. G., PARPIA, J. M., AND SAUNDERS, A. J. Evidence for a Spatially-Modulated Superfluid Phase of ^3He under Confinement. *arXiv:1805.02053 [cond-mat]* (May 2018).
- [53] LI, Y.-H., AND HO, T.-L. Superfluid ^3He in very confined regular geometries. *Phys. Rev. B* 38, 4 (Aug. 1988), 2362–2370.
- [54] MAKI, K. Planar textures in superfluid ^3He -A. *J Low Temp Phys* 32, 1-2 (July 1978), 1–17.
- [55] MASUDA, H., AND FUKUDA, K. Ordered Metal Nanohole Arrays Made by a Two-Step Replication of Honeycomb Structures of Anodic Alumina. *Science* 268, 5216 (June 1995), 1466–1468.
- [56] MATSUMOTO, K., IKEGAMI, T., ITO, S., KIRIGAYA, M., AND OKUDA, Y. Zero and first sound velocity and Fermi liquid parameter F_2 in normal ^3He . *J Low Temp Phys* 102, 1 (Jan. 1996), 227–235.

- [57] MERMIN, N. D., AND HO, T.-L. Circulation and Angular Momentum in the A Phase of Superfluid Helium-3. *Phys. Rev. Lett.* *36*, 11 (Mar. 1976), 594–597.
- [58] MIZUSHIMA, T. Superfluid ^3He in a restricted geometry with a perpendicular magnetic field. *Phys. Rev. B* *86*, 9 (Sept. 2012), 094518.
- [59] MIZUSHIMA, T., AND MACHIDA, K. Effects of Majorana Edge Fermions on Dynamical Spin Susceptibility in Topological Superfluid $^3\text{He-B}$. *J Low Temp Phys* *162*, 3-4 (Feb. 2011), 204–211.
- [60] MIZUSHIMA, T., AND SAULS, J. A. Bosonic Surface States and Acoustic Spectroscopy of Confined Superfluid $^3\text{He-B}$. *arXiv:1801.02277 [cond-mat]* (Jan. 2018).
- [61] MIZUSHIMA, T., TSUTSUMI, Y., KAWAKAMI, T., SATO, M., ICHIOKA, M., AND MACHIDA, K. Symmetry-Protected Topological Superfluids and Superconductors —From the Basics to 3 —. *J. Phys. Soc. Jpn.* *85*, 2 (Jan. 2016), 022001.
- [62] NAGATO, Y., YAMAMOTO, M., AND NAGAI, K. Rough Surface Effects on the p-Wave Fermi Superfluids. *Journal of Low Temperature Physics* *110*, 5-6 (Mar. 1998), 1135–1171.
- [63] NAKAGAWA, M., MATSUBARA, A., ISHIKAWA, O., HATA, T., AND KODAMA, T. Viscosity measurements in normal and superfluid ^3He . *Phys. Rev. B* *54*, 10 (Sept. 1996), R6849–R6852.
- [64] NOCEDAL, J. Updating quasi-Newton matrices with limited storage. *Math. Comp.* *35*, 151 (1980), 773–782.
- [65] NOCEDAL, J., AND WRIGHT, S. *Numerical Optimization*, 2 ed. Springer Series in Operations Research and Financial Engineering. Springer-Verlag, New York, 2006.
- [66] NOMURA, R., MURAKAWA, S., WASAI, M., AKIYAMA, K., NAKAO, T., AND OKUDA, Y. Surface Majorana cone of the topological superfluid $^3\text{He B}$ phase. *Physica E: Low-dimensional Systems and Nanostructures* *55* (Jan. 2014), 42–47.
- [67] OSHEROFF, D. D., GULLY, W. J., RICHARDSON, R. C., AND LEE, D. M. New Magnetic Phenomena in Liquid ^3He below 3 mK. *Phys. Rev. Lett.* *29*, 14 (Oct. 1972), 920–923.
- [68] OSHEROFF, D. D., RICHARDSON, R. C., AND LEE, D. M. Evidence for a New Phase of Solid ^3He . *Phys. Rev. Lett.* *28*, 14 (Apr. 1972), 885–888.

- [69] PAULSON, D. N. *Collisionless Sound and Static Magnetization in Superfluid HELIUM-3*. PhD thesis, University of California, San Diego, 1974.
- [70] POLLANEN, J., LI, J. I. A., COLLETT, C. A., GANNON, W. J., AND HALPERIN, W. P. Identification of Superfluid Phases of ^3He in Uniformly Isotropic 98.2% Aerogel. *Phys. Rev. Lett.* *107*, 19 (Oct. 2011), 195301.
- [71] POLLANEN, J., LI, J. I. A., COLLETT, C. A., GANNON, W. J., HALPERIN, W. P., AND SAULS, J. A. New chiral phases of superfluid ^3He stabilized by anisotropic silica aerogel. *Nature Physics* *8*, 4 (Apr. 2012), 317–320.
- [72] RAINER, D., AND SERENE, J. W. Free energy of superfluid ^3He . *Phys. Rev. B* *13*, 11 (June 1976), 4745–4765.
- [73] RAINER, D., AND VUORIO, M. Small objects in superfluid ^3He . *J. Phys. C: Solid State Phys.* *10*, 16 (1977), 3093.
- [74] ROGER, M., HETHERINGTON, J. H., AND DELRIEU, J. M. Magnetism in solid ^3He . *Rev. Mod. Phys.* *55*, 1 (Jan. 1983), 1–64.
- [75] ROJAS, X., AND DAVIS, J. P. Superfluid nanomechanical resonator for quantum nanofluidics. *Phys. Rev. B* *91*, 2 (Jan. 2015), 024503.
- [76] SACHRAJDA, A. S., BREWER, D. F., AND TRUSCOTT, W. S. Measurements of the spin diffusion coefficient of normal ^3He in bulk liquid and a restricted geometry. *J Low Temp Phys* *56*, 5 (Sept. 1984), 617–631.
- [77] SAULS, J. A. Surface states, edge currents, and the angular momentum of chiral p -wave superfluids. *Phys. Rev. B* *84*, 21 (Dec. 2011), 214509.
- [78] SAULS, J. A. Chiral phases of superfluid ^3He in an anisotropic medium. *Phys. Rev. B* *88*, 21 (Dec. 2013), 214503.
- [79] SAULS, J. A., AND MIZUSHIMA, T. On the Nambu fermion-boson relations for superfluid ^3He . *Phys. Rev. B* *95*, 9 (Mar. 2017), 094515.
- [80] SAULS, J. A., AND SERENE, J. W. Higher order strong-coupling effects in superfluid ^3He . *Physica B+C* *108*, 1 (Aug. 1981), 1137–1138.
- [81] SAULS, J. A., AND SERENE, J. W. Potential-scattering models for the quasiparticle interactions in liquid ^3He . *Phys. Rev. B* *24*, 1 (July 1981), 183–189.

- [82] SAULS, J. A., AND SHARMA, P. Impurity effects on the A_1-A_2 splitting of superfluid ^3He in aerogel. *Phys. Rev. B* 68, 22 (Dec. 2003), 224502.
- [83] SAUNDERS, J., BETTS, D. S., BREWER, D. F., SWITHEBY, S. J., AND TRUSCOTT, W. S. Observations on Superfluid $^3\text{He-A}$ in Small Cylinders: Evidence for a Textural Transition. *Phys. Rev. Lett.* 40, 19 (May 1978), 1278–1281.
- [84] SCHECHTER, A. M. R., SIMMONDS, R. W., PACKARD, R. E., AND DAVIS, J. C. Observation of ‘third sound’ in superfluid ^3He . *Nature* 396, 6711 (Dec. 1998), 554–557.
- [85] SERENE, J. W., AND RAINER, D. Comment on the specific heat of superfluid ^3He . *J Low Temp Phys* 34, 5-6 (Mar. 1979), 589–594.
- [86] SERENE, J. W., AND RAINER, D. The quasiclassical approach to superfluid ^3He . *Physics Reports* 101, 4 (Dec. 1983), 221–311.
- [87] SHEWCHUK, J. R. Triangle: Engineering a 2D quality mesh generator and Delaunay triangulator. In *Applied Computational Geometry Towards Geometric Engineering* (May 1996), Lecture Notes in Computer Science, Springer, Berlin, Heidelberg, pp. 203–222.
- [88] SUROVTSEV, E. V., AND FOMIN, I. A. Model Calculation of Orientational Effect of Deformed Aerogel on the Order Parameter of Superfluid ^3He . *J Low Temp Phys* 150, 3-4 (Feb. 2008), 487–492.
- [89] TAKAGI, T. A-B Phase Transition of Superfluid ^3He Confined in Pore Geometry. *Prog Theor Phys* 78, 3 (Sept. 1987), 562–572.
- [90] THUNEBERG, E. V. Nucleation of superconductivity around weakly scattering defects. *J Low Temp Phys* 62, 1 (Jan. 1986), 27–37.
- [91] THUNEBERG, E. V. Ginzburg-Landau theory of vortices in superfluid $^3\text{He-B}$. *Phys. Rev. B* 36, 7 (Sept. 1987), 3583–3597.
- [92] VOLLHARDT, D. Normal ^3He : An almost localized Fermi liquid. *Rev. Mod. Phys.* 56, 1 (Jan. 1984), 99–120.
- [93] VOLLHARDT, D., AND WOELFLE, P. *The Superfluid Phases Of Helium 3*. CRC Press, London ; New York, July 1990.
- [94] VOLOVIK, G. E. *The Universe in a Helium Droplet*. Clarendon Press, Mar. 2003.

- [95] VOLOVIK, G. E., AND ZUBKOV, M. A. Nambu sum rule and the relation between the masses of composite Higgs bosons. *Phys. Rev. D* *87*, 7 (Apr. 2013), 075016.
- [96] VORONTSOV, A., AND SAULS, J. A. Domain Walls in Superfluid $^3\text{He-B}$. *J Low Temp Phys* *138*, 1-2 (Jan. 2005), 283–288.
- [97] VORONTSOV, A. B. Andreev bound states in superconducting films and confined superfluid ^3He . *Phil. Trans. R. Soc. A* *376*, 2125 (Aug. 2018), 20150144.
- [98] VORONTSOV, A. B., AND SAULS, J. A. Thermodynamic properties of thin films of superfluid $^3\text{He-A}$. *Phys. Rev. B* *68*, 6 (Aug. 2003), 064508.
- [99] VORONTSOV, A. B., AND SAULS, J. A. Crystalline Order in Superfluid ^3He Films. *Phys. Rev. Lett.* *98*, 4 (Jan. 2007), 045301.
- [100] WALMSLEY, P. M., AND GOLOV, A. I. Chirality of Superfluid $^3\text{He-A}$. *Phys. Rev. Lett.* *109*, 21 (Nov. 2012), 215301.
- [101] WHEATLEY, J. C. Experimental properties of superfluid ^3He . *Rev. Mod. Phys.* *47*, 2 (Apr. 1975), 415–470.
- [102] WHEATLEY, J. C., VILCHES, O. E., AND ABEL, W. R. Principles and methods of dilution refrigeration. *Physics Physique Fizika* *4*, 1 (Aug. 1968), 1–64.
- [103] WIMAN, J. J., AND SAULS, J. A. Superfluid Phases of ^3He in a Periodic Confined Geometry. *J Low Temp Phys* *175*, 1-2 (Apr. 2014), 17–30.
- [104] WIMAN, J. J., AND SAULS, J. A. Superfluid phases of ^3He in nanoscale channels. *Phys. Rev. B* *92*, 14 (Oct. 2015), 144515.
- [105] WIMAN, J. J., AND SAULS, J. A. Strong-Coupling and the Stripe Phase of ^3He . *J Low Temp Phys* *184*, 5-6 (Sept. 2016), 1054–1070.
- [106] WU, H., AND SAULS, J. A. Majorana excitations, spin and mass currents on the surface of topological superfluid $^3\text{He-B}$. *Phys. Rev. B* *88*, 18 (Nov. 2013), 184506.
- [107] XU, J., AND CROOKER, B. C. Very thin films of ^3He : A new phase. *Phys. Rev. Lett.* *65*, 24 (Dec. 1990), 3005–3008.
- [108] ZHELEV, N., BENNETT, R., ILIC, R., PARPIA, J., LEVITIN, L., CASEY, A., AND SAUNDERS, J. Nanofabricated cells for confined ^3He . In *APS Meeting Abstracts*. Z22.003, Mar. 2013.

- [109] ZHELEV, N., BENNETT, R. G., SMITH, E. N., POLLANEN, J., HALPERIN, W. P., AND PARPIA, J. M. Dissipation signatures of the normal and superfluid phases in torsion pendulum experiments with ^3He in aerogel. *Phys. Rev. B* *89*, 9 (Mar. 2014), 094513.
- [110] ZIENKIEWICZ, O. C., TAYLOR, R. L., AND ZHU, J. Z. *The Finite Element Method: Its Basis and Fundamentals*, 6 edition ed. Butterworth-Heinemann, Amsterdam, May 2005.

APPENDIX A

Strong-coupling diagrams

The diagrams (b) through (h) of Fig. 8.1 that make up $\Delta\Phi_{\text{sc}}[\widehat{\Delta}]$ for the bulk A phase are described in this appendix; the B phase follows the same form as the weak-coupling plus model studied by Serene and Rainer.[85] The angular integrals are formulated as in Rainer and Serene[72] where the vertex T is defined as

$$(A.1) \quad T_{\alpha\beta,\gamma\rho} \equiv T^{(s)} \delta_{\alpha\rho} \delta_{\beta\gamma} + T^{(a)} (\vec{\sigma})_{\alpha\rho} \cdot (\vec{\sigma})_{\beta\gamma}.$$

The spin-symmetric and spin-antisymmetric components are given, respectively, by

$$(A.2) \quad \begin{aligned} T^{(s)}(q_1, q_2) &= \frac{1}{4} \left\{ 4v(q_1) - 2v(q_2) - 6j(q_2) \right\} \\ T^{(a)}(q_1, q_2) &= \frac{1}{4} \left\{ 4j(q_1) + 2j(q_2) - 2v(q_2) \right\}. \end{aligned}$$

We use the Abrikosov-Khalatnikov[3] angles to integrate the resulting terms in the free-energy functional. These angles, θ and ϕ , relate to the momentum transfers as

$$(A.3) \quad \begin{aligned} q_1 &\equiv |\hat{p}_1 - \hat{p}_3| = k_f \{ |\cos\theta - 1| |\cos\phi - 1| \}^{1/2} \\ q_2 &\equiv |\hat{p}_1 - \hat{p}_4| = k_f \{ |\cos\theta - 1| |\cos\phi + 1| \}^{1/2}. \end{aligned}$$

For diagrams (d) and (e) we also must define two additional angles[72]

$$(A.4) \quad \begin{aligned} \cos \theta' &= \cos \phi - \cos^2(\theta/2)(\cos \phi + 1) \\ \cos \phi' &= \frac{3 \cos^2(\theta/2) - 1 - [\cos^2(\theta/2) - 1] \cos \phi}{\cos^2(\theta/2) + 1 + [\cos^2(\theta/2) - 1] \cos \phi} . \end{aligned}$$

The A phase order parameter is separated into

$$(A.5) \quad \Delta_A(\hat{p}, \varepsilon_n) = \Delta \theta(\varepsilon_n) \omega(\hat{p})$$

where the amplitude Δ is taken to be both real and positive and $\omega(\hat{p}) = \hat{p}_x + i\hat{p}_y$. We define the following convenience functions related to the scalar pieces of the quasiclassical propagators,

$$(A.6) \quad \begin{aligned} f^i &\equiv \frac{\Delta \theta(\varepsilon_{n_i})}{\sqrt{\varepsilon_{n_i}^2 + |\Delta \theta(\varepsilon_{n_i})|^2 [1 - (\hat{p}_i \cdot \hat{z})^2]}} \\ g_S^i &\equiv \frac{\varepsilon_{n_i}}{\sqrt{\varepsilon_{n_i}^2 + |\Delta \theta(\varepsilon_{n_i})|^2 [1 - (\hat{p}_i \cdot \hat{z})^2]}} - \text{sgn}(\varepsilon_{n_i}) \\ g_N^i &\equiv \text{sgn}(\varepsilon_{n_i}) \end{aligned}$$

The prefactors, summations, and integrations are identical for each diagram considered, so we separate out the innermost integrand φ_{sc} as

$$(A.7) \quad \begin{aligned} \Delta \Phi_{\text{sc}}[\hat{\Delta}] &= -\frac{\pi^4 N(0) T^3}{8 T_f} \sum_{\varepsilon_{n_1}} \sum_{\varepsilon_{n_2}} \sum_{\varepsilon_{n_3}} \int \frac{\Omega_1}{4\pi} \int \frac{\Omega_2}{4\pi} \int \frac{\Omega_3}{4\pi} \delta(|\hat{p}_1 + \hat{p}_2 - \hat{p}_3| - 1) \\ &\times \varphi_{\text{sc}}[\Delta; \hat{p}_1, \varepsilon_{n_1}; \hat{p}_2, \varepsilon_{n_2}; \hat{p}_3, \varepsilon_{n_3}; \hat{p}_1 + \hat{p}_2 - \hat{p}_3, \varepsilon_{n_1} + \varepsilon_{n_2} - \varepsilon_{n_3}] . \end{aligned}$$

Finally, the individual diagrams are then given by

$$(A.8) \quad \varphi_b = \frac{1}{2} ([T^{(s)}(\theta, \phi)]^2 + 3 [T^{(a)}(\theta, \phi)]^2) g_S^1 g_S^2 g_N^3 g_N^4$$

$$(A.9) \quad \varphi_c = ([T^{(s)}(\theta, \phi)]^2 + 3 [T^{(a)}(\theta, \phi)]^2) g_S^1 g_N^2 g_S^3 g_N^4$$

$$(A.10) \quad \begin{aligned} \varphi_d = & -2 [T^{(s)}(\theta, \phi)T^{(s)}(\theta', \phi') + T^{(a)}(\theta, \phi)T^{(a)}(\theta', \phi')] \\ & \times \omega^*(\hat{p}_2)\omega(\hat{p}_4) g_S^1 f^2 g_N^3 f^4 \end{aligned}$$

$$(A.11) \quad \varphi_e = - [T^{(s)}(\theta, \phi)T^{(s)}(\theta', \phi') + T^{(a)}(\theta, \phi)T^{(a)}(\theta', \phi')] g_S^1 g_S^2 g_N^3 g_S^4$$

$$(A.12) \quad \begin{aligned} \varphi_f = & -\frac{1}{4} ([T^{(s)}(\theta, \phi)]^2 + 3 [T^{(a)}(\theta, \phi)]^2) \omega^*(\hat{p}_1)\omega^*(\hat{p}_2)\omega(\hat{p}_3)\omega(\hat{p}_4) \\ & \times f^1 f^2 f^3 f^4 \end{aligned}$$

$$(A.13) \quad \varphi_g = ([T^{(s)}(\theta, \phi)]^2 + 3 [T^{(a)}(\theta, \phi)]^2) \omega^*(\hat{p}_2)\omega(\hat{p}_4) g_S^1 f^2 g_S^3 f^4$$

$$(A.14) \quad \varphi_h = \frac{1}{4} ([T^{(s)}(\theta, \phi)]^2 + 3 [T^{(a)}(\theta, \phi)]^2) g_S^1 g_S^2 g_S^3 g_S^4.$$

APPENDIX B

Numerical Optimization with L-BFGS

Minimizing the Ginzburg-Landau free-energy functional is an example of a nonlinear optimization problem. Given a function

$$(B.1) \quad f(\vec{x}) : \mathbb{R}^N \rightarrow \mathbb{R},$$

we want to find \vec{x} such that $\nabla f(\vec{x}) = 0$.

Numerically, we treat this as an iterative procedure in which at each iteration k $f(\vec{x}_{k+1})$ is expanded as

$$(B.2) \quad f(\vec{x}_{k+1}) \equiv f(\vec{x}_k + \alpha \hat{p})$$

$$(B.3) \quad \approx f_k + \nabla f_k^T \alpha \hat{p} + \frac{1}{2} \alpha^2 \hat{p}^T \mathbf{B}_k \hat{p} + \mathcal{O}(\alpha^3),$$

where a direction \hat{p}_k and step length α_k must be chosen to update \vec{x} and \mathbf{B}_k is the Hessian matrix

$$(B.4) \quad [\mathbf{B}_k]_{ij} = \partial_i \partial_j f(\vec{x}_k).$$

Newton's method explicitly minimizes Eq. B.3 with

$$(B.5) \quad \alpha \hat{p} = -\mathbf{B}_k^{-1} \nabla f_k.$$

The downside of this solution is that it involves \mathbf{B}_k^{-1} , which requires both the computation of all second partial derivatives of f and also solving a linear system to recover \hat{p} . To avoid dealing with \mathbf{B}_k^{-1} , Quasi-Newton methods use various approximations to eliminate the computation of second derivatives and the additional matrix inversion problem.

Nocedal and Wright[65] describe in a great detail a number of Quasi-Newton and related methods, along with pseudocode and mathematical proofs for convergence. For the Ginzburg-Landau solvers used starting with Chapter 3 in this thesis we used the algorithm Limited-memory BFGS (L-BFGS), related to the Broyden–Fletcher–Goldfarb–Shanno algorithm.[64]

It is typical with Quasi-Newton methods, which return a vector \vec{p} , to refine final step size α through a linesearch method that minimizes $f(\vec{x}_k + \alpha\vec{p})$ with respect to α . These linesearch methods typically combine secant methods and solution bracketing.[65]

Included below is Python 3.4 and numpy code demonstrating the implementation of the L-BFGS two-loop recursion algorithm[65] as well as a minimal linesearch with both a secant step and bracketing. The code also includes a test problem to show how the linesearch and L-BFGS portions are deployed.

```

1 from numpy import *
2
3
4 def _ip(x, y):
5     return sum(
6         real(
7             x.conj() * y
8         )
9     )
10
11
12 class LBFGS:
13
14     def __init__(self, m_max):
15         self._m_max = m_max # maximum memory
16
17         self._m = 0 # current memory size
18         self._mi = 0 # current index into memory
19
20         # saved state, to be set on first run
21         self._s = None # vector s ~ [m_max * n_dim]
22         self._y = None # vector y ~ [m_max * n_dim]
23         self._rho = None # vector rho ~ [m_max]
24         self._alpha = None # vector alpha ~ [m_max]
25
26         self.last_x = None # store last x
27         self.last_gx = None # store last gx
28
29         # search direction, is returned
30         self.p = None # search direction
31
32     def update(self, x, gx):
33         if self._s is None:
34             # initialize on first iteration, return gradient
35             self._s = zeros((self._m_max,) + x.shape)
36             self._y = zeros((self._m_max,) + x.shape)
37             self._rho = zeros((self._m_max))
38             self._alpha = zeros((self._m_max))
39
40             self.last_x = copy(x)
41             self.last_gx = copy(gx)

```

```

42 |         self.p = - copy(gx)
43 |         return self.p
44 |
45 |     # add last iteration to memory vectors
46 |     k = self._mi
47 |     self._s[k, :] = x - self.last_x
48 |     self._y[k, :] = gx - self.last_gx
49 |     self._rho[k] = 1. / _ip(self._s[k], self._y[k])
50 |     self.p[:] = gx[:]
51 |
52 |     self.last_x[:] = x[:]
53 |     self.last_gx[:] = gx[:]
54 |
55 |     # first loop, reverse
56 |     for k0 in range(self._m):
57 |         if self._mi < k0:
58 |             k = self._mi + self._m - k0
59 |         else:
60 |             k = self._mi - k0
61 |
62 |             self._alpha[k] = self._rho[k] \
63 |                 * _ip(self._s[k], self.p)
64 |             self.p -= self._alpha[k] * self._y[k]
65 |
66 |     # scale factor (H_k^0)
67 |     gamma = 1. / self._rho[self._mi] / \
68 |         _ip(self._y[self._mi], self._y[self._mi])
69 |     self.p *= gamma
70 |
71 |     # second loop, forward
72 |     for k0 in range(self._m):
73 |         if self._mi + k0 + 1 < self._m:
74 |             k = k0 + self._mi + 1
75 |         else:
76 |             k = k0 + self._mi + 1 - self._m
77 |
78 |             beta = self._rho[k] * _ip(self._y[k], self.p)
79 |             self.p += (self._alpha[k] - beta) * self._s[k]
80 |
81 |     # memory index update
82 |     if self._m < self._m_max:

```

```

83         self._m += 1
84         self._mi = (self._mi + 1) % self._m_max
85
86         # sign convention of search direction
87         self.p *= -1.
88         return self.p
89
90
91 class Secant:
92
93     def __init__(self, tol, margin):
94         self.tol = tol
95         self.margin = margin
96         self.bkt = [0., 1e15]
97
98     def update_bracket(self, a, proj_a):
99         if proj_a > 0.:
100             self.bkt[1] = a
101         else:
102             self.bkt[0] = a
103
104     def secant_step(self, a0, pa0, a1, pa1):
105         return (a0 * pa1 - a1 * pa0) / (pa1 - pa0)
106
107     def update(self, x, gx0, p, gradf):
108         a0 = 0.
109         proj_a0 = _ip(gx0, p)
110         self.bkt = [0., 0.]
111         self.update_bracket(a0, proj_a0)
112         a = 1.
113         i = 0
114         for i in range(0, 10):
115             x += (a - a0) * p
116             gx = gradf(x)
117             proj_a = _ip(gx, p)
118             self.update_bracket(a, proj_a)
119
120             if abs(proj_a) < self.tol:
121                 break
122
123         a2 = self.secant_step(a0, proj_a0, a, proj_a)

```

```
124         w = self.margin * (self.bkt[1] - self.bkt[0])
125         if a2 < self.bkt[0] + w \
126             or (self.bkt[1] != 0. \
127                 and a2 > self.bkt[1] - w):
128             a2 = 0.5 * (self.bkt[1] + self.bkt[0])
129
130         a0 = a
131         proj_a0 = proj_a
132         a = a2
133         gx0[:] = gx[:]
134         return a, i
135
136
137 def rosenbrock(x):
138     n = x.shape[0]
139     s = 0.
140
141     for i in range(n - 1):
142         s += 100. * (x[i + 1] - x[i] ** 2) ** 2 \
143             + (x[i] - 1.) ** 2
144
145     return s
146
147
148 def grad_rosenbrock(x):
149     n = x.shape[0]
150     s = zeros_like(x)
151
152     s[0] = 100. * 2. * (x[1] - x[0] ** 2) * (-2. * x[0]) + \
153         2. * (x[0] - 1.)
154     s[-1] = 100. * 2. * (x[-1] - x[-2] ** 2)
155
156     for i in range(1, n - 1):
157         s[i] = 100. * 2. * (x[i] - x[i - 1] ** 2)
158         s[i] += 100. * 2. * (x[i + 1] - x[i] ** 2) * \
159             (-2. * x[i]) + 2. * (x[i] - 1.)
160
161     return s
162
163
164 def main():
```

```
165 |     n = 5000
166 |     x = 0.5 * ones((n))
167 |     fx = rosenbrock(x)
168 |     gx = grad_rosenbrock(x)
169 |
170 |     m_max = 10
171 |     lbfgs = LBFGS(m_max)
172 |
173 |     max_iter = int(1e3)
174 |     tol = 1e-12
175 |     sec_tol = 1e-1
176 |
177 |     secant = Secant(sec_tol, 1e-1)
178 |
179 |     for i in range(0, max_iter):
180 |         p = lbfgs.update(x, gx)
181 |         a, li = secant.update(x[:,], gx[:,], p[:,], \
182 |                               grad_rosenbrock)
183 |         err = amax(abs(gx))
184 |         err_sol = sum(abs(x - 1.))
185 |         print("iter: ", i, "  err: ", err, \
186 |              "  abs err: ", err_sol)
187 |         if amax(abs(gx)) < tol:
188 |             break
189 |
190 |     print("Initial: ", fx, ", Final: ", rosenbrock(x))
191 |
192 |
193 | main()
```

APPENDIX C

Monte Carlo integration

One of the primary difficulties in calculating the strong-coupling diagrams in Chapter 8 is that they require, generally, summation over 3 Matsubara indices and integration over 5 angles. Calculating these sums by brute force numerical methods takes a huge amount of computational time to achieve any degree of precision. This is further exacerbated by the fact that evaluating the free-energy functional requires repeating this multidimensional problem multiple times to achieve self-consistency.

To improve the performance of these evaluation, it is useful to look at the problem as one of multidimensional integration. While the Matsubara frequencies are discrete, they can be considered as piecewise constant functions for the purposes of integration here. High dimensional integrals are a long-standing problem in numerical QFT, and one of the most successful methods for calculating them is Monte Carlo integration. Here we sketch out the basic motivations behind Monte Carlo integration schemes and our implementation for the strong-coupling free-energy functional.

We want to calculate the integral

$$(C.1) \quad I = \int_{\mathbf{v}} d\vec{x} f(\vec{x}),$$

where V is the volume of the domain \mathbf{V} being integrated over. Although our Matsubara frequencies do not have explicit bounds, the cutoff provided by the weak-coupling diagram at the spin-fluctuation scale guarantees convergence within a relatively small and predictable range of indices. In the simplest Monte Carlo we take N uniform samples $\{\vec{x}_i\}_1^N \in \mathbf{V}$ leading to the approximation for I ,

$$(C.2) \quad I_N \equiv \frac{V}{N} \sum_i \vec{x}_i = V \langle f \rangle .$$

The sample variance of f is

$$(C.3) \quad \text{Var}(f) = \frac{1}{N-1} \sum_i (f(\vec{x}_i)^2 - \langle f \rangle^2) ,$$

so that

$$(C.4) \quad \text{Var}(I_N) = \frac{V^2}{N} \text{Var}(f) .$$

This means that, so long as $\text{Var}(f)$ is well-behaved, the error in I_N decreases as $N^{1/2}$ independent of the dimension of the integration domain. This is qualitatively different than methods like Gaussian-quadrature, where the number of points required for a given precision will grow exponentially with dimension.

Clearly, there are better ways to sample a function than uniformly. The most straightforward would be to sample from a probability distribution proportional to $|f|$; however, sampling properly from arbitrary probability distributions is quite difficult. General purpose Monte Carlo algorithms attempt to approximate the probability distribution of $|f|$

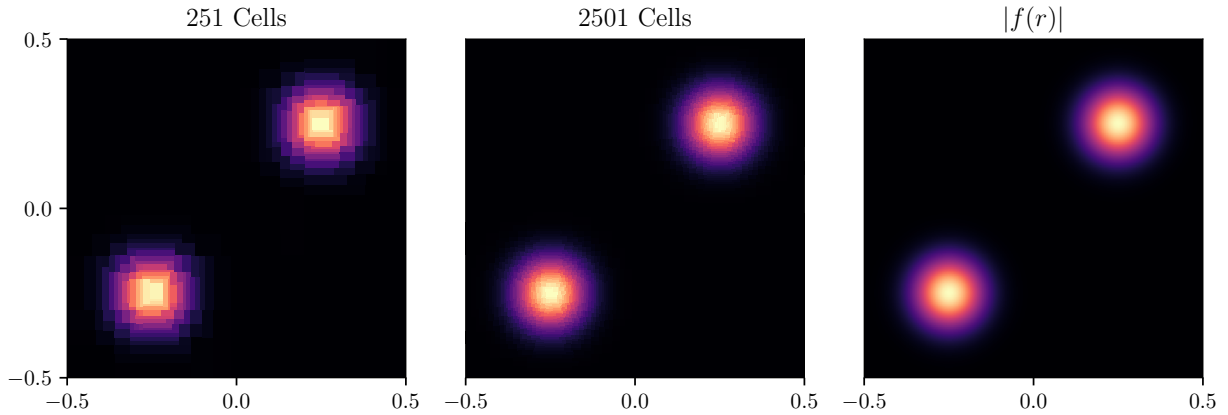


Figure C.1. Probability densities generated by Foam in comparison to the exact function, two gaussians on a diagonal. Brighter points are higher probability.

in a manner that requires minimal function evaluations and can itself be sampled efficiently. We implement the Foam Monte Carlo algorithm developed by Jadach[44], which iteratively creates a probability distribution through the cellular division of hypercubes.

Foam, as implemented here, works by starting from a single hypercube for the entire domain, taking a number of uniform samples, and then splitting the hypercube along a plane that maximally decreases the sum of the variance of the two new daughter cells. Then a new hypercube is chosen by whichever hypercube in the set has the largest variance. The algorithm finalizes the probability distribution after a set number of hypercubes have been generated. Each hypercube in the resulting probability distribution is weighted through its sample RMS value. Figures C.1 and C.2 show a comparison between foam distribution with different hypercube counts and probabilities derived from an exact $|f|$. The final Monte Carlo integration estimate is obtained by sampling this final probability distribution. We generally see estimated errors of less than 10^{-3} in the strong-coupling evaluations which are consistent across trials.

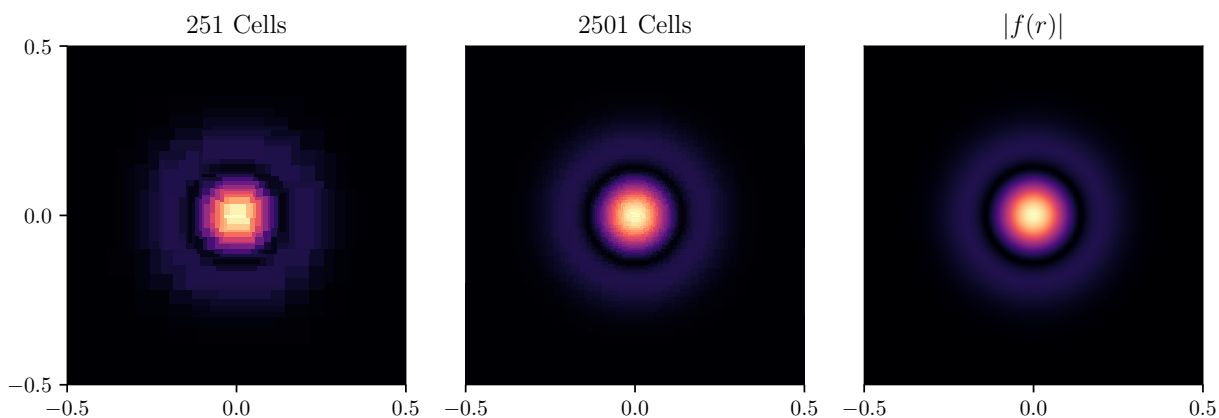


Figure C.2. Probability densities generated by Foam in comparison to the exact function, a Marr wavelet. Brighter points are higher probability.

For our application we regenerate the foam of hypercubes repeatedly with temperature and pressure. We also only care about the foam quality as far as it affects the numerical integration. From these considerations, our version of Foam differs slightly from the reference publications and code[44], in that it assumes the input function is not positive definite and adds multiprocessor support where possible to optimize the foam generation speed.